INFORMATION TO USERS

This manuscript has been reproduced from the microfilm master. UMI films the text directly from the original or copy submitted. Thus, some thesis and dissertation copies are in typewriter face, while others may be from any type of computer printer.

The quality of this reproduction is dependent upon the quality of the copy submitted. Broken or indistinct print, colored or poor quality illustrations and photographs, print bleedthrough, substandard margins, and improper alignment can adversely affect reproduction.

In the unlikely event that the author did not send UMI a complete manuscript and there are missing pages, these will be noted. Also, if unauthorized copyright material had to be removed, a note will indicate the deletion.

Oversize materials (e.g., maps, drawings, charts) are reproduced by sectioning the original, beginning at the upper left-hand corner and continuing from left to right in equal sections with small overlaps.

Photographs included in the original manuscript have been reproduced xerographically in this copy. Higher quality 6" x 9" black and white photographic prints are available for any photographs or illustrations appearing in this copy for an additional charge. Contact UMI directly to order.

Bell & Howell Information and Learning
300 North Zeeb Road, Ann Arbor, MI 48106-1346 USA
800-521-0600

UMI®

Numerical Investigations of Bose-Einstein Condensation in Trapped Dilute Gases and Other Topics

by

Meng Lu

A dissertation submitted to the Graduate Faculty in Physics
in partial fulfillment of the requirements for the degree of Doctor of Philosophy,
The City University of New York.

2000

Bell & Howell Information and Learning Company
300 North Zeeb Road
P.O. Box 1346
Ann Arbor, MI 48106-1346

This manuscript has been read and accepted for the Graduate Faculty in Physics in satisfaction of the dissertation requirement for the degree of Doctor of Philosophy.

14 Sept 2000 — Joseph L. Birman
Date — **Chair of Examining Committee**

Sept 18, 2000
Date — **Executive Officer**

Eugene Chudnovsky

Herman Cummins

Joel Gersten

Melvin Lax

Anatoly Kuklov

Supervisory Committee

THE CITY UNIVERSITY OF NEW YORK

Abstract

Numerical Investigations of Bose-Einstein Condensation in Trapped Dilute Gases and Other Topics

by

Meng Lu

Adviser: Joseph L. Birman, Distinguished Professor of Physics

In the first part of the thesis, the phenomenon of Bose-Einstein condensation of trapped dilute gases is investigated mainly using various numerical approaches. Mean field theory provides a framework to understand many features of the condensation. At zero temperature, the equation for the condensate ground state is derived and solved to obtain many properties of the system, such as density profile and various energies. The lowest excitation is obtained using Bogoliubov theory and shows excellent agreement with the experiments. At non-zero temperature, the ground state and the excited states have to be solved self-consistently by using the Popov approximation. The semi-classical approximation is used to simplify the calculation and the condensation fraction is obtained. We further extend the mean field theory to double condensates. The ground state is obtained and the separation of components is simulated based on the derived coupled equations. The research results presented in this part require a wide set of numerical techniques, such as solution of linear algebraic equations, integration of functions, muti-dimensional root finding, solutions to eigenvalue problems, and propagation of partial differential equation with initial values. Some comparisons are given with the experiments.

In the second part of the thesis, I present the research results for two subjects. (a) The scattering probabilities of hot excitons in narrow quantum wells (QWs)

are obtained. The exciton-phonon matrix element is considered by using an envelope function Hamiltonian approach in the strong quantization limit where the QW width is smaller than the exciton bulk Bohr radius. The Fröhlich-like interaction is taken into account and the contribution of the confined and interface modes to the scattering probability are calculated as a function of quantum well width, electron and hole effective masses, and in-plane center-of-mass kinetic energy. Inter- and intra-subband excitonic transitions are discussed in term of the phonon scalar potential selection rules. Comparison with the experiment is given. (b) The ground state of a few electron quantum dot is obtained using an exact numerical calculation based on the second quantized Hamiltonian.

Acknowledgements

I would like to express my gratitude to my thesis adviser, Professor Joseph L. Birman, who encourages me during all these years to overcome many difficulties and finally carry over this research work to its end. His vast knowledge and expertise are invaluable to my research. Professor Birman is more than just a mentor for my Ph.D. thesis. He treats students almost as family and is always there for me to offer any help he can to make sure that I complete this work.

I am very grateful to Professor Joel Gersten for giving me the opportunity to do theoretical research in physics and for his discussion during my early research work. I am particularly grateful to Professor Anatoly Kuklov, whose remarks and questions help me understand many aspects of my research. I am extremely thankful to Professor Carlos Trallero-Giner, without whom none of the research in Chapter 8 could happen.

I am also very thankful to Professors Herman Cummins and Melvin Lax for serving on my doctoral committee and for their very important education during my graduate study. I also would like to thank Professor Eugene Chudnovsky for being the member of my supervisory committee.

I want to thank Ms. Que Huong Nguyen, Mr. Ping Sun and Mr. Len Tevlin for their help and friendship.

Last but not least I would like to thank my parents and especially my wife for their endless patience and support.

Contents

List of Figures

List of Tables

Part I

Numerical Investigations of Bose-Einstein Condensation in Trapped Dilute Gases

Chapter 1

Introduction

An important consequence of quantum statistics for a system of ideal bosons is that, when the de Broglie wavelength of thermal motion, $\lambda_{dB} = (2\pi\hbar^2/m_0 k_B T)^{1/2}$, becomes comparable to the mean inter-particle separation, $r = \rho^{-1/3}$ as the temperature decreases, (Here, m_0 is the particle mass, k_B is the Boltzmann's constant, T is the absolute temperature, and ρ is the atom number density.) the system is predicted to develop suddenly a macroscopic population in the lowest energy state. This macroscopic quantum phenomenon is termed Bose-Einstein condensation (BEC), which was originally pointed out by Einstein in 1925. For many years, nobody took this BEC idea seriously, until London and Landau used it to explain the superfluidity of liquid helium in 1938. Superconductivity in metals also displays some properties of macroscopic quantum states. For an interdisciplinary review of BEC, see Ref. [1]. However, in these systems, the bosons are so closely packed that the pure quantum-statistical nature of the BEC transition is complicated by strong interactions. Hence there has been growing interest in finding BEC of a weakly interacting system, for which the comparison between experiment and theory would be possible.

In a landmark experiment [2], BEC in a dilute and weakly interacting atomic vapor in an anisotropic magnetic trap was first observed at JILA [1] in 1995. Almost at the same time, groups at MIT and Rice University observed evidence of BEC in dilute atomic ^{23}Na [3] and ^{7}Li [4] vapor produced by essentially the same technique. Three primary signatures of BEC were seen in these experiments: (a) On top of a thermal velocity distribution of the atoms, a narrow peak appeared that was centered at zero velocity. (b) The fraction of the atoms that were in this low-velocity peak increased abruptly as the sample temperature was lowered. (c) The peak exhibited a non-thermal, anisotropic velocity distribution expected of the minimum-energy quantum state of the magnetic trap in contrast to the isotropic, thermal velocity distribution observed in the broad uncondensed fraction.

In a typical BEC experiment at JILA, a gas of spin-polarized, ultracold ^{87}Rb atoms is optically precooled and trapped. The atoms are then loaded into a purely magnetic trap. The time-averaged orbiting potential (TOP) trap consisting of a static quadrupole field plus a small rotating transverse bias field is used to produce an effective harmonic trapping potential with cylindrical symmetry. The atoms are further cooled down by forced evaporation using a radio frequency (rf) magnetic field to selectively induce the Zeeman transition to untrapped spin states. The atom cloud can be observed by absorption imaging. The imaging procedure used by the JILA group in most of its BEC experiments is destructive, but by repeating the cycle of loading, cooling, and imaging, the time evolution of the system can be studied. Using the technique described above, many experiments have been done to probe the properties of the ground state and the excitated states of the BEC systems

[1] Joint Institute for Laboratory Astrophysics, University of Colorado at Boulder.

at both close to zero and finite temperature. For a review of BEC experiments, see Ref. [5].

Those experimental achievements of BEC in dilute alkali vapors have renewed great interest in the theoretical studies of the Bose gases. For comprehensive reviews, see Refs. [6, 7, 8]. One of the most important features of these trapped Bose gases is that they are inhomogeneous and finite sized systems, the number of atoms ranging typically from a few thousands to several millions. In most cases, the confining traps are well approximated by harmonic potentials. This makes the general approach to the problem somewhat different from those traditionally used to treat the homogeneous systems. Another important feature of the systems is that the vapor of the atoms used in these experiments are so dilute that the average distance between the atoms is much larger than the range of the interaction (typically the average distance between atoms is more than ten times the range of interatomic forces). So the interactions are primarily binary and can be treated theoretically within an s-wave scattering approximation, which is characterized by a single parameter a, the s-wave scattering length. Given the above features of the new BEC systems, the natural starting point is the generalized theory for an inhomogeneous weakly interacting Bose system [9]. This is a mean field approach, which provides closed and relatively simple equations for describing many phenomena associated with BEC. An extensive numerical investigation based on such a mean field theory is the main focus of this part of the thesis.

The plan for this part of the thesis is the following: In Chapter 2, we review the eigenvalue problem of the simple harmonic oscillators. We also present some analytical results for the thermodynamic properties of the ideal Bose gases trapped in

harmonic potentials. The derivation of those results is parallel to that of the uniform ideal Bose gases. In Chapter 3, we give the mean field theory for the ground state of the condensate. The ground state wave function is obtained using both approximation method, and numerical calculation. In Chapter 4, we give the Bogoliubov theory for the low excited states of the condensate at zero temperature. Numerical solutions are presented and compared with the recent experiment. In Chapter 5, we extend the Bogoliubov theory to non-zero temperature using the Popov approximation. The solutions are obtained using the semi-classical approximation method and self-consistent numerical calculation. In Chapter 6, we extend the mean field theory to the mixtures of condensates and obtain the coupled equations for double condensate wave functions. We also give a simple way to construct the Thomas-Fermi approximation solutions and present the numerical results corresponding the JILA experiment. We show that in the case considered, the Thomas-Fermi approximation is not in agreement with either experiment or the numerical calculation. In Chapter 7, we give the summary and discuss some open questions for this part of the thesis.

Chapter 2

Ideal Bose Gas in Harmonic Traps

2.1 Introduction

In this chapter, we will neglect the interaction between the atoms and consider the condensation of an ideal Bose gas in harmonic traps. The theory for such systems is not as trivial as it appears to be. The systems of interest are inhomogeneous and finite in size in contrast to the traditional BEC systems, which are homogeneous and infinite. A good description of those traditional BEC systems can be found in almost any good statistical mechanics book, for example, see [10]. We will present many properties for the trapped ideal BEC systems, such as the critical temperature, the fraction of particles in the condensate and the total energy.

2.2 Simple Harmonic Oscillators

As previously mentioned, the external trap used in the recent experiments on BEC can be modeled approximately as producing a harmonic potential

$$V_{ext}(x,y,z) = \frac{1}{2}m_0\left(\omega_x^2x^2 + \omega_y^2y^2 + \omega_z^2z^2\right), \tag{2.1}$$

where ω_x, ω_y and ω_z are the trap frequencies of three spatial directions. The eigenstates of the system are

$$\begin{aligned}\psi_{n_x,n_y,n_z}(x,y,z) &= N_x e^{-\frac{1}{2}\alpha_x^2 x^2} H_{n_x}(\alpha_x x) \\ &\times N_y e^{-\frac{1}{2}\alpha_y^2 y^2} H_{n_y}(\alpha_y y) \\ &\times N_z e^{-\frac{1}{2}\alpha_z^2 z^2} H_{n_z}(\alpha_z z)\,, \end{aligned} \tag{2.2}$$

where $H_n(x)$ is the Hermite polynomial and the eigenvalues are

$$\varepsilon_{n_x,n_y,n_z} = \left(n_x + \frac{1}{2}\right)\hbar\omega_x + \left(n_y + \frac{1}{2}\right)\hbar\omega_y + \left(n_z + \frac{1}{2}\right)\hbar\omega_z, \tag{2.3}$$

where $\alpha_x = (m_0\omega_x/\hbar)^{1/2}$, $\alpha_y = (m_0\omega_y/\hbar)^{1/2}$, $\alpha_z = (m_0\omega_z/\hbar)^{1/2}$ and $\{n_x, n_y, n_z\}$ are non-negative integers. The normalization constants are

$$N_x = \sqrt{\frac{\alpha_x}{\pi^{\frac{1}{2}} 2^{n_x} n_x!}}, \tag{2.4}$$

$$N_y = \sqrt{\frac{\alpha_y}{\pi^{\frac{1}{2}} 2^{n_y} n_y!}}, \tag{2.5}$$

$$N_z = \sqrt{\frac{\alpha_z}{\pi^{\frac{1}{2}} 2^{n_z} n_z!}}. \tag{2.6}$$

It is often useful to introduce the geometric average of the oscillator frequencies

$$\omega = (\omega_x\omega_y\omega_z)^{\frac{1}{3}}\,, \tag{2.7}$$

and harmonic oscillator length

$$d = \sqrt{\frac{\hbar}{m_0\omega}}. \tag{2.8}$$

For example, in term of ω and d, we may write the ground state wave function as

$$\psi_{0,0,0}(x,y,z) = \frac{1}{\pi^{\frac{3}{4}} d^{\frac{3}{2}}} \exp\left[-\frac{1}{2}\left(\frac{\omega_x}{\omega}\frac{x^2}{d^2} + \frac{\omega_y}{\omega}\frac{y^2}{d^2} + \frac{\omega_z}{\omega}\frac{z^2}{d^2}\right)\right]. \tag{2.9}$$

Many experiments use the harmonic traps with cylindrical symmetry. In these cases, we have the following external potential

$$V_{ext}(\rho, z) = \frac{1}{2} m_0 \left(\omega_\rho^2 \rho^2 + \omega_z^2 z^2\right), \tag{2.10}$$

where $\omega_\rho = \omega_x = \omega_y$ and $\rho = (x^2 + y^2)^{1/2}$. The ratio between the axial and radial frequencies, $\lambda = \omega_z/\omega_\rho$, fixes the asymmetry of the trap. For $\lambda < 1$ the trap is cigar shaped, while for $\lambda > 1$ the trap is disk shaped. For the external potential with cylindrical symmetry, the eigenstates of the system are

$$\begin{aligned}\psi_{n_\rho,m,n_z}(\rho, \phi, z) &= N_\rho e^{im\phi} (\alpha_\rho \rho)^{|m|} e^{-\frac{1}{2}\alpha_\rho^2 \rho^2} L_{n_\rho}^{|m|}\left(\alpha_\rho^2 \rho^2\right) \\ &\times N_z e^{-\frac{1}{2}\alpha_z^2 z^2} H_{n_z}(\alpha_z z),\end{aligned} \tag{2.11}$$

where $L_n^{|m|}(x)$ is the associated Laguerre polynomial and the eigenvalues are

$$\varepsilon_{n_\rho,m,n_z} = (2n_\rho + |m| + 1)\hbar\omega_\rho + \left(n_z + \frac{1}{2}\right)\hbar\omega_z, \tag{2.12}$$

where $\alpha_\rho = (m_0\omega_\rho/\hbar)^{1/2}$, $\alpha_z = (m_0\omega_z/\hbar)^{1/2}$ and $\{n_\rho, |m|, n_z\}$ are non-negative integers. The normalization constant N_z has the same expression as Eq. (2.6), while N_ρ is given by

$$N_\rho = \sqrt{\frac{\alpha_\rho^2 n_\rho!}{\pi(n_\rho + |m|)!}}. \tag{2.13}$$

For cylindrical traps, sometimes it is more convenient to use

$$d_\rho = \sqrt{\frac{\hbar}{m_0\omega_\rho}} \tag{2.14}$$

as the unit for length. For example, in terms of λ and d_ρ, the ground state wave function can be expressed as

$$\psi_{0,0,0}(\rho, z) = \frac{\lambda^{\frac{1}{4}}}{\pi^{\frac{3}{4}} d_\rho^{\frac{3}{2}}} \exp\left[-\frac{1}{2}\left(\frac{\rho^2}{d_\rho^2} + \lambda\frac{z^2}{d_\rho^2}\right)\right]. \tag{2.15}$$

2.3 Properties at Finite Temperature

At temperature T the total number of particles is given, in the grand-canonical ensemble, by the sum

$$N = \sum_{n_x,n_y,n_z} \frac{1}{e^{\beta(\varepsilon_{n_x,n_y,n_z}-\mu)}-1}, \tag{2.16}$$

while the total energy is given by

$$E = \sum_{n_x,n_y,n_z} \frac{\varepsilon_{n_x,n_y,n_z}}{e^{\beta(\varepsilon_{n_x,n_y,n_z}-\mu)}-1}. \tag{2.17}$$

where $\varepsilon_{n_x,n_y,n_z}$ is the eigenenergy of the ideal Bose gas in the harmonic trap given in Eq. (2.3), μ is the chemical potential and $\beta = 1/(k_B T)$. As in the case of uniform ideal Bose gas, it is convenient to separate out the lowest eigenvalue $\varepsilon_{0,0,0}$ from the sum (2.16) and call N_0 the number of particles in this state. When the chemical potential $\mu \to \mu_c = \hbar(\omega_x + \omega_x + \omega_x)/2$, N_0 can be macroscopic. The sum (2.16) becomes

$$N - N_0 = \sum_{n_x,n_y,n_z} \frac{1}{e^{\beta\hbar(n_x\omega_x+n_y\omega_y+n_z\omega_z)}-1}. \tag{2.18}$$

In order to evaluate this sum, one usually assumes that as $N \to \infty$, the relevant excitation energies, contributing to the sum (2.18), are much larger than the level spacing fixed by the trap frequencies. So the sum can be replaced by the following integral

$$N - N_0 = \int_0^\infty \frac{dn_x dn_y dn_z}{e^{\beta\hbar(n_x\omega_x+n_y\omega_y+n_z\omega_z)}-1}. \tag{2.19}$$

The accuracy of the approximation (2.19) is expected to be good if the number of trapped atoms is large and $k_B T \gg \hbar\omega$, where ω is the geometric average of trap frequencies defined in Eq. (2.7). The integral (2.19) can be calculated as

$$N - N_0 = \zeta(3)\left(\frac{k_B T}{\hbar\omega}\right)^3, \tag{2.20}$$

where $\zeta(n)$ is the Riemann ζ function. From this result one can obtain the transition temperature for the BEC by imposing that $N_0 \to 0$ at the transition temperature T_c^0, so one gets

$$k_B T_c^0 = \hbar\omega \left(\frac{N}{\zeta(3)}\right)^{\frac{1}{3}} = 0.94 N^{\frac{1}{3}} \hbar\omega. \tag{2.21}$$

The proper thermodynamic limit for these systems is obtained by letting $N \to \infty$ and $\omega \to 0$, while keeping the product $N\omega^3$ constant. With this definition, the transition temperature (2.21) is well defined in the thermodynamic limit. Inserting the above expression for T_c^0 into Eq. (2.20) one gets the temperature dependence of the condensate fraction for $T < T_c^0$:

$$\frac{N_0}{N} = 1 - \left(\frac{T}{T_c^0}\right)^3. \tag{2.22}$$

The same result can be also obtained by rewriting Eq. (2.19) as an integral over energy as follows

$$N - N_0 = \int_0^\infty d\varepsilon \rho(\varepsilon) \frac{1}{e^{\beta\varepsilon} - 1}, \tag{2.23}$$

where $\rho(\varepsilon)$ is the density of states given by

$$\rho(\varepsilon) = \frac{\varepsilon^2}{2(\hbar\omega)^3}. \tag{2.24}$$

The total energy can be found from the integral

$$E = \int_0^\infty d\varepsilon \rho(\varepsilon) \frac{\varepsilon}{e^{\beta\varepsilon} - 1}, \tag{2.25}$$

which gives the result

$$\frac{E}{N k_B T_c^0} = \frac{3\zeta(4)}{\zeta(3)} \left(\frac{T}{T_c^0}\right)^4. \tag{2.26}$$

These results can be compared with the well known results for the uniform Bose gases [10]. In the latter case, the eigenstates are plane waves with energy $\varepsilon = p^2/2m_0$

and the density of states is

$$\rho(\varepsilon) = \frac{V}{2\pi}\left(\frac{2m_0}{\hbar^2}\right)^{\frac{3}{2}}\sqrt{\varepsilon}, \tag{2.27}$$

where V is the volume. The condensate fraction is given by

$$\frac{N_0}{N} = 1 - \left(\frac{T}{T_c^0}\right)^{\frac{3}{2}}. \tag{2.28}$$

and the critical temperature is given by

$$k_B T_c^0 = \frac{2\pi\hbar^2}{m_0}\left(\frac{n}{\zeta(3/2)}\right)^{\frac{2}{3}}, \tag{2.29}$$

where $n = N/V$ is the density. The energy is given by

$$\frac{E}{N k_B T_c^0} = \frac{3\zeta(5/2)}{2\zeta(3/2)}\left(\frac{T}{T_c^0}\right)^{\frac{5}{2}}. \tag{2.30}$$

We can also calculate the density of particles outside the condensate $n_T(\vec{r})$ using the semiclassical approximation, which is valid for $k_B T \gg \hbar\omega$. At $T < T_c^0$ and in the thermodynamic limit, the thermal density is given by the integral over momentum space

$$n_T(\vec{r}) = \int \frac{d\vec{p}}{(2\pi\hbar)^3}\frac{1}{e^{\beta\varepsilon(\vec{p},\vec{r})}-1}, \tag{2.31}$$

where $\varepsilon(\vec{p},\vec{r})$ is the semiclassical energy in phase space given by

$$\varepsilon(\vec{p},\vec{r}) = \frac{p^2}{2m_0} + V_{ext}(\vec{r}). \tag{2.32}$$

The result is

$$n_T(\vec{r}) = \frac{1}{\lambda_{dB}^3} g_{\frac{3}{2}}\left(e^{-\beta V_{ext}(\vec{r})}\right), \tag{2.33}$$

where λ_{dB} is the de Broglie wavelength. The function $g_{3/2}(z)$ is defined as

$$g_\alpha(z) = \sum_{n=1}^{\infty} z^n/n^\alpha. \tag{2.34}$$

By integrating $n_T(\vec{r})$ over space one can get again the condensate fraction relation Eq. (2.22). It is now clear that there are two relevant energy scales for the ideal gas: the energy corresponding to the transition temperature $k_B T_c^0$ and the average level spacing $\hbar\omega$. From expression (2.21), we can see that for the current experiments on BEC with N ranging from a few thousands to several millions, $k_B T_c^0$ can be 10 to 100 larger than $\hbar\omega$. This implies that the semiclassical approximation can be used for a wide range of temperatures.

Chapter 3

Ground State at Zero Temperature

3.1 Introduction

In this chapter, we will use mean field theory to describe the ground state of the BEC at zero temperature. The equation for the condensate wave function is derived. When the number of the atoms is larger, the so called Thomas-Fermi approximation can be used to obtain the ground state. The focus of this chapter is to use two different numerical methods to obtain the ground state of BEC. The steepest descent method is fast and accurate, it provides us with the ground state wave function in the numerical form which is suitable for further studies of the dynamics of the condensate and non-zero temperature properties. The expansion method gives the solution in the form such that obtaining the low excited states is possible. We compare the results obtained from all the approximation and numerical methods.

3.2 Mean Field Theory for the Ground State

The starting point is the many-body Hamiltonian describing N interacting bosons with mass m_0 confined by an external potential $V_{ext}(\vec{r})$. In second quantization, it is given by

$$\hat{H} = \int d\vec{r}\hat{\Psi}^\dagger(\vec{r})\hat{H}_0\hat{\Psi}(\vec{r}) + \frac{1}{2}\int d\vec{r}d\vec{r}'\hat{\Psi}^\dagger(\vec{r})\hat{\Psi}^\dagger(\vec{r}')U(\vec{r}-\vec{r}')\hat{\Psi}(\vec{r}')\hat{\Psi}(\vec{r}), \tag{3.1}$$

where

$$\hat{H}_0 = -\frac{\hbar^2}{2m_0}\nabla^2 + V_{ext}(\vec{r}), \tag{3.2}$$

and $\hat{\Psi}(\vec{r})$ and $\hat{\Psi}^\dagger(\vec{r})$ are the boson field operators that annihilate and create a particle at position $\vec{r}$, respectively. $U(\vec{r}-\vec{r}')$ is the two-body interaction potential. In a dilute and cold gas, the de Broglie wavelengths of the atoms are very large compared to the range of the inter-atomic potential so that only binary collisions at low energy are relevant and three-body processes can be neglected. These collisions are characterized by a single parameter a, the s-wave scattering length. Thus the interaction potential can be approximated by

$$U(\vec{r}-\vec{r}') = U_0\delta(\vec{r}-\vec{r}'), \tag{3.3}$$

where $U_0 = 4\pi\hbar^2 a/m_0$. The Heisenberg equation of motion for $\hat{\Psi}(\vec{r},t)$ can be found as

$$i\hbar\frac{\partial\hat{\Psi}(\vec{r},t)}{\partial t} = \left[\hat{\Psi}(\vec{r},t),\hat{H}\right] = \hat{H}_0\hat{\Psi}(\vec{r},t) + U_0\hat{\Psi}^\dagger(\vec{r},t)\hat{\Psi}(\vec{r},t)\hat{\Psi}(\vec{r},t). \tag{3.4}$$

In the mean field approximation, the field operator is decomposed as

$$\hat{\Psi}(\vec{r},t) = \Psi(\vec{r},t) + \hat{\Phi}(\vec{r},t), \tag{3.5}$$

where $\Psi(\vec{r},t)$ is a complex function defined as the expectation of the field operator: $\Psi(\vec{r},t) = \langle\hat{\Psi}(\vec{r},t)\rangle$, while $\hat{\Phi}(\vec{r},t)$ is the residual operator describing the quantum and

thermal fluctuations around this mean value. The function $\Psi(\vec{r},t)$ is a classical field having the meaning of an order parameter and is often called the "wave function of the condensate". The normalization of this wave function fixes the number of atoms in the condensate at each time as follows

$$\int d\vec{r}|\Psi(\vec{r},t)|^2 = N_0. \tag{3.6}$$

Substituting Eq. (3.5) into Eq. (3.4), and making use of the property that the expectation value of $\hat{\Phi}(\vec{r},t)$ is zero, we obtain the following nonlinear Schrödinger equation, or "Gross-Pitaevskii" (GP) equation,

$$i\hbar\frac{\partial\Psi(\vec{r},t)}{\partial t} = \left(\hat{H}_0 + U_0|\Psi(\vec{r},t)|^2\right)\Psi(\vec{r},t), \tag{3.7}$$

The above equation can be used to study the dynamics of the condensate in various problems, such as, the expansion of cloud and the simulation of large amplitude oscillations. To get the stationary state $\Psi(\vec{r})$ of Eq. (3.7), we look for the solution of the following form

$$\Psi(\vec{r},t) = \Psi(\vec{r})e^{-i\mu t/\hbar}, \tag{3.8}$$

where μ is the chemical potential of the condensate. Substitute Eq. (3.8) into Eq. (3.7), and we now have the following time-independent GP equation

$$\left(\hat{H}_0 + U_0|\Psi(\vec{r})|^2\right)\Psi(\vec{r}) = \mu\Psi(\vec{r}). \tag{3.9}$$

It is worth noting that the above equation can also be obtained from the variational principle based on the following energy functional

$$E = \int d\vec{r}\left(\frac{\hbar^2}{2m}|\nabla\Psi(\vec{r})|^2 + V_{ext}(\vec{r})|\Psi(\vec{r})|^2 + \frac{U_0}{2}|\Psi(\vec{r})|^4\right), \tag{3.10}$$

with the normalization condition

$$\int d\vec{r}|\Psi(\vec{r})|^2 = N_0 \tag{3.11}$$

as a constraint. According to the method of Lagrangian multipliers, the problem is equivalent to an unconstrained variational problem with the following energy functional

$$\int d\vec{r}F = \int d\vec{r}\left(\frac{\hbar^2}{2m}|\nabla\Psi(\vec{r})|^2 + V_{ext}(\vec{r})|\Psi(\vec{r})|^2 + \frac{U_0}{2}|\Psi(\vec{r})|^4 - \mu|\Psi(\vec{r})|^2\right), \tag{3.12}$$

where μ is again the chemical potential. It is easy to show that the time-independent GP equation (3.9) can be obtained from the energy functional Eq. (3.12) using the following Euler equation:

$$\frac{\partial F}{\partial \Psi^*} - \frac{\partial}{\partial x}\left(\frac{\partial F}{\partial \Psi_x^*}\right) - \frac{\partial}{\partial y}\left(\frac{\partial F}{\partial \Psi_y^*}\right) - \frac{\partial}{\partial z}\left(\frac{\partial F}{\partial \Psi_z^*}\right) = 0, \tag{3.13}$$

where Ψ^* is the complex conjugate of the condensate wave function, and

$$\Psi_\alpha^* \equiv \frac{\partial \Psi^*}{\partial \alpha}, \qquad \alpha = x, y, z. \tag{3.14}$$

3.3 Thomas-Fermi Approximation

In the case of atoms with repulsive interaction ($a > 0$), one can obtain a very simple analytical form for the ground state wave function in the limit $Na/d \gg 1$, where the kinetic energy term in the time-independent GP equation becomes insignificant except near the condensate boundary [11]. Thus we may neglect the quantum pressure totally and obtain the the following algebraic equation for the wave function $\Psi(\vec{r})$

$$\left(V_{ext}(\vec{r}) + U_0|\Psi(\vec{r})|^2\right)\Psi(\vec{r}) = \mu\Psi(\vec{r}). \tag{3.15}$$

It has either the trivial solution $\Psi(\vec{r}) = 0$ or the following solution for the density profile

$$|\Psi(\vec{r})|^2 = \frac{1}{U_0}\left(\mu - V_{ext}(\vec{r})\right), \tag{3.16}$$

in the region where $\mu > V_{ext}(\vec{r})$, and $|\Psi(\vec{r})|^2 = 0$ outside the region. This is often referred to as Thomas-Fermi approximation. The chemical potential μ can be determined by the normalization condition Eq. (3.11), which now has the following form

$$\frac{1}{U_0}\int_{\mu > V_{ext}(\vec{r})} d\vec{r}\,(\mu - V_{ext}(\vec{r})) = N_0. \tag{3.17}$$

In the case of $V_{ext}(\vec{r})$ taking the general harmonic form as in Eq. (2.1), the chemical potential can be found as

$$\mu = \frac{\hbar\omega}{2}\left(15N_0\frac{a}{d}\right)^{\frac{2}{5}}. \tag{3.18}$$

For the external potential with cylindrical symmetry, we have the following expression

$$\mu = \frac{\hbar\omega_\rho}{2}\left(15N_0\lambda\frac{a}{d_\rho}\right)^{\frac{2}{5}}. \tag{3.19}$$

3.4 Steepest Descent Method

One way of obtaining the ground state of the BEC systems numerically is through the steepest descent approach, which is a method of direct minimization of the energy functional (3.12). In general, a time-dependent wave function $\Psi(\vec{r}, t)$, where t is a fictitious time variable, is evaluated at different time steps, starting from an arbitrary trial wave function and converging to the exact solution $\Psi(\vec{r}, \infty) \equiv \Psi(\vec{r})$. The time evolution can be formulated in terms of the equation

$$\frac{\partial\Psi(\vec{r}, t)}{\partial t} = -\frac{\delta E}{\delta\Psi(\vec{r}, t)}, \tag{3.20}$$

where E is the functional defined in Eq. (3.10) and δ denotes the constrained functional derivative which preserves the normalization Eq. (3.11). In our case, Eq. (3.20) becomes the following equation

$$-\hbar\frac{\partial\Psi(\vec{r},t)}{\partial t} = \left(-\frac{\hbar^2}{2m}\nabla^2 + V_{ext}(\vec{r}) + U_0|\Psi(\vec{r},t)|^2\right)\Psi(\vec{r},t), \tag{3.21}$$

where $\Psi(\vec{r},t)$ can be chosen to be real to simplify the calculation. Usually, we use the corresponding Thomas-Fermi approximation solution as the initial condition for systems with large number of particles and the ground state of the simple harmonic oscillator as the initial condition for systems with small number of particles. The normalization of $\Psi(\vec{r},t)$ is kept constant at all time. We have to point out that if the numerical implementation of the method is correct, the choice of the initial trial state should not really matter, i.e., different initial conditions should all give the same result, which minimizes the energy functional (3.10). The only difference is the speed of convergence. This can be used as a test of the computer codes. We will only consider the traps with cylindrical symmetry having the form of Eq. (2.10). It can be shown that the ground state of the system also has the cylindrical symmetry, which means that the ground state wave function only depends on ρ and z. To get a convenient dimensionless form of Eq. (3.21) suitable for numerical study, we scale the variables and wave function as follows

$$\omega_\rho t \to t; \quad \rho/d_\rho \to \rho; \quad z/d_\rho \to z; \quad a/d_\rho \to a; \quad d_\rho^{\frac{3}{2}}\Psi(\rho,z,t) \to \Psi(\rho,z,t), \tag{3.22}$$

where d_ρ is the harmonic oscillator length defined in Eq. (2.14). With the understanding that all physical quantities will take suitable dimensionless forms from now

on until the end of this section, we transfer Eq. (3.21) into the following form

$$-\frac{\partial\Psi(\rho,z,t)}{\partial t} = -\frac{1}{2}\left(\frac{\partial^2}{\partial\rho^2}+\frac{1}{\rho}\frac{\partial}{\partial\rho}+\frac{\partial^2}{\partial z^2}\right)\Psi(\rho,z,t) + \left(V_{ext}(\rho,z)+U_0|\Psi(\rho,z,t)|^2\right)\Psi(\rho,z,t), \tag{3.23}$$

where $V_{ext}(\rho,z)$ and U_0 take the following dimensionless form

$$V_{ext}(\rho,z) = \frac{1}{2}\left(\rho^2+\lambda^2 z^2\right), \tag{3.24}$$

$$U_0 = 4\pi a. \tag{3.25}$$

It is useful to note that the chemical potential now takes the following dimensionless form

$$\mu = \frac{1}{2}(15N_0\lambda a)^{\frac{2}{5}}. \tag{3.26}$$

It is usually convenient to introduce a new wave-function

$$u(\rho,z,t) = \rho\Psi(\rho,z,t), \tag{3.27}$$

which is zero at $\rho = 0$. The equation for $u(\rho,z,t)$ is as follows

$$-\frac{\partial u(\rho,z,t)}{\partial t} = \left(\hat{T}_\rho+\hat{T}_z+\bar{V}\right)u(\rho,z,t), \tag{3.28}$$

where

$$\hat{T}_\rho = -\frac{1}{2}\left(\frac{\partial^2}{\partial\rho^2}-\frac{1}{\rho}\frac{\partial}{\partial\rho}\right), \tag{3.29}$$

$$\hat{T}_z = -\frac{1}{2}\frac{\partial^2}{\partial z^2}, \tag{3.30}$$

$$\bar{V} = V_{ext}(\rho,z)-\frac{1}{2\rho^2}+U_0\frac{|u(\rho,z,t)|^2}{\rho^2}. \tag{3.31}$$

Meanwhile the normalization condition Eq. (3.11) becomes

$$2\pi\int_0^\infty\int_{-\infty}^\infty \rho d\rho dz\frac{|u(\rho,z,t)|^2}{\rho^2} = N_0. \tag{3.32}$$

We solve such an initial value problem using the alternating-direction implicit (ADI) scheme on a square grid and equally spaced points along the t-axis [12]. We thus denote

$$\begin{aligned} \rho_j &= j\Delta r, \\ z_k &= k\Delta r, \\ t_n &= n\Delta t, \end{aligned} \tag{3.33}$$

where $j = 1, \ldots, N_r$, $k = -(N_r - 1)/2, \ldots, (N_r - 1)/2$ and $n = 1, \ldots, N_t$. Here we have chosen N_r to be an odd number for a symmetric sampling along z-axis. We define

$$u_{j,k}^n = u(\rho_j, z_k, t_n). \tag{3.34}$$

A formal integration from t_n to $t_n + \Delta t$ gives

$$u_{j,k}^{n+1} = e^{-(\hat{T}_\rho + \hat{T}_z + \bar{V})\Delta t} u_{j,k}^n. \tag{3.35}$$

The idea of ADI is to divide each time step into two steps of size $\Delta t/2$. In each substep, a different geometrical dimension is treated implicitly. Therefore, we operate on both sides of Eq. (3.35) with $\exp\left[(\hat{T}_\rho + \hat{T}_z + \bar{V})\Delta t/2\right]$, and after neglecting terms $\sim O(\Delta t^2)$, we get

$$\begin{aligned} &\left(1 + \hat{T}_\rho \frac{\Delta t}{2}\right)\left(1 + \hat{T}_z \frac{\Delta t}{2}\right) e^{\bar{V}\Delta t/2} u_{j,k}^{n+1} \\ &= \left(1 - \hat{T}_\rho \frac{\Delta t}{2}\right)\left(1 - \hat{T}_z \frac{\Delta t}{2}\right) e^{-\bar{V}\Delta t/2} u_{j,k}^n. \end{aligned} \tag{3.36}$$

We then introduce an intermediate function $v_{j,k}^n$ and obtain the following equations

$$\left(1 + \hat{T}_\rho \frac{\Delta t}{2}\right) v_{j,k}^n = \left(1 - \hat{T}_z \frac{\Delta t}{2}\right) u_{j,k}^n, \tag{3.37}$$

$$\left(1 + \hat{T}_z \frac{\Delta t}{2}\right) e^{\bar{V}\Delta t/2} u_{j,k}^{n+1} = \left(1 - \frac{\Delta t}{2}\hat{T}_\rho\right) e^{-\bar{V}\Delta t/2} v_{j,k}^n. \tag{3.38}$$

Using the fully implicit scheme, we obtain the following equation from Eq. (3.37) for the ρ direction

$$\begin{aligned}&\left[1 - e(v^n_{j+1,k} - 2v^n_{j,k} + v^n_{j-1,k}) + e(v^n_{j+1,k} - v^n_{j-1,k})/(2j)\right]\\ &= \left[1 + e(u^n_{j,k+1} - 2u^n_{j,k} + u^n_{j,k-1})\right],\end{aligned} \tag{3.39}$$

where

$$e = \frac{\Delta t}{4\Delta r^2}. \tag{3.40}$$

This tri-diagonal system can be easily solved by the LU decomposition method [12]. We now introduce

$$\tilde{v}^n_{j,k} = e^{-\bar{V}(v^n_{j,k})\Delta t/2} v^n_{j,k}, \tag{3.41}$$

Hence, we have a similar tri-diagonal system for the z direction

$$\begin{aligned}&\left[1 - e(\tilde{u}^{n+1}_{j,k+1} - 2\tilde{u}^{n+1}_{j,k} + \tilde{u}^{n+1}_{j,k-1})\right]\\ &= \left[1 + e(\tilde{v}^n_{j+1,k} - 2\tilde{v}^n_{j,k} + \tilde{v}^n_{j-1,k}) - e(\tilde{v}^n_{j+1,k} - \tilde{v}^n_{j-1,k})/(2j)\right],\end{aligned} \tag{3.42}$$

where

$$\tilde{u}^{n+1}_{j,k} = e^{\bar{V}(\tilde{u}^{n+1}_{j,k})\Delta t/2} u^{n+1}_{j,k}. \tag{3.43}$$

At each time step we need to calculate the kinetic energy E_{kin}, the potential energy E_{pot}, the interaction energy E_{int} and the total energy E_{tot} to make sure of the convergence of the solution. The search for the ground state is completed only when all these energies converge within a predefined numerical error. In dimensionless forms

$$\begin{aligned}E_{kin} &= -\pi \int_0^\infty \int_{-\infty}^\infty \rho d\rho dz \frac{u^*}{\rho^2}\left(\frac{\partial^2 u}{\partial \rho^2} - \frac{1}{\rho}\frac{\partial u}{\partial \rho} + \frac{u}{\rho^2} + \frac{\partial^2 u}{\partial z^2}\right),\\ E_{pot} &= \pi \int_0^\infty \int_{-\infty}^\infty \rho d\rho dz \left(\rho^2 + \lambda^2 z^2\right)\frac{|u|^2}{\rho^2},\\ E_{int} &= 4\pi^2 a \int_0^\infty \int_{-\infty}^\infty \rho d\rho dz \frac{|u|^4}{\rho^4},\end{aligned} \tag{3.44}$$

and

$$E_{tot} = E_{kin} + E_{pot} + E_{int}. \tag{3.45}$$

Using the numerical method presented above, we calculated the ground state of the ^{87}Rb condensate typically used by the JILA group. The s-wave scattering length of ^{87}Rb atoms is about $110a_0$, where a_0 is the Bohr radius. The experimental trap has cylindrical symmetry, with $\omega_\rho = 2\pi \times 132$Hz and the asymmetry parameter of the trap $\lambda = \omega_z/\omega_\rho = \sqrt{8}$. The results are listed in Table 3.1. We also plot the wave

N_0	E_{kin}/N_0	E_{pot}/N_0	E_{int}/N_0	E_{tot}/N_0	μ
100	1.016634	1.439999	0.285072	2.741705	3.026777
200	0.930804	1.609129	0.455948	2.995881	3.451829
500	0.803405	1.967900	0.781570	3.552875	4.334445
1000	0.705009	2.378480	1.122441	4.205929	5.328370
2000	0.609817	2.950160	1.569422	5.129399	6.698821
5000	0.493853	4.038428	2.378091	6.910373	9.288464
10000	0.415938	5.199341	3.212228	8.827507	12.039735
20000	0.347335	6.750410	4.306383	11.404127	15.710510
50000	0.270778	9.608669	6.299399	16.178846	22.478245
100000	0.222806	12.594159	8.373950	21.190916	29.564866
200000	0.182465	16.532921	11.117594	27.832979	38.950573
500000	0.139279	23.711472	16.163639	40.014389	56.178028
1000000	0.113112	31.143393	21.466280	52.722786	74.189066
2000000	0.091622	40.875393	28.545198	69.512215	98.057413
5000000	0.069127	58.439503	41.736393	100.245026	141.981419

Table 3.1: Results for the ground state of ^{87}Rb atoms in a trap with $\omega_\rho = 2\pi \times 132$Hz and $\lambda = \sqrt{8}$. The energies and chemical potential are given in the unit of $\hbar\omega_\rho$ and the lengths are given in the unit of d_ρ.

functions for different N_0 in Fig. 3.1. When N_0 increases, the repulsive force among atoms tends to lower the central density and expand the cloud of atoms towards regions where the trapping potential is higher. This produces an increase of both

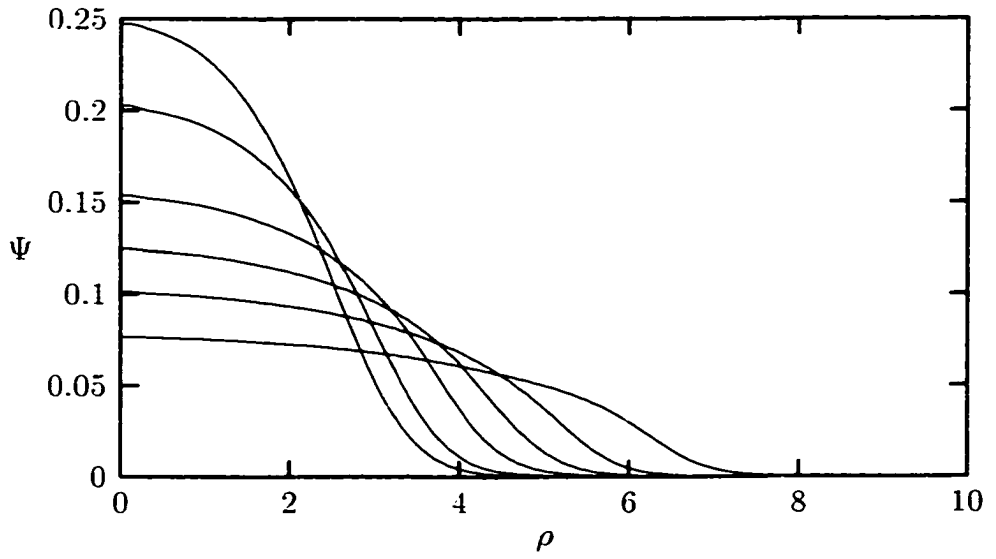

Figure 3.1: Ground state wave function for ^{87}Rb along ρ axis. The wave functions are normalized to 1. Lengths are given in the unit of d_ρ. The lines corresponds to $N_0 = 1000$, 2000, 5000, 10000, 20000, and 50000, in descending order of central density.

the internal and the harmonic oscillator potential energy per particle. However, the kinetic energy per particle decreases because the density distribution is flattened. This also shows that the Thomas-Fermi approximation should be more accurate for larger number of atoms. In Fig. 3.2, we compare the ground state wave function obtained from the steepest descent calculation and Thomas-Fermi approximation for 5000 ^{87}Rb atoms. The agreement is quite good except at the boundary of

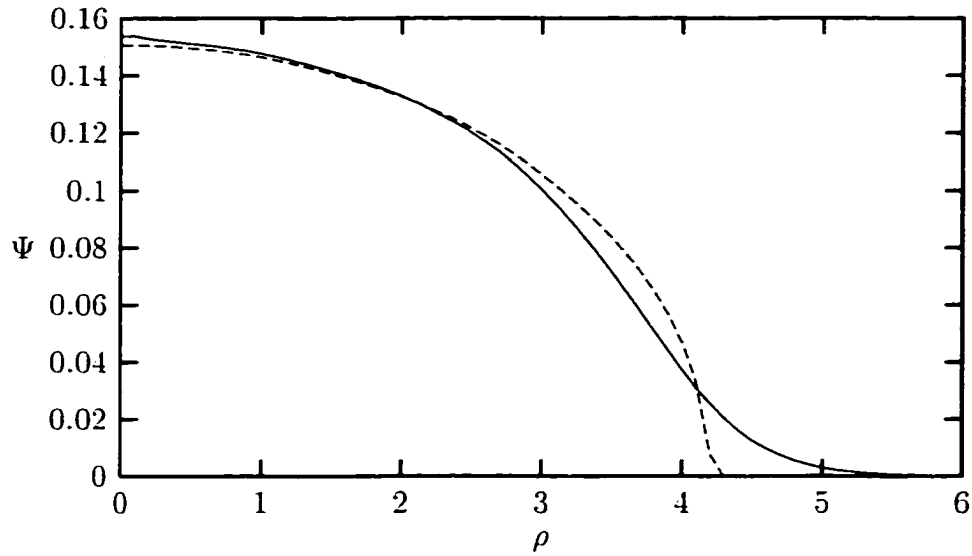

Figure 3.2: Ground state wave function for 5000 ^{87}Rb atoms. Solid line corresponds to the the numerical result, while the dashed line corresponds to the Thomas-Fermi approximation. The length is given in the unit of d_ρ.

the condensate. Simple relationship among the different contributions to the total energy can be obtained using the virial theorem [13] as

$$2E_{kin} - 2E_{pot} + 3E_{int} = 0 \tag{3.46}$$

One can easily see that the numerical results in Table 3.1 satisfy this relation very well.

3.5 Expansion Method

In this section, we will describe how to obtain the ground state of a condensate from solving the time-independent GP equation (3.9) by using the method of expanding the solution in a fixed basis. In order to simplify the calculation and to compare with the experiments, we will once again focus on the cylindrical harmonic trap. We expand the normalized condensate wave function $\psi_g(\vec{r}) \equiv \Psi(\vec{r})/\sqrt{N_0}$ in the basis of trap-potential eigenstates, i.e.,

$$\psi_g(\vec{r}) = \sum_{\nu} a_\nu \varphi_\nu(\vec{r}), \tag{3.47}$$

where ν represents a set of quantum numbers (n_ρ, m, n_z) and the sum expands over the N_{basis} basis-set functions. Inserting Eq. (3.47) into Eq. (3.9) and taking the scalar product with each basis-set function converts the problem to one of finding the simultaneous root of N_{basis} nonlinear algebraic functions having the following form

$$f_\nu(\{a\}) \equiv (\epsilon_\nu - \mu)a_\nu + N_0 U_0 \sum_{\nu_1,\nu_2,\nu_3} C(\nu, \nu_1, \nu_2, \nu_3) a^*_{\nu_1} a_{\nu_2} a_{\nu_3} = 0. \tag{3.48}$$

The coefficients $C(\nu_1, \nu_2, \nu_3, \nu_4)$ are the integrals of the product of four trap wave functions. Method for evaluating these integrals are described later in this section. These nonlinear equations can be solved by a standard Newton-Raphson technique provided a good guess of the solution is known [12]. Equations (3.48) are not sufficient to determine the set $\{a\}$ since μ is also unknown. If we choose a value of μ, and a corresponding value of N_0, a solution may be found that will, in general, not be normalized. This solution may be normalized by the simultaneous rescaling of the basis-set coefficient $\{a\}$, and the number of condensate atoms, N_0. For example,

we can find an arbitrary solution $\psi_{N_A}(\vec{r})$ of the time-independent GP equation

$$\left(\hat{H}_0 + N_A U_0 |\psi_{N_A}|^2\right) \psi_{N_A}(\vec{r}) = \mu \psi_{N_A}(\vec{r}), \tag{3.49}$$

then find the norm of the solution

$$A^2 = \int d\vec{r} |\psi_{N_A}(\vec{r})|^2, \tag{3.50}$$

where A is some constant. The set $\{a_A\}$, the basis-set coefficients for the solution $\psi_{N_A}(\vec{r})$, and the condensate population N_A may be rescaled as follows

$$\{a_B\} = \left\{\frac{a_A}{A}\right\}, \qquad N_B = A^2 N_A, \tag{3.51}$$

to give a normalized solution $\psi_{N_B}(\vec{r})$ for the new GP equation

$$\left(\hat{H}_0 + N_B U_0 |\psi_{N_B}(\vec{r})|^2\right) \psi_{N_B}(\vec{r}) = \mu \psi_{N_B}(\vec{r}). \tag{3.52}$$

So we (a) find an arbitrary solution $\psi_{N_A}(\vec{r})$, then (b) find a normalized solution $\psi_{N_B}(\vec{r})$ from $\psi_{N_A}(\vec{r})$ by rescaling both the wave function and the number of atoms in the condensate. To ensure that the final normalized solution is actually the lowest energy state of the condensate, we simulate the adiabatic growth of the nonlinear term in Eqs. (3.48) by first finding a solution for a value of μ close to the non-interacting ground state energy, which corresponds to a very small number of particles in the condensate, and so the condensate wave function is very close to that of the trap ground state. The initial values of the basis-set coefficients are those of the trap ground state, i.e., $\{a\} = \{1, 0, 0, ...\}$. The Newton-Raphson algorithm is then used to solve Eqs. (3.48). The chemical potential μ is then incremented, corresponding to an increase in condensate size, and the basis-set coefficients found previously, for smaller condensate, are used as the initial values for this new solution.

Now we describe the method used for evaluating the coefficients $C(\nu_1,\nu_2,\nu_3,\nu_4)$, which are given by the following integral

$$C(\nu_1,\nu_2,\nu_3,\nu_4)=\int_0^{2\pi}d\phi\int_0^{\infty}d\rho\rho\int_{-\infty}^{\infty}dz\psi^*_{\nu_1}(\vec{r})\psi^*_{\nu_2}(\vec{r})\psi_{\nu_3}(\vec{r})\psi_{\nu_4}(\vec{r}). \tag{3.53}$$

Using the dimensionless variables $\zeta=(\alpha_\rho\rho)^2$ and $\xi=\alpha_z z$, we change the integral (3.53) into the following form

$$C(\nu_1,\nu_2,\nu_3,\nu_4)=\frac{N}{2\alpha_\rho^2\alpha_z}\Phi(\nu_1,\nu_2,\nu_3,\nu_4)U(\nu_1,\nu_2,\nu_3,\nu_4)\Xi(\nu_1,\nu_2,\nu_3,\nu_4), \tag{3.54}$$

where N is the total normalization constant and

$$\Phi(\nu_1,\nu_2,\nu_3,\nu_4)=\int_0^{2\pi}d\phi e^{i\phi(m_3+m_4-m_1-m_2)}, \tag{3.55}$$

$$\begin{aligned}U(\nu_1,\nu_2,\nu_3,\nu_4)&=\int_0^{\infty}d\zeta e^{-2\zeta}\zeta^{(m_3+m_4-m_1-m_2)/2}\\&\quad\times L^{|m_1|}_{n_{\rho_1}}(\zeta)L^{|m_2|}_{n_{\rho_2}}(\zeta)L^{|m_3|}_{n_{\rho_3}}(\zeta)L^{|m_4|}_{n_{\rho_4}}(\zeta),\end{aligned} \tag{3.56}$$

$$\Xi(\nu_1,\nu_2,\nu_3,\nu_4)=\int_{-\infty}^{\infty}d\xi e^{-2\xi^2}H_{n_{z_1}}(\xi)H_{n_{z_2}}(\xi)H_{n_{z_3}}(\xi)H_{n_{z_4}}(\xi). \tag{3.57}$$

Eq. (3.55) may be evaluated easily to give

$$\Phi(\nu_1,\nu_2,\nu_3,\nu_4)=2\pi\delta_{m_1+m_2,m_3+m_4}. \tag{3.58}$$

$U(\nu_1,\nu_2,\nu_3,\nu_4)$ and $\Xi(\nu_1,\nu_2,\nu_3,\nu_4)$ may be evaluated using the Gaussian quadrature methods [12]. With transformation $u=2\zeta$, $U(\nu_1,\nu_2,\nu_3,\nu_4)$ becomes

$$\begin{aligned}U(\nu_1,\nu_2,\nu_3,\nu_4)&=\frac{1}{2^{(m_1+m_2+m_3+m_4+2)/2}}\sum_{i=0}^{N^{\zeta}_{Quad}}w_i^L\left(g_i^L\right)^{(m_1+m_2+m_3+m_4)/2}\\&\quad\times L_{n_1}^{(|m_1|)}\left(\frac{g_i^L}{2}\right)L_{n_2}^{(|m_2|)}\left(\frac{g_i^L}{2}\right)L_{n_3}^{(|m_3|)}\left(\frac{g_i^L}{2}\right)L_{n_4}^{(|m_4|)}\left(\frac{g_i^L}{2}\right),\end{aligned} \tag{3.59}$$

where g_i^L is the ith Gauss-Laguerre quadrature point and w_i^L is the corresponding weight. This sum is exact provided $N^{\zeta}_{Quaad}>2max(n_\rho)+max(m)$. Applying the

same technique to $\Xi(\nu_1, \nu_2, \nu_3, \nu_4)$ with the transformation $v = \sqrt{2}\xi$, we have

$$\Xi(\nu_1, \nu_2, \nu_3, \nu_4) = \frac{1}{\sqrt{2}} \sum_{i=0} N^{\xi}_{Quad} w_i^H \times H_{n_1}\left(\frac{g_i^H}{\sqrt{2}}\right) H_{n_2}\left(\frac{g_i^H}{\sqrt{2}}\right) H_{n_3}\left(\frac{g_i^H}{\sqrt{2}}\right) H_{n_4}\left(\frac{g_i^H}{\sqrt{2}}\right), \quad (3.60)$$

where g_i^H is the ith Gauss-Hermite quadrature point and w_i^H is the corresponding weight. This sum is exact provided $N^{\xi}_{Quad} > 2max(n_z)$. This means that the choice of basis-set functions fixes the number of quadrature points needed, e.g., for the calculation of the cylindrically symmetric ground state, we may use $n_\rho = \{0, \ldots, 6\}$, $m = 0$, and $n_z = \{0, \ldots, 6\}$, fixing $N^{\zeta}_{Quad} = 13$ and $N^{\xi}_{Quad} = 13$.

Using the expansion and integration method described above, we solved the time-independent GP equation (3.9) for the BEC systems consisting of ^{87}Rb atoms in the same harmonic trap considered in the previous section. The radial trapping frequency $\omega_\rho = 2\pi \times 132$Hz, and the asymmetry parameter $\lambda = \sqrt{8}$. Since we are interested in the ground state at this time, we only need to expand the ground state wave function in those eigenstates of a harmonic oscillator with $m = 0$ and n_z being an even number. In Fig. 3.3, we plot the energy levels of those relevant states. This diagram can tell us how many eigenstates should be included in the expansion given the energy cut-off E_{max}. For example, for $E_{max} = 15\hbar\omega_\rho$, the number of basis is $N_{basis} = 12$. We have done the calculation for $E_{max} = 15\hbar\omega_\rho$, $20\hbar\omega_\rho$ and $25\hbar\omega_\rho$, the results are plotted in Fig. 3.4. The figure shows that for $N < 10000$, it is already very accurate to take $E_{max} = 25\hbar\omega_\rho$. This is also clear from Table 3.1, which shows that for $N = 10000$, the total energy $E_{tot} = 8.83\hbar\omega_\rho$. Thus we basically use the basis up to three times the total energy of the ground state wave function. In Table 3.2, we list the chemical potential obtained from the Thomas-Fermi approximation,

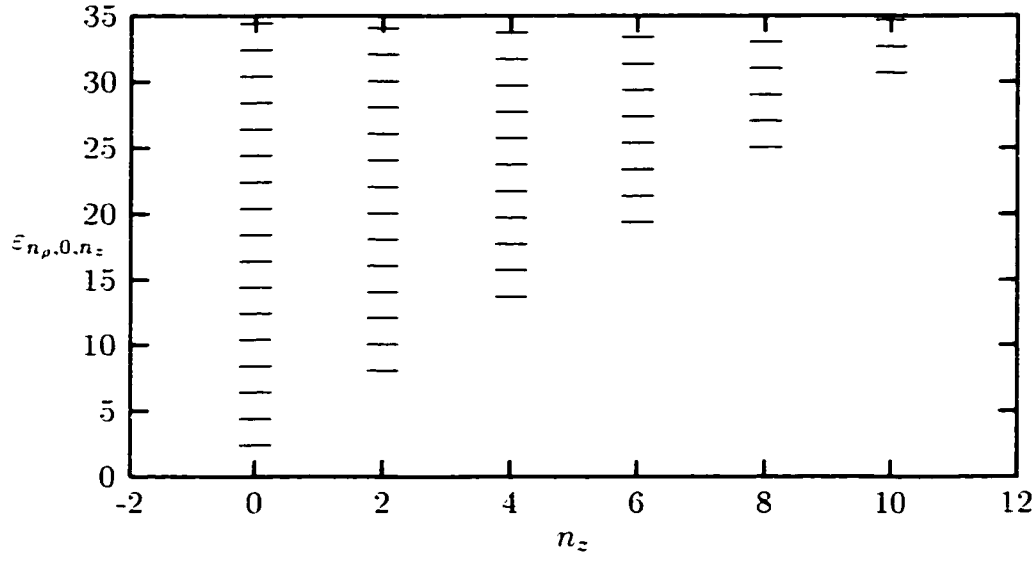

Figure 3.3: Energy levels of harmonic trap with $\omega_\rho = 2\pi \times 132$Hz and $\lambda = \sqrt{8}$. The energy is given in the unit of $\hbar\omega_\rho$.

the steepest descent method and the basis expansion method. It is clear from the table that the Thomas-Fermi approximation gives more accurate results for larger number of atoms. The results obtained from the steepest descent and expansion methods agree with each other very well for all cases considered here.

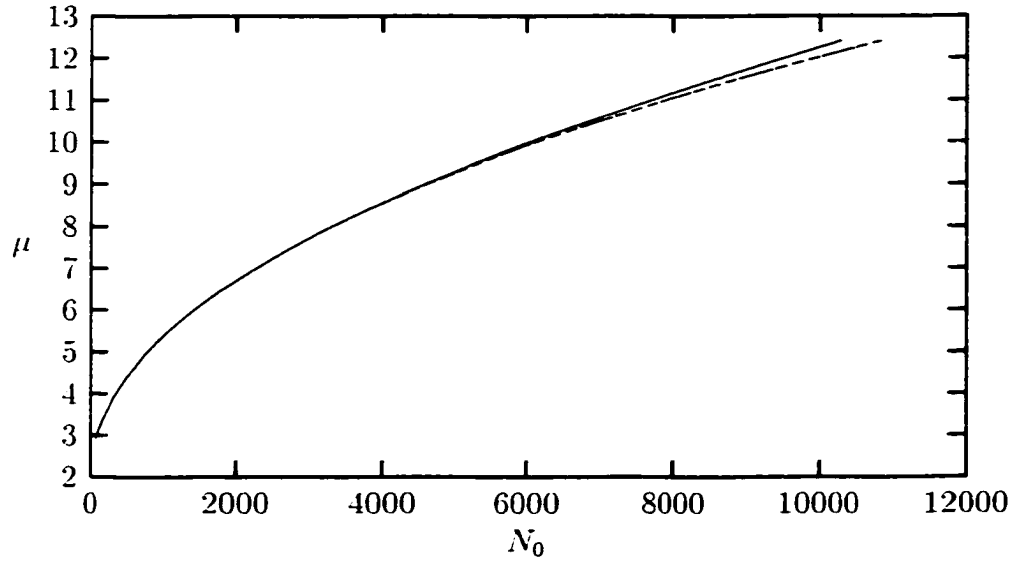

Figure 3.4: Chemical potential of condensates with different sizes. The energy is given in the unit of $\hbar\omega_\rho$. The upper line is the result for $E_{max} = 15\hbar\omega_\rho$ and the lower lines are the results for $E_{max} = 20\hbar\omega_\rho$ and $25\hbar\omega_\rho$, which are practically indistinguishable.

N	μ_{TF}	μ_{SD}	μ_{BE}
1000	4.645335	5.328370	5.326346
2000	6.129557	6.698821	6.694606
3000	7.208843	7.719611	7.713895
4000	8.087999	8.560796	8.553922
5000	8.843111	9.288464	9.280624
6000	9.512126	9.936340	9.927610
7000	10.117106	10.524371	10.514711
8000	10.672178	11.065387	11.054826
9000	11.187011	11.568431	11.556835
10000	11.668555	12.039735	12.027165

Table 3.2: Results for the ground state of ^{87}Rb atoms in the trap with $\omega_\rho = 2\pi \times$ 132Hz and $\lambda = \sqrt{8}$. The chemical potentials are given in the unit of $\hbar\omega_\rho$. Here, the subscripts TF, SD and BE denote Thomas-Fermi, steepest descent and basis expansion method, respectively.

Chapter 4

Elementary Excitations at Zero Temperature

4.1 Introduction

In this chapter, we will present the Bogoliubov theory for the collective excitations of the condensate. The Bogoliubov equations for determining the excitation frequencies are derived using both the Bogoliubov transformation and linear-response analysis. Using the expansion method of the previous chapter, we are able to obtain the lowest excitation frequencies of condensates with different total number of atoms N_0. The agreement with the JILA experiment is excellent. We also present a general approach to the numerical study of the dynamics of BEC. We describe and compare different numerical propagation schemes. The large amplitude oscillation of the excitation is simulated using a very stable and accurate numerical scheme.

4.2 Bogoliubov Theory

The derivation of the elementary excitation spectrum of a weakly interacting, homogeneous Bose gas was done by Bogoliubov (1947). In order to correspond more

directly to the recent BEC experiments in trapping potentials, we present here a revised theory. We start with the following grand canonical Hamiltonian

$$\begin{aligned}\hat{K} &\equiv \hat{H} - \mu\hat{N} \\ &= \int d\vec{r}\hat{\Psi}^\dagger(\vec{r})\hat{H}_0\hat{\Psi}(\vec{r}) + \frac{U_0}{2}\int d\vec{r}\hat{\Psi}^\dagger(\vec{r})\hat{\Psi}^\dagger(\vec{r})\hat{\Psi}(\vec{r})\hat{\Psi}(\vec{r}) \\ &- \mu\int d\vec{r}\hat{\Psi}^\dagger(\vec{r})\hat{\Psi}(\vec{r}) \end{aligned} \tag{4.1}$$

As in Eq. (3.5), we decompose the field operator $\hat{\Psi}(\vec{r})$ as follows

$$\hat{\Psi}(\vec{r}) = \Psi(\vec{r}) + \hat{\Phi}(\vec{r}). \tag{4.2}$$

Inserting Eq. (4.2) into Hamiltonian (4.1) and neglecting terms in $\hat{\Phi}(\vec{r})$ higher than quadratic yields the following expression for $\hat{K}$

$$\begin{aligned}\hat{K} = &\int d\vec{r}\Psi^*(\vec{r})\left(\hat{H}_0 - \mu + \frac{1}{2}U_0|\Psi(\vec{r})|^2\right)\Psi(\vec{r}) \\ &+ \int d\vec{r}\Psi^*(\vec{r})\left(\hat{H}_0 - \mu + U_0|\Psi(\vec{r})|^2\right)\hat{\Phi}(\vec{r}) \\ &+ \int d\vec{r}\hat{\Phi}^\dagger(\vec{r})\left(\hat{H}_0 - \mu + U_0|\Psi(\vec{r})|^2\right)\Psi(\vec{r}) \\ &+ \int d\vec{r}\hat{\Phi}^\dagger(\vec{r})\left(\hat{H}_0 - \mu + 2U_0|\Psi(\vec{r})|^2\right)\hat{\Phi}(\vec{r}) \\ &+ \frac{1}{2}U_0\left(\int d\vec{r}\hat{\Phi}^\dagger(\vec{r})\Psi(\vec{r})^2\hat{\Phi}^\dagger(\vec{r}) + \int d\vec{r}\hat{\Phi}(\vec{r})\Psi^*(\vec{r})^2\hat{\Phi}(\vec{r})\right). \end{aligned} \tag{4.3}$$

The first term in the above equation is a c-number and the second and third terms will vanish identically if $\Psi(\vec{r})$ satisfies the GP equation. The Bogoliubov-approximate grand canonical Hamiltonian $\hat{K}_B$ then takes the form (to within a c-number)

$$\begin{aligned}\hat{K}_B = &\int d\vec{r}\hat{\Phi}^\dagger(\vec{r})\left(\hat{H}_0 - \mu + 2U_0|\Psi(\vec{r})|^2\right)\hat{\Phi}(\vec{r}) \\ &+ \frac{1}{2}U_0\int d\vec{r}\hat{\Phi}^\dagger(\vec{r})\Psi(\vec{r})^2\hat{\Phi}^\dagger(\vec{r}) + \frac{1}{2}U_0\int d\vec{r}\hat{\Phi}(\vec{r})\Psi^*(\vec{r})^2\hat{\Phi}(\vec{r}). \end{aligned} \tag{4.4}$$

The Bogoliubov Hamiltonian can be cast into the form for that of a collection of non-interacting quasi-particles by the following Bogoliubov transformation

$$\hat{\Phi}(\vec{r}) = \sum_j \left(u_j(\vec{r})\hat{\alpha}_j + v_j^*(\vec{r})\hat{\alpha}_j^\dagger \right),$$
$$\hat{\Phi}^\dagger(\vec{r}) = \sum_j \left(u_j^*(\vec{r})\hat{\alpha}_j^\dagger + v_j(\vec{r})\hat{\alpha}_j \right). \tag{4.5}$$

Here $u_j(\vec{r})$ and $v_j(\vec{r})$ are some complete set of functions to be determined and $\hat{\alpha}_j^\dagger$ and $\hat{\alpha}_j$ are quasi-particle creation and destruction operators and the implicit assumption is made that the condensate wave function is not included in the sum. The quasi-particle operators satisfy the usual commutation relations for boson creation and destruction operators

$$\left[\hat{\alpha}_j, \hat{\alpha}_{j'}^\dagger\right] = \delta_{jj'}, \qquad [\hat{\alpha}_j, \hat{\alpha}_{j'}] = 0, \qquad \left[\hat{\alpha}_j^\dagger, \hat{\alpha}_{j'}^\dagger\right] = 0. \tag{4.6}$$

The reduction of $\hat{K}_B$ to a collection of non-interacting quasi-particles occurs if the $u_j(\vec{r})$ and $v_j(\vec{r})$ satisfy the following Bogoliubov equations

$$\hat{\mathcal{L}}u_j(\vec{r}) + U_0\Psi(\vec{r})^2 v_j(\vec{r}) = E_j u_j(\vec{r}),$$
$$\hat{\mathcal{L}}v_j(\vec{r}) + U_0\Psi^*(\vec{r})^2 u_j(\vec{r}) = -E_j v_j(\vec{r}), \tag{4.7}$$

where

$$\hat{\mathcal{L}} = \hat{H}_0 - \mu + 2U_0|\Psi(\vec{r})|^2. \tag{4.8}$$

The final form of $\hat{K}_B$ is

$$\hat{K}_B = \sum_j E_j \hat{\alpha}_j^\dagger \hat{\alpha}_j. \tag{4.9}$$

The same Bogoliubov equations can also be obtained by linear-response analysis of the time-dependent GP equation (3.7). Namely, one can look for solution of the form

$$\Psi(\vec{r}, t) = e^{-i\mu t/\hbar}\left(\Psi(\vec{r}) + u(\vec{r})e^{-i\omega_p t} + v^*(\vec{r})e^{i\omega_p t}\right), \tag{4.10}$$

which corresponds to small oscillations of the order parameter around the ground state value. Here ω_p is the probe frequency. By substituting Eq. (4.10) into Eq. (3.7) and keeping terms linear in the complex functions $u(\vec{r})$ and $v(\vec{r})$, we get again the Bogoliubov equations (4.7).

4.3 Expansion Method

In this section, we will describe how to solve Eqs. (4.7) using the expansion method. We first expand $u_j(\vec{r})$ and $v_j(\vec{r})$ in the eigenstates of $\hat{H}_0$ as follows

$$\begin{aligned} u_j(\vec{r}) &= \sum_\nu b_\nu \psi_\nu(\vec{r}), \\ v_j(\vec{r}) &= \sum_\nu c_\nu \psi_\nu(\vec{r}), \end{aligned} \tag{4.11}$$

where the summations run up to N'_{basis}. We substitute the above equations and the expansion for the ground state of condensate Eq. (3.47) into Eqs. (4.7) and take the scalar product with the complex conjugate of the basis functions. Then one can have the following equations

$$\begin{aligned} \sum_{\nu'} L_{\nu,\nu'} b_{\nu'} + \sum_{\nu'} M_{\nu,\nu'} c_{\nu'} &= E_j b_\nu, \\ \sum_{\nu'} L_{\nu,\nu'} c_{\nu'} + \sum_{\nu'} M_{\nu,\nu'} b_{\nu'} &= -E_j c_\nu, \end{aligned} \tag{4.12}$$

where $L_{\nu,\nu'}$ is defined as

$$L_{\nu,\nu'} = \int d\vec{r} \psi^*_\nu(\vec{r}) \hat{\mathcal{L}} \psi_{\nu'}(\vec{r}), \tag{4.13}$$

and $M_{\nu,\nu'}$ is given by

$$M_{\nu,\nu'} = N_0 U_0 \sum_{\nu_1,\nu_2} a_{\nu_1} a_{\nu_2} \int d\vec{r} \psi^*_\nu(\vec{r}) \psi_{\nu_1}(\vec{r}) \psi_{\nu_2}(\vec{r}) \psi_{\nu'}(\vec{r}). \tag{4.14}$$

Here subscripts ν_1 and ν_2 are for the expansion of the ground state wave function in Eq. (4.7) and thus have the forms $\nu_1 = (n_{\rho 1}, 0, n_{z1})$ and $\nu_2 = (n_{\rho 2}, 0, n_{z2})$ because

the ground state wave function can be taken as real and angle independent. Here a_{ν_1} and a_{ν_2} are those expansion coefficients obtained in section 3.5. Now it is clear that the problem of solving Eqs. (4.7) has been converted to the following generalized matrix eigenvalue equation having the form

$$\begin{pmatrix} L & M \\ M & L \end{pmatrix} \begin{pmatrix} B \\ C \end{pmatrix} = E \begin{pmatrix} 1 & 0 \\ 0 & -1 \end{pmatrix} \begin{pmatrix} B \\ C \end{pmatrix}, \tag{4.15}$$

where L and M are square matrices of order N'_{basis}. B and C are N'_{basis}-component column vector containing the coefficients in the basis set expansion of $u_j(\vec{r})$ and $v_j(\vec{r})$. More detail of the expansion method can be found in Ref. [14, 15, 16]. As mentioned above, the basis functions used for the expansion of the ground state wave function are those with $m = 0$, thus to get non-zero elements for $M_{\nu,\nu'}$, ν and ν' must have the same m. This implies that the generalized eigenvalue problem of Eq. (4.15) can be solved in sub-spaces according to the quantum number m. In the JILA experiment [17], collective modes of condensate are excited by applying a small time-dependent perturbation to the trapping potential. The response of the condensate depends on the symmetry of the driving force as well as the driving frequency ω_p. Perturbations with two different symmetries can be generated, which are labeled as $m = 0$ and $m = 2$, where m is the angular momentum projection onto z axis. The $m = 1$ mode corresponds to rigid-body center-of-mass motion, which coincides exactly with the first excited state of the bare trap. In Fig. 4.1, we plot the collective excitation frequencies for $m = 0, 1, 2$ obtained numerically as a function of number of particles in the condensate. The parameters used correspond to the experiment performed at JILA. We also listed in Table 4.1 the comparison between the theoretical predictions and the experimental values of the lowest three excitation frequencies for $N_0 = 4500$. As one can see, the agreement is excellent.

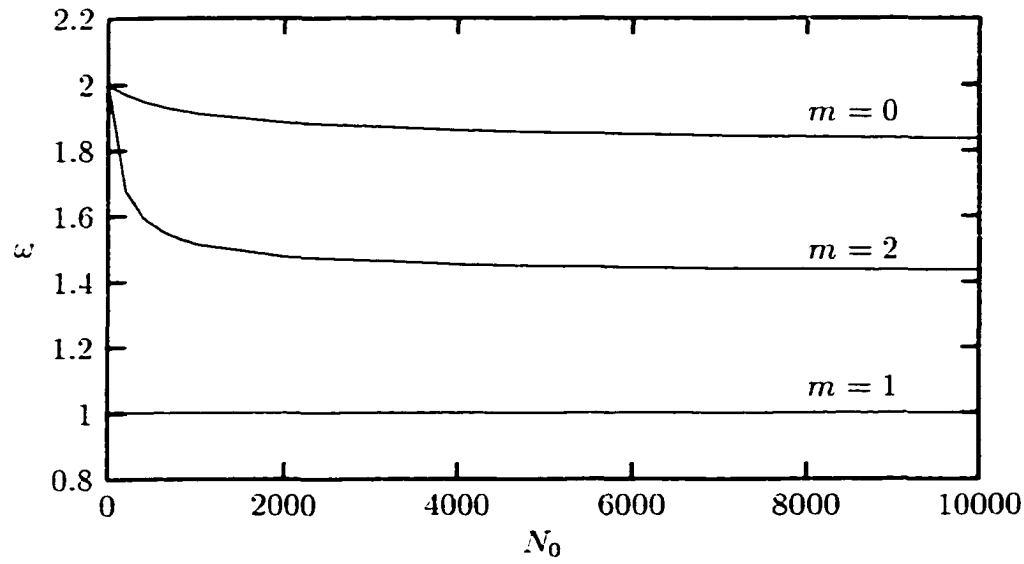

Figure 4.1: The lowest three calculated excitation frequencies in the unit of ω_ρ for N_0 ^{87}Rb atoms in the JILA trap with $\omega_\rho = 2\pi \times 132$Hz and $\lambda = \sqrt{8}$.

N_0	m	ω_e	ω_t	% diff.
4500	0	1.84±0.01	1.86	1.1
4500	2	1.43±0.01	1.45	1.4

Table 4.1: A comparison between the theoretical prediction and the JILA experiment results. ω_e and ω_t are the experimental and theoretical values, respectively.

4.4 Simulation of Large Amplitude Oscillations

The experimental observations of collective excitations of the BEC also stimulate our interest in the dynamical properties of a Bose condensate. It has been suggested by Smerzi and Fontoni [18] that even at $T = 0$, when the amplitude of the oscillation is large, a damping of monopole moment oscillation can occur and will be observed. In the experiment, the collective monopole vibrations have been induced using a time-dependent magnetic field acting on the $x - y$ plane during the first 0.05s. In order to simulate exactly the experiments, we solve the time-dependent GP equation (3.7) by adding a time-dependent potential $V_d = \frac{1}{2}m_0\omega^2(t)\rho^2$ that oscillates with a frequency equal to that of the excitation under study and with an amplitude equal to 1.5% and 4.5% of the radial spring constant. The oscillations induced by the driving potential increase rapidly in amplitude during $t = 0.05$s. Then the system oscillates freely in the anisotropic external trap.

We need an extremely stable numerical scheme to simulate the time evolution of the time-dependent GP equation. One approach is the classical Crank-Nicholson scheme combined with ADI method, which has been used in Chapter. 3 in imaginary time to obtain the ground state of the condensate. It turns out that Crank-Nicholson is also very stable for the real time simulation problem, but it is not accurate enough for very long time of propagation, because it is only accurate to the 2nd order in evaluating the spatial derivatives [1]. Fast Fourier transformation turns out to be a much more accurate method to calculate the spatial derivatives as we will describe below. To search for a better numerical scheme, we will formulate the problem into a

[1] Improved ADI method is reported in Ref. [19]. The authors claim that the method is stable and highly accurate.

more general form to get a better understanding of the numerical task involved. For a comprehensive review about the numerical solution of time-dependent Schrödinger equation, see Ref. [20, 21]. The task is to numerically propagate the following initial value problem

$$i\hbar\frac{\partial\Psi(\vec{r},t)}{\partial t} = \hat{H}(t)\Psi(\vec{r},t), \tag{4.16}$$

where $\hat{H}(t)$ is the Hamiltonian operator including the nonlinear term. Given the initial wave function, the time evolution involves the calculation of the $\hat{H}(t)\Psi(\vec{r},t)$ as well as the time derivative of the wave function. The evaluation of $\hat{H}(t)\Psi(\vec{r},t)$ consists of two parts: $\hat{T}\Psi(\vec{r},t)$ and $\hat{V}\Psi(\vec{r},t)$, where $\hat{T}$ is the kinetic operator and $\hat{V}$ is the potential energy operator. The operation $\hat{V}\Psi(\vec{r},t)$ is a local one, which is just a simple multiplication at each grid point. The operation of $\hat{T}\Psi(\vec{r},t)$ is the most time consuming part of any numerical calculation of this type. The operator $\hat{T}$ is non-local in the coordinate representation. The most commonly used schemes for computing this operation of the wave function are 3-point finite difference scheme and the fast Fourier transform (FFT) method. Combined with different implementations of the time derivative of the wave function, we will have different numerical schemes for solving this type of initial value problems. In the 3-point finite difference scheme, the second order spatial derivative of the wave function $\Psi(x)$ at $x = x_j$ in one dimension, for example, is represented as follows

$$\frac{d^2\Psi(x_j)}{dx^2} = \frac{\Psi_{j+1} - 2\Psi_j + \Psi_{j-1}}{\Delta x^2}. \tag{4.17}$$

The FFT method of computing the second order derivative of the wave function involves Fourier transforming the coordinate space wave function to momentum space, multiplying it by $(ik)^2$ (where k is the wave number), and transforming it

back to the coordinate space by inverse Fourier transform as indicated below

$$\Psi(k) = \frac{1}{\sqrt{2\pi}} \int_{-\infty}^{\infty} dx \Psi(x) e^{-ikx}, \tag{4.18}$$

$$\Psi(x) = \frac{1}{\sqrt{2\pi}} \int_{-\infty}^{\infty} dk \Psi(k) e^{ikx}, \tag{4.19}$$

$$\frac{d\Psi(x)}{dx} = \frac{1}{\sqrt{2\pi}} \int_{-\infty}^{\infty} dk \Psi(k)(ik) e^{ikx}, \tag{4.20}$$

$$\frac{d^2\Psi(x)}{dx^2} = \frac{1}{\sqrt{2\pi}} \int_{-\infty}^{\infty} dk \Psi(k)(ik)^2 e^{ikx}. \tag{4.21}$$

Since the kinetic energy operator is local in the momentum space, its action on the wave function is evaluated very accurately, just as the case of the potential energy operator in the coordinate space. The method requires the wave function to satisfy periodic boundary conditions and it is exact for band-limited functions. If the function is not band-limited or periodic boundary conditions are not satisfied, the wave function would wrap around at an opposite side introducing errors in the calculation. An attractive feature of the method is its computational scaling property with respect to the number of grid points N. Computational time increases slowly as $N \log N$. Once the appropriate spatial discretisation scheme is chosen, and the initial wave function on the grid is set up, the next step is the time propagation of the wave function. The time-dependent Schrödinger equation has the following formal solution

$$\Psi(t) = \hat{U}(t)\Psi(0) = \hat{T}_t \exp\left(-\frac{i}{\hbar}\int_0^t \hat{H}(t')dt'\right)\Psi(0), \tag{4.22}$$

where $\hat{T}_t$ is the time ordering operator. A simple solution to the time problem is to break up the total evolution operator into small increments of duration Δt in which the variation of the Hamiltonian operator is small

$$\hat{U}(t) = \prod_{n=0}^{N-1} \hat{U}(n\Delta t + \Delta t, n\Delta t), \tag{4.23}$$

where $\Delta t = t/N$ and

$$\hat{U}(n\Delta t + \Delta t, n\Delta t) = e^{-i\hat{H}(n\Delta t)\Delta t/\hbar}. \tag{4.24}$$

The difference between various approximations to the propagation schemes can be traced to the way the exponentiation is approximated. If we difference the operator $\exp(-i\hat{H}\Delta t/\hbar)$ as follows

$$e^{-i\hat{H}\Delta t/\hbar} = \frac{1 - i\hat{H}\Delta t/2\hbar}{1 + i\hat{H}\Delta t/2\hbar}, \tag{4.25}$$

we will have

$$\left(1 + i\hat{H}\Delta t/2\hbar\right)\Psi_j^{n+1} = \left(1 - i\hat{H}\Delta t/2\hbar\right)\Psi_j^n. \tag{4.26}$$

On replacing $\hat{H}$ by its 3-point finite difference approximation, we have a complex tridiagonal system to solve. This is just the Crank-Nicholson scheme. Another scheme for time propagation is to expand the evolution operator $\hat{U} = \exp(-i\hat{H}\Delta t/\hbar)$ in a Taylor series as follows

$$e^{-i\hat{H}\Delta t/\hbar} = 1 - i\hat{H}\Delta t/\hbar + \cdots. \tag{4.27}$$

It has been found that a numerical algorithm based on this expansion is not stable. The instability comes about because the scheme does not conserve the time reversal symmetry of the Schrödinger equation. With a symmetric modification of the expansion, stability is obtained. One way to formulate the scheme is to use second-order differencing (SOD) to approximate the time derivative as below

$$i\hbar\frac{\Psi^{n+1} - \Psi^{n-1}}{2\Delta t} = \hat{H}\Psi^n. \tag{4.28}$$

and the explicit second-order propagation is obtained

$$\Psi(t + \Delta t) \approx \Psi(t) - 2i\hat{H}\Psi(t)/\hbar. \tag{4.29}$$

Because the Hamiltonian is hermitian, the SOD propagation scheme preserves norm and energy. This methods, unfortunately, requires a small time increment for numerical stability as otherwise contributions from higher-order terms in Δt increase and errors accumulate. It is possible to work out the stability criteria for the step-size by taking into account the maximum energy on the grid introduced by the spatial discretisation. If the Fourier method is used for the spatial discretisation, the maximum energy on the grid is $E_{max} = T_{max} + V_{max}$, where $T_{max} = \hbar^2\pi^2/2m_0(\Delta x)^2$ and V_{max} is the maximum potential energy on the grid. It follows from the uncertainty principle relating time and energy that the time increment should be smaller than a critical value $\Delta t_c = \hbar/E_{max}$. Any time-step bigger than this would make the propagation numerically unstable. For practical calculation, it is recommended that $\Delta t = \Delta t_c/5$ be used. The method has its advantage in that it is easy to implement and can be used even when the Hamiltonian is time-dependent.

It is worth mentioning that there are a class of so called global propagation schemes, which are extremely accurate and stable for the Hamiltonian without explicit time dependence. The main idea behind global propagators is to use a polynomial expansion of the exponential in the evolution operator

$$\hat{U}(t) = \sum_{n=0}^{N} a_n P_n\left(-\frac{i}{\hbar}\hat{H}t\right). \tag{4.30}$$

Here $P_n(z)$ are an orthonormal complete set of polynomials. Global propagators can use very long time steps, sometimes a single time step to complete the calculation. One commonly used global propagator is the Chebyshev scheme, which uses the Chebyshev polynomial expansion in Eq. (4.30). We will not go into details of the Chebyshev scheme, since it is not suitable for our problem, which depends on the time explicitly.

We have used the SOD scheme combined with FFT method for computing the spatial derivatives to simulate the large amplitude oscillation of a driven condensate. The results are presented in Fig. 4.2 and Fig. 4.3. In Fig. 4.2, we plot the monopole

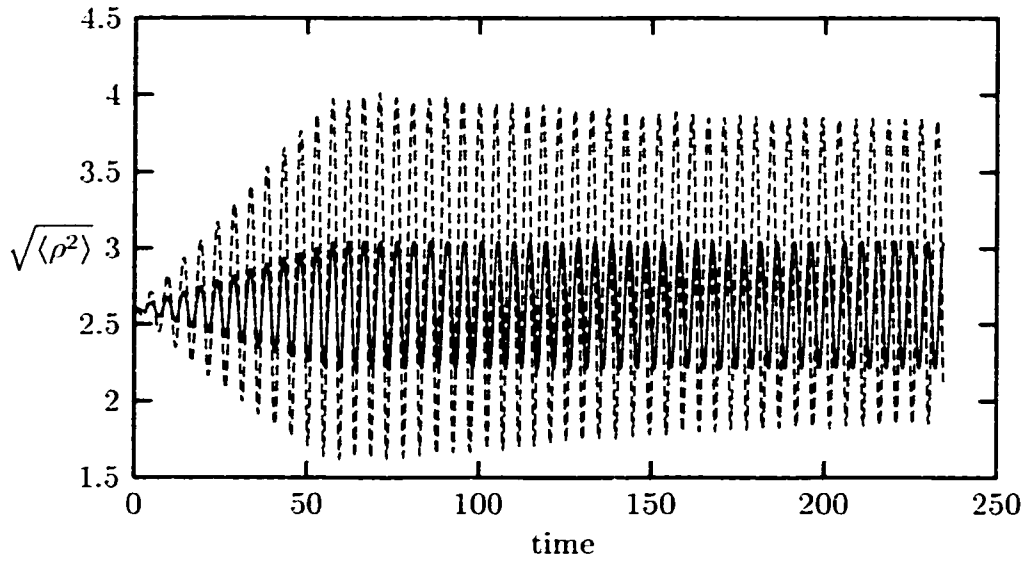

Figure 4.2: Monopole moment (in arbitrary unit) versus time for a system of $N_0 = 4500$ ^{87}Rb atoms in JILA trap with $\omega_\rho = 2\pi \times 132$Hz and $\lambda = \sqrt{8}$. The time is in the unit of $1/\omega$. The solid line and the dashed line correspond to driving amplitude of 1.5% and 4.5% of the spring constant, respectively.

moment as a function of time. As shown clearly, the oscillation amplitude increases steadily during the driving. When the driving amplitude is 1.5% of the spring constant, there is no damping of the excited mode after driving is switched off. This is not in agreement with the results reported in Ref. [18]. To make sure our result is correct, we plot the total energy per particle during the time evolution in Fig. 4.3. The energy increases during the drive and remains constant when driving is turned off as expected. However, there is no result about the energy versus time

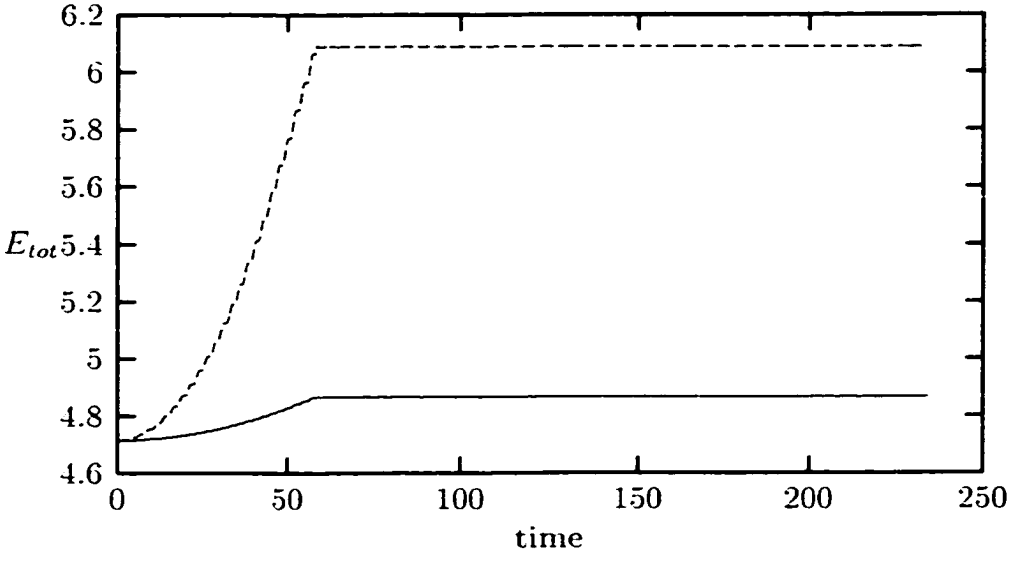

Figure 4.3: The total energy per particle during the time-evolution. The energy is in the unit of $\hbar\omega$ and the time is in the unit of $1/\omega$. The solid line and the dashed line correspond to driving amplitude of 1.5% and 4.5% of the spring constant, respectively.

reported in Ref. [18], so we can not verify if the energy per particle is conserved in their calculation. When the driving amplitude is 4.5% of the spring constant, there is small damping for the monopole moment.

Chapter 5

Properties of BEC at Finite Temperature

5.1 Introduction

In this chapter, we extend the Bogoliubov theory to non-zero temperature using the Popov approximation. When $k_B T \gg \hbar\omega$, the semiclassical approximation can be used. We describe the self-consistent procedure to solve the semiclassical equations for the ground state wave function and the excitation states.

5.2 Popov Approximation

To obtain the excitations at non-zero temperature, we use the Bogoliubov theory described in Chapter 4 for zero temperature extended to finite temperature [22]. For a review of the theory of excitations of the condensate at finite temperature, see Ref. [23]. The starting point is still the grand canonical Hamiltonian (4.1). Using again the decomposition (4.2), the operators in the interaction term becomes

$$\begin{aligned} &\hat{\Psi}^\dagger(\vec{r})\hat{\Psi}^\dagger(\vec{r})\hat{\Psi}(\vec{r})\hat{\Psi}(\vec{r}) \\ &= |\Psi(\vec{r})|^4 + 2|\Psi(\vec{r})|^2\Psi^*(\vec{r})\hat{\Phi}(\vec{r}) + 2|\Psi(\vec{r})|^2\Psi(\vec{r})\hat{\Phi}^\dagger(\vec{r}) \end{aligned}$$

$$+ 4|\Psi(\vec{r})|^2\hat{\Phi}^\dagger(\vec{r})\hat{\Phi}(\vec{r}) + \Psi^*(\vec{r})^2\hat{\Phi}(\vec{r})\hat{\Phi}(\vec{r}) + \Psi(\vec{r})^2\hat{\Phi}^\dagger(\vec{r})\hat{\Phi}^\dagger(\vec{r})$$
$$+ 2\Psi^*(\vec{r})\hat{\Phi}^\dagger(\vec{r})\hat{\Phi}(\vec{r})\hat{\Phi}(\vec{r}) + 2\Psi(\vec{r})\hat{\Phi}^\dagger(\vec{r})\hat{\Phi}^\dagger(\vec{r})\hat{\Phi}(\vec{r}) + \hat{\Phi}^\dagger(\vec{r})\hat{\Phi}^\dagger(\vec{r})\hat{\Phi}(\vec{r})\hat{\Phi}(\vec{r}). \quad (5.1)$$

In the following, the cubic and quartic terms in $\hat{\Phi}(\vec{r})$, $\hat{\Phi}^\dagger(\vec{r})$ in the last line of the above equation will be treated in the mean-field approximation. For the cubic terms one gets

$$\hat{\Phi}^\dagger(\vec{r})\hat{\Phi}(\vec{r})\hat{\Phi}(\vec{r}) \approx 2\langle\hat{\Phi}^\dagger(\vec{r})\hat{\Phi}(\vec{r})\rangle\hat{\Phi}(\vec{r}) \equiv 2n_T(\vec{r})\hat{\Phi}(\vec{r}),$$
$$\hat{\Phi}^\dagger(\vec{r})\hat{\Phi}^\dagger(\vec{r})\hat{\Phi}(\vec{r}) \approx 2\langle\hat{\Phi}^\dagger(\vec{r})\hat{\Phi}(\vec{r})\rangle\hat{\Phi}^\dagger(\vec{r}) \equiv 2n_T(\vec{r})\hat{\Phi}^\dagger(\vec{r}), \quad (5.2)$$

where $n_T(\vec{r})$ is the non-condensate density of particles at temperature T. Whereas the quartic term becomes

$$\hat{\Phi}^\dagger(\vec{r})\hat{\Phi}^\dagger(\vec{r})\hat{\Phi}(\vec{r})\hat{\Phi}(\vec{r}) \approx 4\langle\hat{\Phi}^\dagger(\vec{r})\hat{\Phi}(\vec{r})\rangle\hat{\Phi}^\dagger(\vec{r})\hat{\Phi}(\vec{r})$$
$$\equiv 4n_T(\vec{r})\hat{\Phi}^\dagger(\vec{r})\hat{\Phi}(\vec{r}). \quad (5.3)$$

To obtain the mean-field factorization we have neglected the terms proportional to the anomalous non-condensate density $m_T(\vec{r}) = \langle\hat{\Phi}(\vec{r})\hat{\Phi}(\vec{r})\rangle$ and its complex conjugate. This approximation corresponds to the so called Popov approximation. The grand-canonical Hamiltonian can be written as the sum of four terms

$$\hat{K} = \hat{K}_0 + \hat{K}_1 + \hat{K}_1^\dagger + \hat{K}_2. \quad (5.4)$$

The first term $\hat{K}_0$ contains only the condensate wave function $\Psi(\vec{r})$

$$\hat{K}_0 = \int d\vec{r}\Psi^*(\vec{r})\left(\hat{H}_0 - \mu + \frac{U_0}{2}n_0(\vec{r})\right)\Psi(\vec{r}), \quad (5.5)$$

where we have introduced the condensate density $n_0(\vec{r}) = |\Psi(\vec{r})|^2$. The $\hat{K}_1$ and $\hat{K}_1^\dagger$ terms are linear in the operators $\hat{\Phi}(\vec{r})$, $\hat{\Phi}^\dagger(\vec{r})$

$$\hat{K}_1 = \int d\vec{r}\hat{\Phi}^\dagger(\vec{r})\left[\hat{H}_0 - \mu + U_0(n_0(\vec{r}) + 2n_T(\vec{r}))\right]\Psi(\vec{r}), \quad (5.6)$$

and finally $\hat{K}_2$ is quadratic in $\hat{\Phi}(\vec{r})$, $\hat{\Phi}^\dagger(\vec{r})$

$$\hat{K}_2 = \int d\vec{r}\hat{\Phi}^\dagger(\vec{r})\hat{\mathcal{L}}\hat{\Phi}(\vec{r}) + \frac{U_0}{2}\int d\vec{r}\Psi(\vec{r})^2\hat{\Phi}^\dagger(\vec{r})\hat{\Phi}^\dagger(\vec{r}) + \frac{U_0}{2}\int d\vec{r}\Psi^*(\vec{r})^2\hat{\Phi}(\vec{r})\hat{\Phi}(\vec{r}), \tag{5.7}$$

where we have introduced the hermitian operator

$$\hat{\mathcal{L}} = \hat{H}_0 - \mu + 2U_0 n(\vec{r}), \tag{5.8}$$

with

$$n(\vec{r}) = n_0(\vec{r}) + n_T(\vec{r}). \tag{5.9}$$

The $\hat{K}_1$, $\hat{K}_1^\dagger$ terms vanish if $\Psi(\vec{r})$ is the solution of the equation for the condensate wave function

$$\left[\hat{H}_0 - \mu + U_0(n_0(\vec{r}) + 2n_T(\vec{r}))\right]\Psi(\vec{r}) = 0. \tag{5.10}$$

The quadratic term $\hat{K}_2$ can be diagonalized as in Chapter 4 by means of the Bogoliubov transformation (4.5) if $u_j(\vec{r})$ and $v_j(\vec{r})$ satisfy the following Bogoliubov equations

$$\begin{aligned}\hat{\mathcal{L}}u_j(\vec{r}) + U_0 n_0(\vec{r})v_j(\vec{r}) &= E_j u_j(\vec{r}),\\ \hat{\mathcal{L}}v_j(\vec{r}) + U_0 n_0(\vec{r})u_j(\vec{r}) &= -E_j v_j(\vec{r}).\end{aligned} \tag{5.11}$$

5.3 Semiclassical Approximation

The coupled equations can be solved very easily using the semi-classical approximation with

$$\begin{aligned}u_j(\vec{r}) &= u(\vec{p},\vec{r})e^{i\phi(\vec{r})},\\ v_j(\vec{r}) &= v(\vec{p},\vec{r})e^{-i\phi(\vec{r})},\end{aligned} \tag{5.12}$$

where the momentum of the elementary excitation is fixed by the gradient of the phase $\vec{p} = \hbar\nabla\phi(\vec{r})$ and satisfies the condition $p \gg \hbar/d$ [24]. $u(\vec{p},\vec{r})$ and $v(\vec{p},\vec{r})$ are real functions. We also assume that $u(\vec{p},\vec{r})$, $v(\vec{p},\vec{r})$ are smooth functions of $\vec{r}$ on length scales of the order of the harmonic oscillator length d. Since the typical size of the thermally excited cloud is of the order of the classical thermal radius $\sqrt{2k_BT/m_0\omega^2}$, the semi-classical approximation makes sense only if $k_BT \gg \hbar\omega$. Using Eq. (2.21), we can easily estimate that for condensate with number of particles ranging from 5×10^3 to 5×10^6, $k_BT_c^0/\hbar\omega$ ranges from 16 to 160, which implies that semi-classical approximation can be used for large range of temperatures. The sum over the quantum state j labeling the solutions of the Bogoliubov equations is replaced by the integral $\int d\vec{p}/(2\pi\hbar)^3$. By neglecting derivatives of $u(\vec{r})$ and $v(\vec{r})$ and second derivatives of $\phi(\vec{r})$ it is possible to rewrite the Bogoliubov-type equations in the semi-classical form

$$\left(\frac{p^2}{2m} + V_{ext}(\vec{r}) - \mu + 2U_0n(\vec{r})\right)u(\vec{p},\vec{r}) + U_0n_0(\vec{r})v(\vec{p},\vec{r}) = \varepsilon(\vec{p},\vec{r})u(\vec{p},\vec{r}),$$
$$\left(\frac{p^2}{2m} + V_{ext}(\vec{r}) - \mu + 2U_0n(\vec{r})\right)v(\vec{p},\vec{r}) + U_0n_0(\vec{r})u(\vec{p},\vec{r}) = -\varepsilon(\vec{p},\vec{r})v(\vec{p},\vec{r}) \quad (5.13)$$

The solution of these equations is easily obtained and one finds the following result for the spectrum of the elementary excitations

$$\varepsilon(\vec{p},\vec{r}) = \left[\left(\frac{p^2}{2m} + V_{ext}(\vec{r}) - \mu + 2U_0n(\vec{r})\right)^2 - U_0^2n_0^2(\vec{r})\right]^{\frac{1}{2}}, \quad (5.14)$$

with the $u(\vec{p},\vec{r})$ and $v(\vec{p},\vec{r})$ given by

$$u^2(\vec{p},\vec{r}) = \frac{p^2/2m + V_{ext}(\vec{r}) - \mu + 2U_0n(\vec{r}) + \varepsilon(\vec{p},\vec{r})}{2\varepsilon(\vec{p},\vec{r})},$$
$$v^2(\vec{p},\vec{r}) = \frac{p^2/2m + V_{ext}(\vec{r}) - \mu + 2U_0n(\vec{r}) - \varepsilon(\vec{p},\vec{r})}{2\varepsilon(\vec{p},\vec{r})},$$
$$u(\vec{p},\vec{r})v(\vec{p},\vec{r}) = -\frac{U_0n_0(\vec{r})}{2\varepsilon(\vec{p},\vec{r})}. \quad (5.15)$$

The knowledge of the excitation spectrum fixes the distribution function of the elementary excitations

$$f(\vec{p},\vec{r}) = \frac{1}{\exp\left[\varepsilon(\vec{p},\vec{r})/k_B T\right] - 1}, \tag{5.16}$$

in terms of which one can calculate the distribution function of thermally excited particles

$$\begin{aligned} F(\vec{p},\vec{r}) &= \left(u^2(\vec{p},\vec{r}) + v^2(\vec{p},\vec{r})\right) f(\vec{p},\vec{r}) \\ &= -\left(\frac{\partial\varepsilon(\vec{p},\vec{r})}{\partial\mu}\right)_{n_0,n_T} f(\vec{p},\vec{r}), \end{aligned} \tag{5.17}$$

with

$$\left(\frac{\partial\varepsilon(\vec{p},\vec{r})}{\partial\mu}\right)_{n_0,n_T} = -\frac{p^2/2m + V_{ext}(\vec{r}) - \mu + 2U_0 n(\vec{r})}{\varepsilon(\vec{p},\vec{r})}. \tag{5.18}$$

The thermal density at $\vec{r}$ is given by

$$n_T(\vec{r}) = \int d\vec{p}\frac{F(\vec{p},\vec{r})}{(2\pi\hbar)^3}, \tag{5.19}$$

in terms of which we can calculate the total number of atoms out of the condensate $N_T = \int d\vec{r} n_T(\vec{r})$.

5.4 Self-consistent Numerical Calculation

To obtain the thermodynamic properties at $T < T_c^0$, we need to follow the self-consistent numerical procedure outlined here. (a) Given $T < T_c^0$ ($k_B T \gg \hbar\omega$) and the total number of particles in and out of the condensate N. The equation for the condensate wave function Eq. (5.10) is first solved using the steepest descent method, for the condensate wave function $\Psi(\vec{r})$ and the chemical potential μ, while keeping the total number of atoms fixed. (b) The condensate wave function and the

chemical potential found in the last step are used to calculate the excitation energy based on Eq. (5.14), which yield a non-condensate density $n_T(\vec{r})$ through Eq. (5.19). (c) From the new thermal density, the total number of particle out of the condensate N_T and the number of atoms in the condensate $N_0 = N - N_T$ can be calculated. The condensate N_0/N fraction can also be obtained. Steps (a)-(c) are repeated until convergence is reached. We stop the iterative procedure when successive iterations give values for the chemical potential and the condensate fraction differing by less than a few parts in 10^3. In Fig. 5.1, we show the condensate fraction as a function of the temperature. From Fig. 5.1, we can see clearly that the effect of the interaction

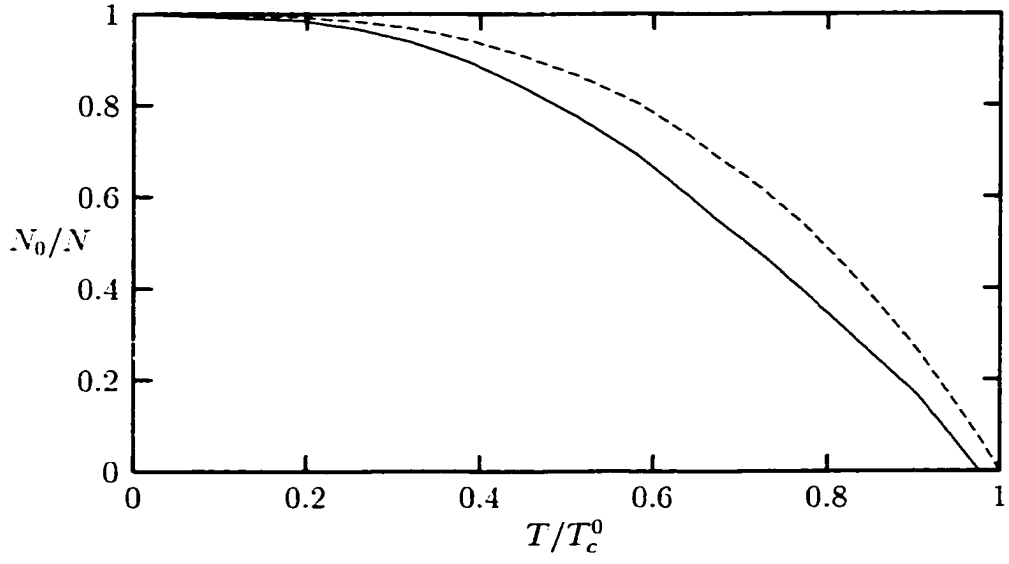

Figure 5.1: Condensate fraction as a function of T/T_c^0. Solid line correspond to $N = 4500$ ^{87}Rb atoms in the trap with $\omega_\rho = 2\pi \times 132$Hz and $\lambda = \sqrt{8}$. Dashed line corresponds to result for ideal Bose gases trapped in the same harmonic potential ($a = 0$).

is to lower the transition temperature compared to the ideal Bose gases.

Chapter 6

Properties of Double Condensates

6.1 Introduction

In this chapter, we will describe some important properties of double condensates, which could be mixture of different kinds of atoms or the same type of atoms in different quantum states. For a review on experiments with double condensates, see Ref. [25]. A typical experiment involving mixed condensates done at JILA begins with a sample of approximately 5×10^5 spin-aligned, Bose-condensed ^{87}Rb atoms at a temperature of less than 50 nK, confined in a 3D harmonic magnetic potential at density 1×10^{14} cm^{-3}. The number density of noncondensed atoms is a factor of 30 or more smaller. The ground state of a ^{87}Rb atom is split in a magnetic field into eight levels by hyperfine and Zeeman interactions. It is with states $|1\rangle$ ($|F = 1, m = -1\rangle$) and $|2\rangle$ ($|F = 2, m = 1\rangle$) that most of the mixed-fluids experiments were performed. Using a two-photon pulse, any fraction of the atoms that are in state $|1\rangle$ can be transferred into state $|2\rangle$. In principal, a mixture may also be obtained using two different types of atoms, for example, Na-Rb mixture. The $|1\rangle$ and $|2\rangle$ components of the condensate are distinguishable, namely, the components do not spontaneously interconvert at experimental energy scales, and the components can be selectively

detected and imaged. We will first present the coupled GP equations obtained from the mean field theory extended to the double components BEC systems. The Thomas-Fermi approximation is then considered for the double condensates. We have found that the wave functions obtained from the Thomas-Fermi approximation are not in agreement with the experiments and numerical calculations in contrast with the single component BEC system, for which the Thomas-Fermi approximation provides excellent results for the ground state. The numerical solutions for the double condensate ground state are found for the trapping potentials with both zero and small displacement. In the following work, the dynamics of component separation of the double condensates is simulated using coupled time-dependent GP equations, the results are in fairly good agreement with the JILA experiment.

6.2 Ground State of Double Condensates

We can easily extend the mean field theory presented in Chapter 3 for the single component condensate to double condensate systems. For atoms with masses m_1 and m_2 confined in the traps $V_1(\vec{r})$ and $V_2(\vec{r})$ respectively, the equations derived are now a pair of coupled GP equations for the order parameters $\Psi_1(\vec{r},t)$ and $\Psi_2(\vec{r},t)$,

$$i\hbar\frac{\partial\Psi_1(\vec{r},t)}{\partial t} = \left(-\frac{\hbar^2}{2m_1}\nabla^2 + V_1(\vec{r}) + U_{11}|\Psi_1(\vec{r},t)|^2 + U_{12}|\Psi_2(\vec{r},t)|^2\right)\Psi_1(\vec{r},t) \quad (6.1)$$

$$i\hbar\frac{\partial\Psi_2(\vec{r},t)}{\partial t} = \left(-\frac{\hbar^2}{2m_2}\nabla^2 + V_2(\vec{r}) + U_{12}|\Psi_1(\vec{r},t)|^2 + U_{22}|\Psi_2(\vec{r},t)|^2\right)\Psi_2(\vec{r},t) \quad (6.2)$$

where the intra- and inter- species interactions U_{11}, U_{22} and U_{12} are determined by s-wave scattering lengths a_{11}, a_{22} and a_{12} through $U_{11} = 4\pi\hbar^2 a_{11}/m_1$, $U_{22} = 4\pi\hbar^2 a_{22}/m_2$ and $U_{12} = 2\pi\hbar^2 a_{12}/m_{12}$, where m_{12} is defined as $m_{12} = m_1 m_2/(m_1 +$

m_2). The normalization conditions are

$$\int d\vec{r}|\Psi_1(\vec{r},t)|^2 = N_1, \tag{6.3}$$

$$\int d\vec{r}|\Psi_2(\vec{r},t)|^2 = N_2, \tag{6.4}$$

where N_1 and N_1 are the numbers of atoms in states $|1\rangle$ and $|2\rangle$, respectively. The time-independent equations for the ground state of the double condensates can be obtained as follows

$$\left(-\frac{\hbar^2}{2m_1}\nabla^2 + V_1(\vec{r}) + U_{11}|\Psi_1(\vec{r})|^2 + U_{12}|\Psi_2(\vec{r})|^2\right)\Psi_1(\vec{r}) = \mu_1\Psi_1(\vec{r}), \tag{6.5}$$

$$\left(-\frac{\hbar^2}{2m_2}\nabla^2 + V_2(\vec{r}) + U_{12}|\Psi_1(\vec{r})|^2 + U_{22}|\Psi_2(\vec{r})|^2\right)\Psi_2(\vec{r}) = \mu_2\Psi_2(\vec{r}), \tag{6.6}$$

where μ_1 and μ_2 are the chemical potentials. The spatial positions of the two fluids are determined by the their respective confining magnetic potentials. The locations of the two minima of the confining potentials $V_1(\vec{r})$ and $V_2(\vec{r})$ can be adjusted externally to be either exactly coincident or slightly offset. The inter- and intra-species interactions are dominant factors in determining the the density distributions. When the numbers of particles of both species are large, we would intuitively expect that the Thomas-Fermi approximation used in the single component BEC system could be useful [26, 27]. However, we have found out that this is not the case here. The Thomas-Fermi approximation gives the wrong picture for the recent JILA experiments [28, 29]. As in Chapter 3, when Thomas-Fermi approximation can be used, we neglect the kinetic energies and obtain the following algebraic equations

$$\left(V_1(\vec{r}) + U_{11}|\Psi_1(\vec{r})|^2 + U_{12}|\Psi_2(\vec{r})|^2\right)\Psi_1(\vec{r}) = \mu_1\Psi_1(\vec{r}), \tag{6.7}$$

$$\left(V_2(\vec{r}) + U_{12}|\Psi_1(\vec{r})|^2 + U_{22}|\Psi_2(\vec{r})|^2\right)\Psi_2(\vec{r}) = \mu_2\Psi_2(\vec{r}). \tag{6.8}$$

To simplify the problem and to prove our observation, we will only consider the experiments done at JILA with the two internal states of ^{87}Rb, which implies $m_1 = m_2 = m_{12} = m_0$. For the Thomas-Fermi approximation to work easily, we consider the trapping potentials with no displacement, which in our case are the same external harmonic potential. We will denote the potential as $V_{ext}(\vec{r})$. The non-trivial solutions are the following

$$\begin{cases} |\Psi_1(\vec{r})|^2 = (\mu_1 - V_{ext}(\vec{r}))/U_{11}, \\ |\Psi_2(\vec{r})|^2 = 0; \end{cases} \tag{6.9}$$

or

$$\begin{cases} |\Psi_1(\vec{r})|^2 = 0, \\ |\Psi_2(\vec{r})|^2 = (\mu_2 - V_{ext}(\vec{r}))/U_{22}; \end{cases} \tag{6.10}$$

or

$$\begin{cases} |\Psi_1(\vec{r})|^2 = (\mu_1 U_{22} - \mu_2 U_{12} - V_{ext}(\vec{r})(U_{22} - U_{12}))/\Delta, \\ |\Psi_2(\vec{r})|^2 = (\mu_2 U_{11} - \mu_1 U_{12} - V_{ext}(\vec{r})(U_{11} - U_{12}))/\Delta, \end{cases} \tag{6.11}$$

where Δ is defined as

$$\Delta = U_{11}U_{22} - U_{12}^2. \tag{6.12}$$

For the case of JILA experiments, it is known that $a_{11} : a_{12} : a_{22} = 1.03 : 1 : 0.97$ with the average of the three $(a_{11} + a_{12} + a_{22})/3$ being 55(3)Å. It follows that $\Delta < 0$ and all the nonzero densities in Eqs. (6.9), (6.10), and (6.11) have the inverted paraboloid forms except for $|\Psi_2(\vec{r})|^2$ in Eq. (6.11), which has a paraboloid form. It is our observation that the only possible solutions must have one of the shapes shown in Fig. 6.1. The key point is that the solutions in Eqs. (6.9), (6.10), and (6.11) must appear as a pair piecewisely in the final expression for the densities and there are only finite number of possible combinations. The requirement that density must be positive everywhere and zero when $r \to 0$ puts further restriction on the choice of combinations. It is clear that in this case, the Thomas-Fermi approximation

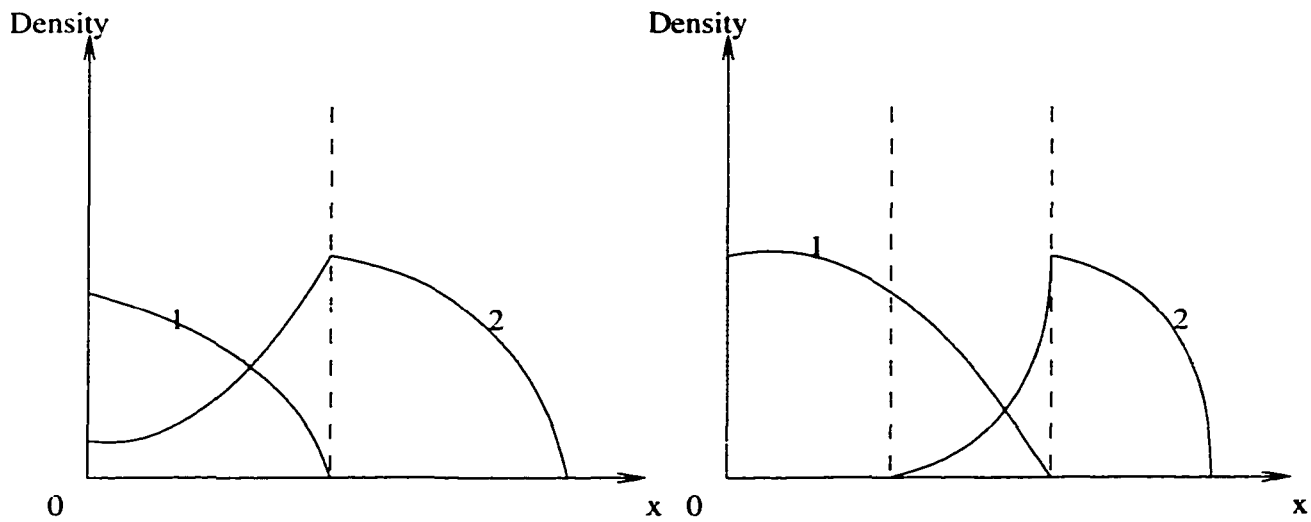

Figure 6.1: Schematic diagram of possible Thomas-Fermi ground states.

always puts $|1\rangle$ in the center and $|2\rangle$ at the periphery of the cloud, which is in direct contradiction with what is observed in the experiment and numerical calculation. Our numerical studies use the steepest descent method modified for the double condensates case. The modification is straightforward. One only needs to propagate the coupled time-dependent GP equations (6.1) and (6.2) in imaginary time as in section 3.4 while keeping the normalization conditions Eqs. (6.3) and (6.4) to hold for all the time. For an early numerical work on the ground state of double condensates, see Ref. [30]. The results are in agreement with the JILA experiment, which shows that $|1\rangle$ forms a shell around $|2\rangle$. In Fig. 6.2 and Fig. 6.3, we show the density of condensate in the x-z plane, due to symmetry, only the parts with $x > 0$ are shown here. As we can see clearly from Fig. 6.2 and Fig. 6.3, the atoms in state $|1\rangle$ with slightly stronger interaction occupy the outer shell, while

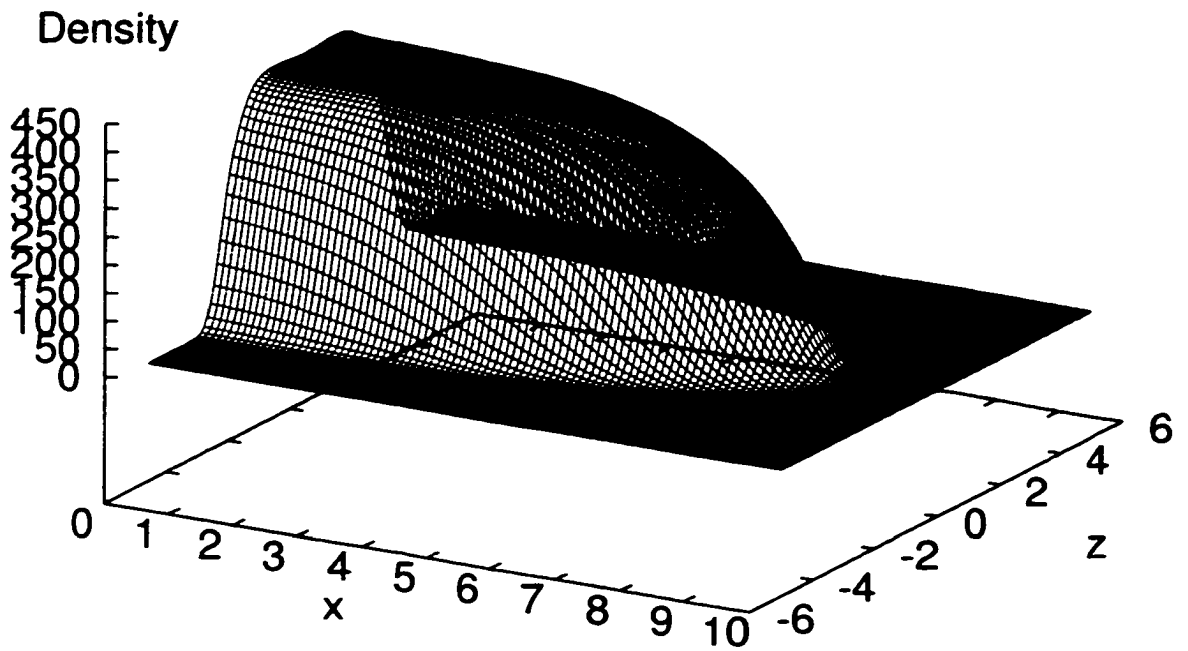

Figure 6.2: Density of 2.5×10^5 ^{87}Rb atoms in state $|1\rangle$. The lengths are in unit d_ρ. There is no displacement for the trapping potentials. The trap has $\omega_\rho = 2\pi \times 20.7$Hz and $\lambda = \sqrt{8}$.

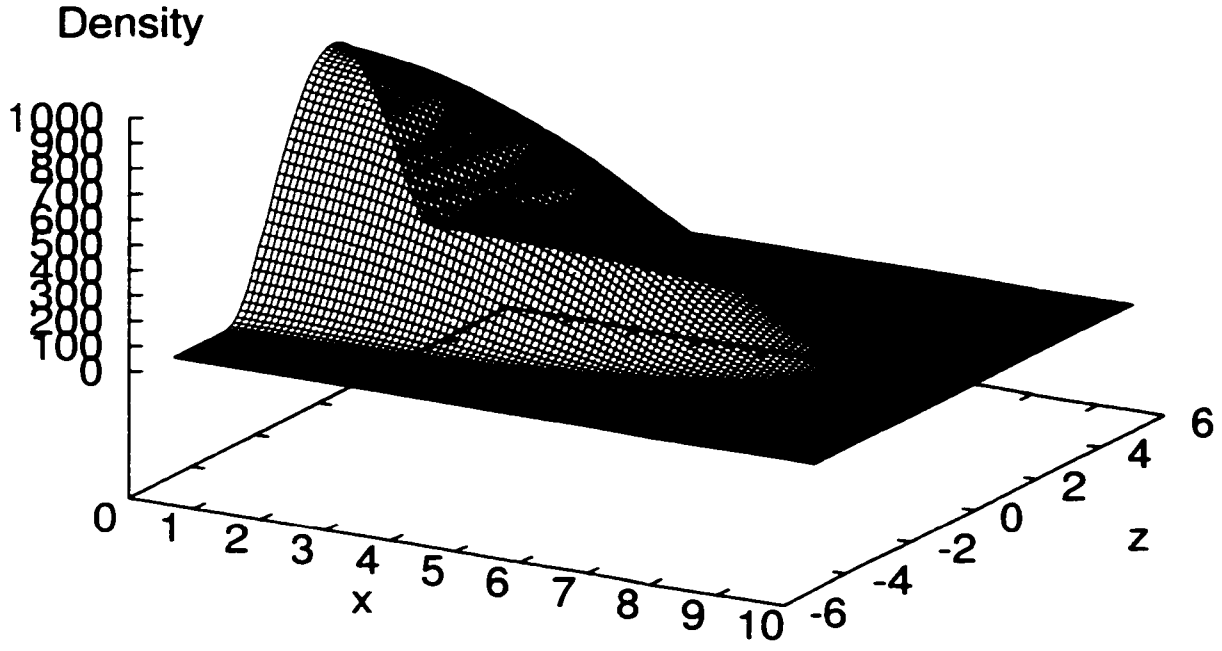

Figure 6.3: Density of 2.5×10^5 ^{87}Rb atoms in state $|2\rangle$. The lengths are in unit d_ρ. There is no displacement for the trapping potentials. The trap has $\omega_\rho = 2\pi \times 20.7$Hz and $\lambda = \sqrt{8}$.

the atoms in state $|2\rangle$ with slightly weaker interaction stay in the center. The reason for this discrepancy is not clear at the moment and will be the subject of further investigation. In Fig. 6.4 and Fig. 6.5, we show the density of the double condensates when the external potentials are displaced by 400 nm in the z direction. As expected, since there is a minor vertical offset in the spatial centers of $V_1(\vec{r})$ and $V_2(\vec{r})$, the components are separated in the z-direction, rather than in-and-out. The results we presented here are in agreement with the experiment performed at JILA. In Fig. 6.6, we show the typical double condensate images taken by JILA [28].

6.3 Dynamics of Component Separation

As previously mentioned, the double condensates system obtained at JILA is prepared from an initial pure single $|1\rangle$ by driving a two-photon transition. The process is shown schematicaly in Fig. 6.7 [28]. In the presence of such a coupling drive at frequency ω_{rf}, the dynamics of double condensates system is governed by the following equations [28]

$$i\hbar\frac{\partial\Psi_1(\vec{r},t)}{\partial t} = \left(-\frac{\hbar^2}{2m_1}\nabla^2 + V_1(\vec{r}) + \hbar\omega_1 + U_{11}|\Psi_1(\vec{r},t)|^2 + U_{12}|\Psi_2(\vec{r},t)|^2\right)\Psi_1(\vec{r},t) + \frac{\hbar\Omega}{2}e^{i\omega_{rf}t}\Psi_2(\vec{r},t), \tag{6.13}$$

$$i\hbar\frac{\partial\Psi_2(\vec{r},t)}{\partial t} = \left(-\frac{\hbar^2}{2m_2}\nabla^2 + V_2(\vec{r}) + \hbar\omega_2 + U_{12}|\Psi_1(\vec{r},t)|^2 + U_{22}|\Psi_2(\vec{r},t)|^2\right)\Psi_2(\vec{r},t) + \frac{\hbar\Omega}{2}e^{-i\omega_{rf}t}\Psi_1(\vec{r},t), \tag{6.14}$$

where ω_1 and ω_2 are the corresponding frequencies of the states $|1\rangle$ and $|2\rangle$ respectively and Ω is the amplitude of coupling. The driving frequency is detuned slightly from the transition frequency by δ, namely,

$$\omega_{rf} = \omega_2 - \omega_1 + \delta, \tag{6.15}$$

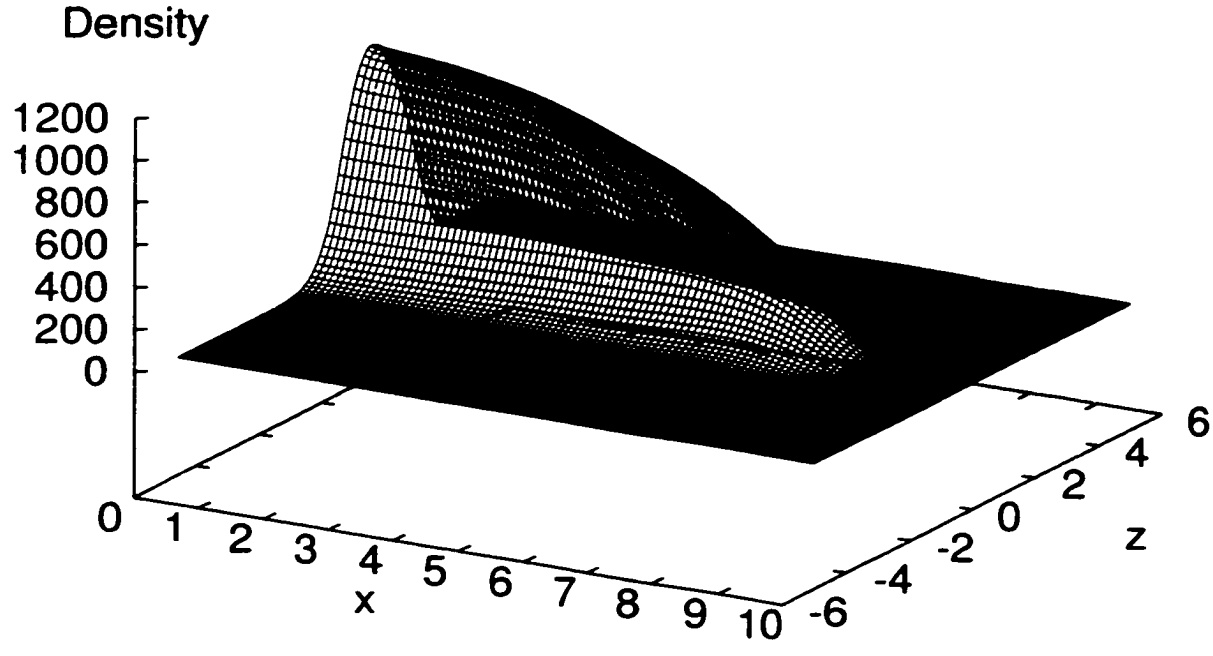

Figure 6.4: Density of 2.5×10^5 ^{87}Rb atoms in state $|1\rangle$. The lengths are in unit d_ρ. The center of the trap is at $z = 200$ nm. The trap has $\omega_\rho = 2\pi \times 20.7$Hz and $\lambda = \sqrt{8}$.

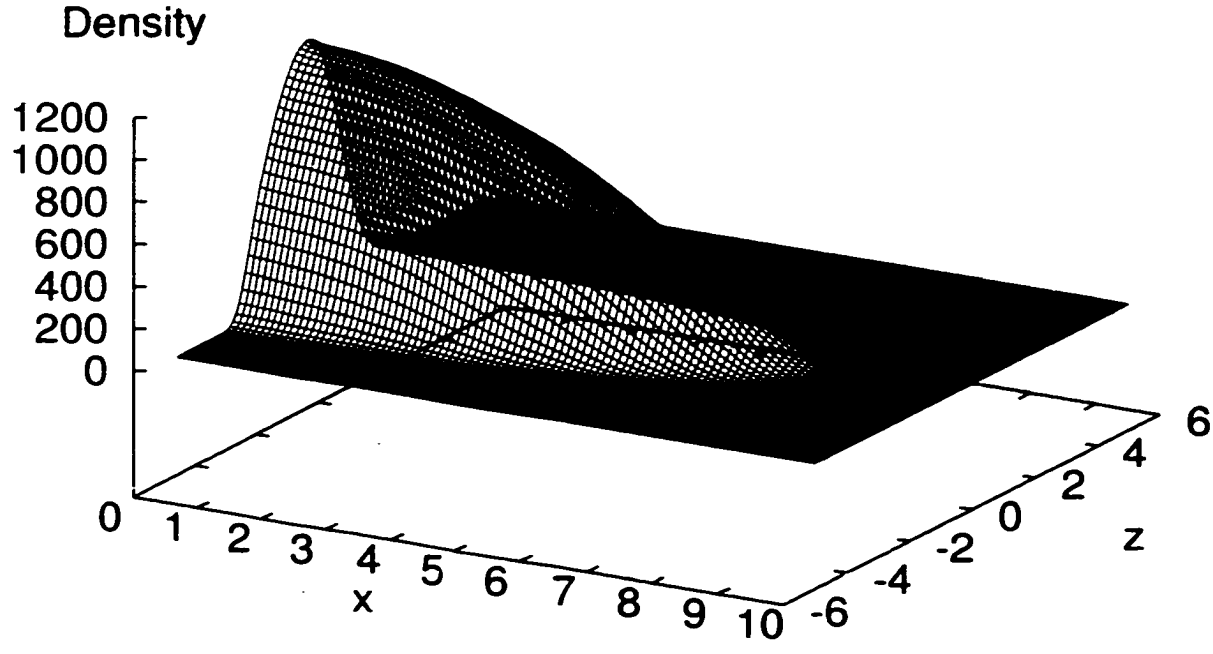

Figure 6.5: Density of 2.5×10^5 ^{87}Rb atoms in state $|2\rangle$. The lengths are in unit d_ρ. The center of the trap is at $z = -200$ nm. The trap has $\omega_\rho = 2\pi \times 20.7$Hz and $\lambda = \sqrt{8}$.

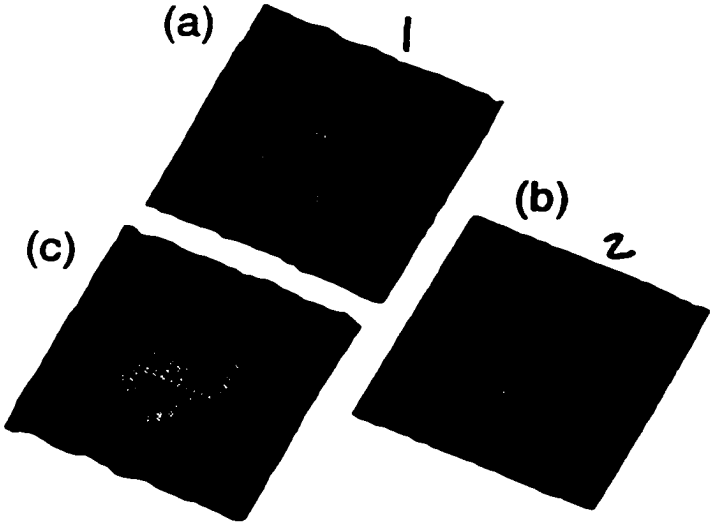

Figure 6.6: Figure taken from JILA experiment, see text. (a) The image of the $|1\rangle$ condensate exhibits a "crater", corresponding to a shell in which the $|2\rangle$ atoms (b) reside. For this trap, $\nu_z = 47$ Hz with zero relative sag. By changing the strength of the magnetic quadrupole field, a nonzero relative sag can be introduced, which shifts the location of the "crater" (c). (Each square in this post-expansion image is $136\mu m$ on a side.)

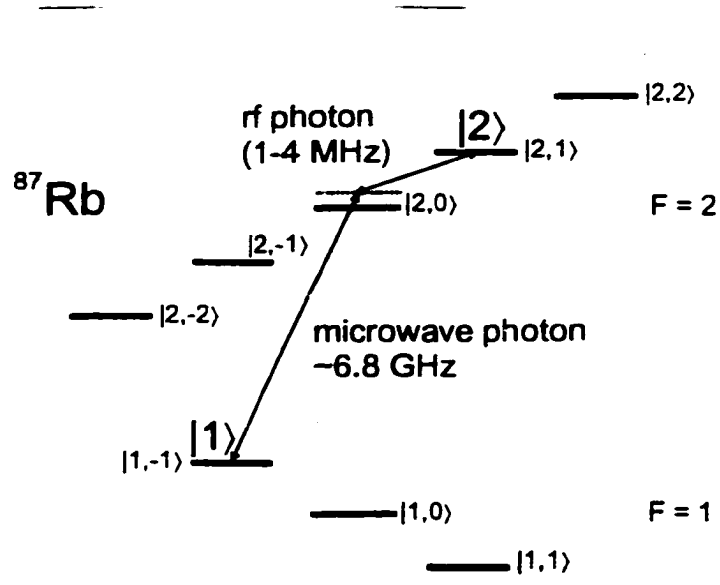

Figure 6.7: Figure taken from JILA experiment, see text. A schematic diagram of the ground state hyperfine levels ($F = 1, 2$) of ^{87}Rb, shown with a splitting due to an applied magnetic field. The two-photon transition is driven between the $|1, -1\rangle$ ($|1\rangle$) and $|2, 1\rangle$ ($|2\rangle$) states.

and $|\delta| \ll \omega_{rf}$. We will treat Eq. (6.13) and Eq. (6.14) in the rotating frame by introducing

$$\Phi_1(\vec{r},t) = e^{i(\omega_1 - \frac{\delta}{2})t}\Psi_1(\vec{r},t), \tag{6.16}$$

$$\Phi_2(\vec{r},t) = e^{i(\omega_2 + \frac{\delta}{2})t}\Psi_2(\vec{r},t). \tag{6.17}$$

And we have

$$i\hbar\frac{\partial\Phi_1(\vec{r},t)}{\partial t} = \left(-\frac{\hbar^2}{2m_1}\nabla^2 + V_1(\vec{r}) + \frac{\hbar\delta}{2} + U_{11}|\Phi_1(\vec{r},t)|^2 + U_{12}|\Phi_2(\vec{r},t)|^2\right)\Phi_1(\vec{r},t) + \frac{\hbar\Omega}{2}\Phi_2(\vec{r},t), \tag{6.18}$$

$$i\hbar\frac{\partial\Phi_2(\vec{r},t)}{\partial t} = \left(-\frac{\hbar^2}{2m_2}\nabla^2 + V_2(\vec{r}) + \frac{\hbar\delta}{2} + U_{12}|\Phi_1(\vec{r},t)|^2 + U_{22}|\Phi_2(\vec{r},t)|^2\right)\Phi_2(\vec{r},t) + \frac{\hbar\Omega}{2}\Phi_1(\vec{r},t), \tag{6.19}$$

In the JILA experiment, the trapping potentials are displaced such that the minimum of $V_2(\vec{r})$ is 0.4μm lower than that of $V_1(\vec{r})$, or approximately 3% of the total extent of the combined density distribution in the vertical direction. At first, approximately 5×10^5 ^{87}Rb atoms are formed condensate in state $|1\rangle$, it is possible to transfer quickly any desired fraction of the atoms to state $|2\rangle$ by selecting the amplitude and length of the two-photon pulse. A pulse with amplitude and duration such that $\Omega\tau = \pi/2$, which is known as the "$\pi/2$ pulse", is then applied to transfer half the population from state $|1\rangle$ to $|2\rangle$. The system is then left to evolve freely and eventually come to equilibrium after about 65 ms. We numerically propagate the coupled GP equations (6.18) and (6.19). The numerical results are shown in Fig. 6.8. Our numerical simulation of the experiment is in fair agreement with the experimental data. We show the experimental result from Ref. [28] in Fig. 6.9. The experiment shows somewhat larger damping than the numerical calculation. This

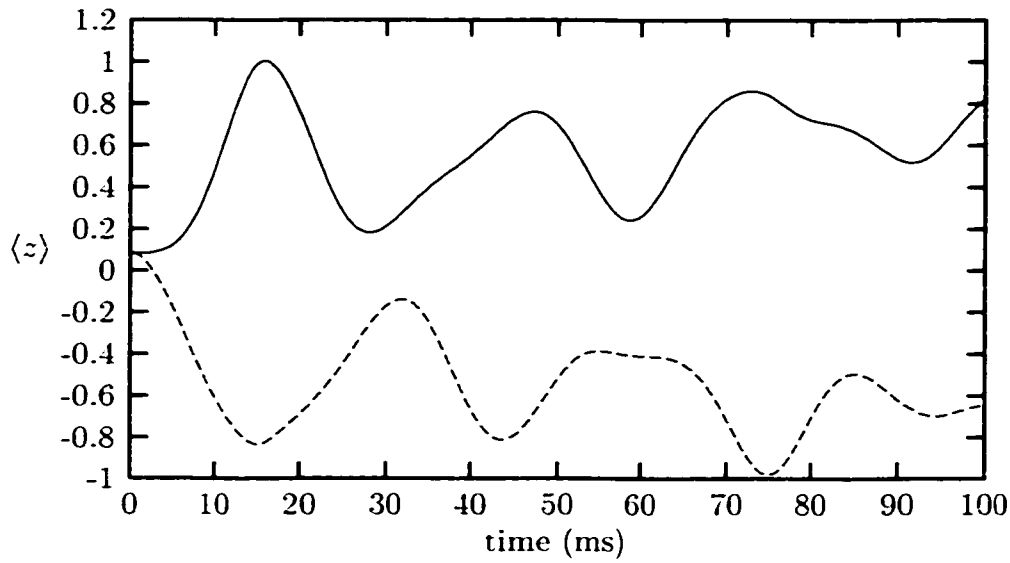

Figure 6.8: The center of masses in z direction for atoms in state $|1\rangle$ and $|2\rangle$. Solid line is for $|1\rangle$, while dashed line is for $|2\rangle$. The center of the external potentials are at $z = \pm 200$ nm for $|1\rangle$ and $|2\rangle$, respectively. The unit of length is d_ρ.

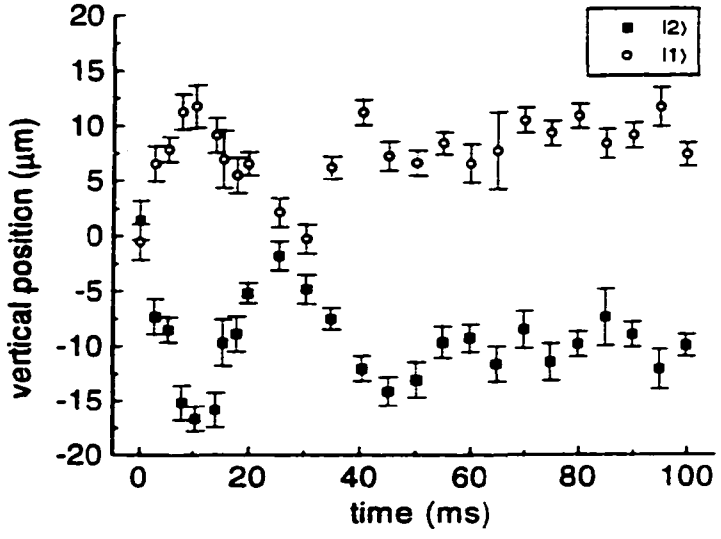

Figure 6.9: Figure taken from JILA experiment, see text. The relative motion of the center-of-mass of the two condensates. The relative sag is 400 nm and the trap frequency is $\nu_z = 59$ Hz.

may be due to the existence of the thermal component in the system.

Chapter 7

Conclusions and Further Work

7.1 Conclusions

In this part, we have provided an introductory description of the properties of Bose-Einstein condensation in trapped dilute gases. The main conclusion is that, despite of the dilute nature of the Bose gases, two-body interactions still have an important impact on most of the physical quantities of interest, such as those properties of the ground state and the low excited states considered in Chapter 3 and Chapter 4. Interaction can be included into the theory of BEC within the mean field approximation framework depending on a single parameter, the s-wave scattering length a, which can be measured with rather high accuracy. As a result, there is no adjustable parameter in the theory and the fact that the theoretical predictions are in very good agreement with the experiments shows the validity of the theory. We have found out that at zero-temperature, the Gross-Pitaevskii equation derived from the mean field theory gives an accurate description of the ground state of the condensate. For large number of particles, the Thomas-Fermi approximation can be used to give good results for the condensate density profile and chemical potential. For the low excited states, the Bogoliubov theory provides excellent agreement with

the experiment for the excitation frequencies. The numerical solutions to the ground state based on the mean field theory can be obtained systematically using either the steepest descent method or the basis expansion method described in Chapter 3. At nonzero temperature, the extension of Bogoliubov theory with Popov approximation gives a set of equations, which must be solved self-consistently to get the ground state and the excited states. The semiclassical approximation can be used for higher temperature to obtain the excitation energy and the condensate fraction. We further extent the mean field theory to treat the double condensate systems. The ground state wave functions are obtained using steepest descent method. We also observe that for the current JILA experiment, the Thomas-Fermi approximation does not give correct picture for large number of atoms as expected intuitively. The dynamics of component separation is simulated using the coupled driven GP equations. The result is in fair agreement with the experiment.

7.2 Further Work

We have developed systematically a set of numerical methods to study various properties of the BEC systems based on the mean field theory. Using these numerical methods, we can study many other topics related to the condensate. We will conclude this part of the thesis by listing several interesting subjects for further work:

- For ^{7}Li atoms, the s-wave scattering length is negative, which corresponds to an attractive interaction between particles. It is well known that homogeneous BEC system with such attractive interaction is unstable [31]. However, if the condensate is confined by a potential and the number of particles is not too large, then it is possible for the zero-point energy to exceed the attractive

interaction energy and to stabilize the condensate against collapse. It is reported that the maximum number of particle this system can reach is about 1500 under the current experimental conditions [4, 32]. It will be interesting to see if the steepest descent method used in Chapter 3 can be used in the systems with attractive forces.

- At non-zero temperature, the excitations can be determined by the Bogoliubov theory with Popov approximation. In Chapter 5, semiclassical approximation is used to solve self-consistently the equations for the ground state wave function and the excited states at given temperature T. However, the expansion method similar to what is used in Chapter 4 can also be used to obtain the excitations at finite temperature [33]. It is worth studying if the semiclassical approximation agrees with the more accurate expansion method.

- For the large amplitude oscillation simulated in Chapter 4, it is not directly comparable to the experiment performed at JILA [34] because the experiment was performed at finite temperature, while the simulation is done at zero temperature. Thus it makes sense to extend the numerical study there to include the temperature effect. Some work has already been reported on the subject using some kind of phenomenological treatment [35]. For theory of damping of low-energy excitations at finite temperature, see Ref. [36, 37, 38].

- As mentioned in Chapter 6, the reason why the Thomas-Fermi approximation for the double condensates does not agree with either the numerical solution or the experiment is not clear. It is worthwhile to continue the investigation of this question. Also there has been some work reported about the symmetry

breaking in the ground state of the binary mixtures of BEC [39, 40, 41]. The steepest descent method used in Chapter 6 will be a useful tool for this subject.

- Vortices in a Bose-Einstein condensate is another very interesting topic. JILA group has reported the creation of vortices in two-component BEC system [42] through a coherent process involving the spatial and temporal control of interconversion between the two components. Using an interference technique, the vortex state is confirmed to possess angular momentum. It will be very interesting to investigate the properties of the vortex state using the numerical method given in section 4.4. Some numerical work has already appeared in the literature [43, 44].

Part II

Scattering of Hot Excitons in Quantum Wells and Ground State Properties of Quantum Dots

Chapter 8

Scattering of Hot Excitons in Quantum Wells

8.1 Introduction

In this chapter we investigate the hot exciton scattering rates in semiconductor narrow quantum wells (QWs). An exciton with kinetic energy higher than the thermal temperature of the medium is called a hot exciton. This concept has been introduced in the past when multiphonon LO-lines have been observed in resonant Raman scattering in bulk semiconductor materials (see [45] and references therein). For polar semiconductors, when the exciton energy is greater than a longitudinal optical phonon, the scattering rate is governed by the exciton-LO phonon interaction and the Fröhlich like mechanism is the stronger one playing the main role in the exciton relaxation time. In the past and for the bulk semiconductor case, transition probabilities of hot excitons interacting with longitudinal and acoustic phonons have been carried out in Refs. [46, 47, 48]. The dependence on exciton kinetic energy, effective electron and hole masses, and the excitonic quantum numbers were obtained, showing the conditions that favor the hot excitons contribution to the multiphonon Raman process in semiconductors. The importance of hot exciton

relaxation via optical phonon emission in QWs has been stressed by photoluminescence experiments [49] and by time-resolved Raman scattering measurements [50]. Also, the relative role of confined phonons and interface modes in time resolved resonant Raman spectroscopy experiments is pointed out in Ref. [51]. Today, there are several theoretical studies of carrier relaxation times in QWs considering the main mechanism due to electron-LO-phonon interaction (e.g. Ref. [52] and references therein). Nevertheless, a direct calculation of the hot exciton scattering rate due to the confined optical phonons in a QW is lacking in the literature. In this chapter we will focus on the excitonic scattering rate calculation and on its contribution to the multiphonon resonant Raman process (MPR) in narrow QWs. Recently, Mowbray et al [53] reported a multiphonon process in GaAs/AlAs superlattices. Raman spectra for the second and third order processes from GaAs phonons show structures involving the combination of confined and interface LO phonons. The relative intensities of the second and third order processes due to the combination of L_2 confined phonon are weaker than that obtained with L_2 and interface phonons for samples of 6-GaAs monolayer. The enumeration of phonon symmetries in the QW follows Ref. [54]. For the case of 10-GaAs monolayer samples, the combined intensities of L_2 and L_4 phonons are comparable to the intensities due to $2L_2$ or $3L_2$ ones. These results show that the relative intensities of a MPR scattering process are very sensitive to the quantum well width. The connection of the MPR process with excitonic transitions followed when the excitonic cascade model is invoked to explain the main features of the scattered light [45]. According to this model, the scattering cross section with an emission of one emitted phonon is proportional to the exciton scattering rate $W(E)$ with kinetic energy E. Thus, an explicit calcula-

tion of $W(E)$ as a function of the QW width and phonon mode contribution will bring further understanding of MPR process in QWs as we will discuss bellow.

8.2 Model and Fundamental Expressions

To describe the scattering rate process we assume a Wannier-Mott exciton model in a quantum well with non-degenerate electron and hole isotropic bands. In the framework of the envelope function approximation the eigenvalues and eigenfunctions of the quantum confined excitons are described by the Hamiltonian

$$\hat{H} = \frac{\hat{p}_e^2}{2m_e} + \frac{\hat{p}_h^2}{2m_h} - \frac{e^2}{\epsilon_0|\vec{r}_e - \vec{r}_h|} + V_e(z_e) + V_h(z_h), \tag{8.1}$$

where $m_e(m_h)$, $\vec{r}_e = (\vec{\rho}_e, z_e)$ $(\vec{r}_h = (\vec{\rho}_h, z_h))$, and $V_e(z_e)$ $(V_h(z_h))$ are the effective mass, the coordinates, and band off-set for the electron (hole), respectively. ϵ_0 is the static dielectric constant. For narrow quantum wells where the QW width d is smaller than the bulk exciton Bohr radius a_B (strong quantization limit), the Hamiltonian (8.1) can be rewritten as

$$\hat{H} = \hat{H}_0 + \hat{H}_p, \tag{8.2}$$

with

$$\hat{H}_0 = \frac{\hat{p}_e^2}{2m_e} + \frac{\hat{p}_h^2}{2m_h} - \frac{e^2}{\epsilon\rho} + V_e(z_e) + V_h(z_h), \tag{8.3}$$

and

$$\hat{H}_p = \frac{e^2}{\epsilon|\vec{\rho}_e - \vec{\rho}_h|} - \frac{e^2}{\epsilon|\vec{r}_e - \vec{r}_h|}, \tag{8.4}$$

where $\hat{H}_p$ can be considered as a perturbation term to the Hamiltonian (8.4). In the strong quantization limit where $a_B \gg d$ the exciton motion is reduced to solving the two-dimensional Wannier-Mott equation. The exciton wave function $\Psi_{exc}(\vec{r}_e, \vec{r}_h)$ of

the Hamiltonian H_0 can be taken in separable form given by products of the two-dimensional exciton wave function $\Psi(\vec{R},\vec{\rho})$ and the electron and hole subband wave functions $\phi_i(z_i)(i=e,h)$

$$\Psi_{exc}(\vec{r}_e,\vec{r}_h)=\Psi(\vec{R},\vec{\rho})\phi_e(z_e)\phi_h(z_h). \tag{8.5}$$

In Eq.(8.5), $\vec{R}=(m_e\vec{\rho}_e+m_h\vec{\rho}_h)/M$ $(M=m_e+m_h)$ is the electron-hole pair center-of-mass coordinate on the x-y plane, $\vec{\rho}=\vec{\rho}_e-\vec{\rho}_h$ is the in-plane relative coordinate of the electron and the hole and the motion along the z-axis is described by the wave functions

$$\phi_n(z)=B_n\begin{cases}e^{k_Bz}, & z\le -d/2,\\ e^{-k_Bd/2}\cos(k_Az+n\pi/2)/\cos(k_Ad/2+n\pi/2), & |z|\le d/2,\\ (-1)^ne^{-k_Bz}, & z\ge d/2,\end{cases} \tag{8.6}$$

with

$$B_n=e^{k_Bd/2}\left[\frac{1}{k_B}+\frac{1}{k_A}\frac{m_A}{m_B}\frac{k_A}{k_B}+\frac{d}{2}\left(\frac{m_A}{m_B}\frac{k_A}{k_B}\right)^2+\frac{d}{2}\right]^{-\frac{1}{2}}, \tag{8.7}$$

where $k_A=\sqrt{2m_AE_n/\hbar^2}$, $k_B=\sqrt{2m_B(V_0-E_n)/\hbar^2}$, V_0 is the band offset, and $m_A(m_B)$ is the carrier effective mass in the well (barrier). The eigenenergies E_n for even and odd states in the QW along z-direction are given by the bound state conditions

$$\frac{k_B}{m_B}=\frac{k_A}{m_A}\begin{cases}\tan(k_Ad/2), & n=1,3,\ldots,\\ -\cot(k_Ad/2), & n=2,4,\ldots.\end{cases} \tag{8.8}$$

The two-dimensional exciton wave function in polar coordinates can be separated into a center of mass motion with wave vector $\vec{K}$, a radial part and an angular part given by

$$\Psi(\vec{R},\vec{\rho})=\frac{1}{L}e^{i\vec{K}\cdot\vec{R}}R_{N,m}(\rho)\frac{1}{\sqrt{2\pi}}e^{im\phi}, \qquad m=0,\pm1,\pm2,\ldots. \tag{8.9}$$

For bound exciton states (bound exciton energy $\varepsilon_N < 0$), the corresponding normalized eigenfunction is obtained as follows

$$R_{N,m}(\rho) = N_{N,m} e^{-\rho/[a_B(N+1/2)]} \left[\frac{\rho}{a_B(N+1/2)}\right]^{|m|} \times F\left[-N+|m|, 2|m|+1, \frac{\rho}{a_B(N+1/2)}\right] \quad |m| \leq N,\ N = 0, 1, \ldots \quad (8.10)$$

where

$$N_{N,m} = \sqrt{\frac{(N+|m|)!}{[(2m)!]^2 a_B^2 (N+1/2)^3 (N-|m|)\pi}}, \quad (8.11)$$

and $F(\alpha, \beta; z)$ is the confluent hypergeometric function. The bound exciton energy ε_N are

$$\varepsilon_N = -\frac{R_y}{(N+1/2)^2}. \quad (8.12)$$

The total energy of Hamiltonian (8.1) is found to be

$$E = E_g + E_{n_e} + E_{n_h} + \varepsilon_N + \frac{\hbar^2 K^2}{2M}, \quad (8.13)$$

with E_g being the gap energy, $R_y = \mu e^2/2\hbar^2\epsilon^2$ the effective Rydberg constant and μ the reduced mass in the x-y plane.

To describe the exciton-phonon interaction we follow a unified treatment [54] that takes into account the full matching boundary conditions: mechanical and electrodynamic. This phenomenological treatment involves the coupling between the longitudinal (L), and transversal (T) polarization modes as a consequence of the coupled differential equations for the phonon displacement field $\vec{u}$ and electrostatic potential ϕ. The model yields confined quasi-L and confined quasi-T modes, while some of these modes exhibit interface character.[55] The interaction Hamiltonian is [55]

$$H_{E-P} = \sum_{n_p,\vec{q}} \frac{C_F}{\sqrt{V}} \left[\phi_{n_p,\vec{q}}(z_e) e^{i\vec{q}\cdot\vec{\rho}_e} - \phi_{n_p,\vec{q}}(z_h) e^{i\vec{q}\cdot\vec{\rho}_h}\right] \hat{b}_{n_p,\vec{q}} + H.C., \quad (8.14)$$

where $\hat{b}_{n_p,\vec{q}}$ is the phonon creation operator with wave vector $\vec{q}$ and frequency $\omega_{n_p,q}$. V is a normalization volume, and C_F is the Fröhlich coupling constant given by

$$C_F = e\sqrt{2\pi\hbar\omega_L(\epsilon_\infty^{-1} - \epsilon_0^{-1})}, \tag{8.15}$$

where ω_L is the LO phonon frequency, ϵ_∞ is the high frequency dielectric constant and ϵ_0 is the static dielectric constant. The Fröhlich-type exciton-phonon interaction (8.14) has been expressed as a product of factors for motion perpendicular and parallel to the QW axis. The function $\phi_{n_p,\vec{q}}$ is proportional to the electrostatic scalar potential obtained as solution of the eigenvalue problem and shows a definite parity. We need to remark that the potential given in Refs. [55] has several misprints. The correct expressions are written below.

(A) Odd potential states

$$\phi_{n_p,\vec{q}}(z) = \sqrt{\frac{d}{||u||^2}} \begin{cases} \sin(2\eta_L z/d) - S_L^+ e^{-\eta_q} \sinh(2\eta_q z/d)/\eta_q, & |z| \le d/2, \\ S_0 e^{-2\eta_q |z|/d} z/|z|, & |z| \ge d/2, \end{cases} \tag{8.16}$$

with the following dispersion relation

$$\left(\frac{\beta_L}{\beta_T}\right)^2 \left[\eta_L^2 + \left(\frac{dq}{2}\right)^2\right] (\eta_L \cos\eta_L + \eta_q \sin\eta_L)(\eta_q \cos\eta_T \sinh\eta_q + \eta_T \sin\eta_T \cosh\eta_q)$$

$$= \left[\eta_T^2 + \left(\frac{dq}{2}\right)^2\right] (\eta_q \cos\eta_T - \eta_T \sin\eta_T)(\eta_L \cos\eta_L \sinh\eta_q - \eta_q \sin\eta_L \cosh\eta_q), \tag{8.17}$$

where β_L and β_T are two parameters describing the quadratic dispersion of the LO and TO phonon in the bulk, respectively.

(B) Even potential state

$$\phi_{n_p,\vec{q}}(z) = \sqrt{\frac{d}{||u||^2}} \begin{cases} \cos(2\eta_L z/d) - C_L^+ e^{-\eta_q} \cosh(2\eta_q z/d)/\eta_q, & |z| \le d/2, \\ C_0 e^{-2\eta_q |z|/d}, & |z| \ge d/2, \end{cases} \tag{8.18}$$

with the following dispersion relation

$$\left(\frac{\beta_L}{\beta_T}\right)^2 \left[\eta_L^2 + \left(\frac{dq}{2}\right)^2\right] (\eta_q \cos\eta_L - \eta_L \sin\eta_L)(\eta_T \cos\eta_T \sinh\eta_q - \eta_q \sin\eta_T \cosh\eta_q)$$

$$= \left[\eta_T^2 + \left(\frac{dq}{2}\right)^2\right](\eta_T \cos\eta_T + \eta_q \sin\eta_T)(\eta_L \sin\eta_L \cosh\eta_q + \eta_q \cos\eta_L \sinh\eta_q). \quad (8.19)$$

In Eq.(8.16) and Eq.(8.18), $||u||^2$ represents the norm of the vibrational amplitude. The definition of the terms S_L^+, C_L^+, $||u||^2$ and other parameters can be found at the end of this chapter.

The sinusoidal and cosinusoidal functions appearing in Eq. (8.16) and Eq. (8.18), respectively are the contributions of the confinement phonons to the electrostatic potential, while the hyperbolic and exponential functions come from the interface phonons and are due to the dielectric mismatch between the interfaces. It is important to realize that we do not have purely interface modes, and also for both cases, the coupled modes satisfy $\nabla \cdot \vec{u} \neq 0$ and $\nabla \times \vec{u} \neq 0$. The modes may be predominantly L, or predominantly T, or present certain character of "interface" modes, depending on wave-vector $\vec{q}$ which is contained in Eq.(8.17) and Eq.(8.19). The phonon dispersion for a QW structure of GaAs/AlAs with 2.0 nm and 1.7 nm well width are shown in Fig. 8.1. The branches are labeled as L_N and T_N (N=1,2,...) according to their longitudinal and transverse character at $\vec{q} = 0$. The modes which show a strong dispersion as a function of the in-plane wave vector $\vec{q}$ are those with the strongest electric field component and also the strongest interface character. For the 2.0 nm QW the two interface branches are L_1 and L_4 modes, while in the case of 1.7 nm QW, these correspond to L_1 and T_1 modes. The upper mode is purely antisymmetric (L_1) while the lower interface mode (L_4 and T_1 in Figs. 8.1(a) and 8.1(b), respectively) is symmetric. The antisymmetric part of the potential (L_1, L_3 modes) couples to the exciton via inter-subband transitions with exciton wave functions having different symmetry with respect to the center of the well. The symmetric part of the function $\phi_{n_p,\vec{q}}$ (L_2, L_4 modes) couples to excitons

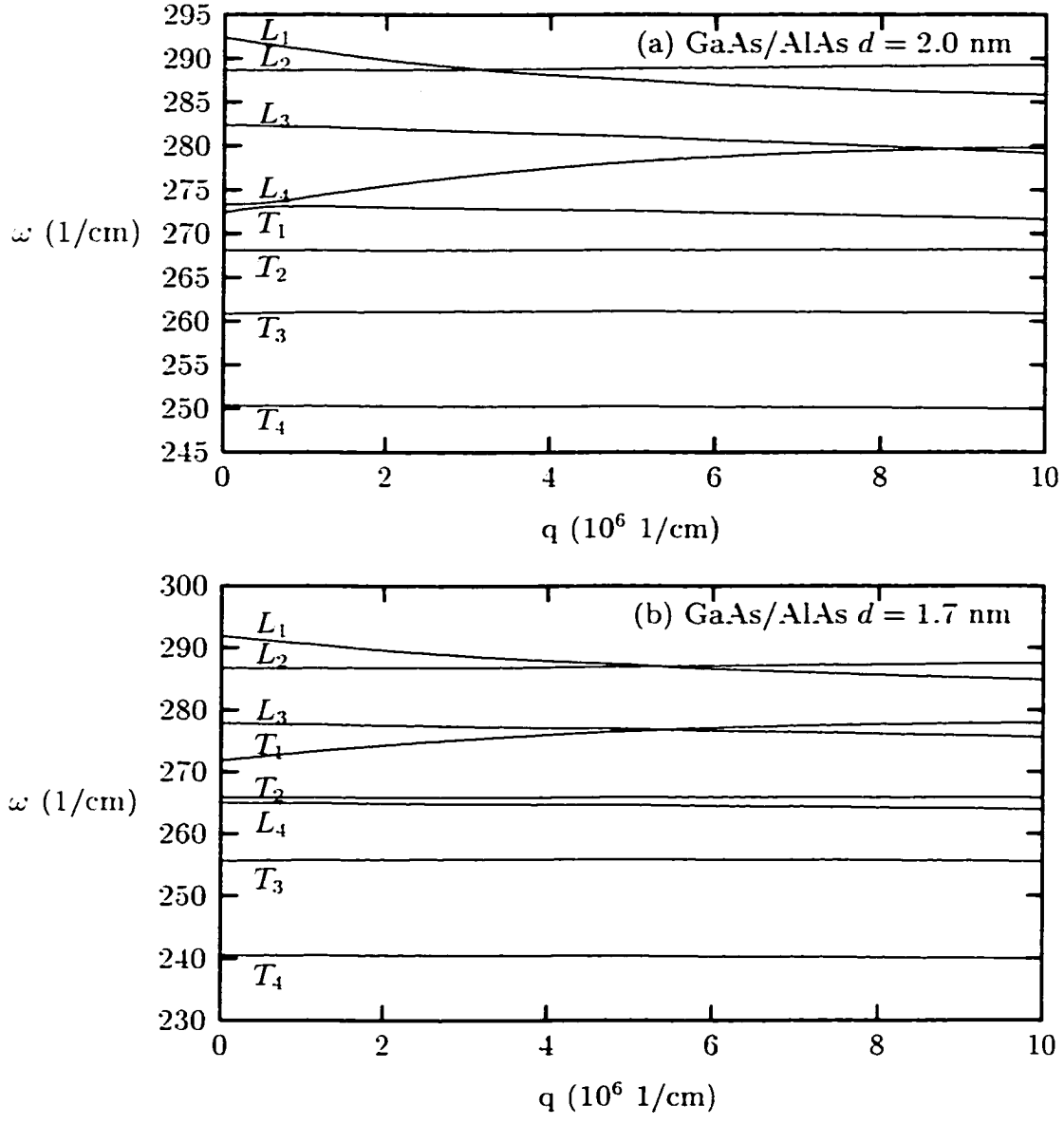

Figure 8.1: Dispersion of the GaAs optical phonons of the (a) 2.0 nm and (b) 1.7 nm GaAs/AlAs quantum wells. The phonons are labeled as longitudinal (L) and transverse (T) according to its character at $\vec{q} = 0$. Symmetric phonon potentials correspond to L_2 and L_4, and antisymmetric phonon potentials correspond to L_1 and L_3. The interface modes are those showing strong dispersion as a function of q. The anticrossing of L_4 and T_1 modes near $q = 0.5 \times 10^6$ (1/cm) is clearly seen in (a). L_4 and T_1 modes present the same parity respect to center of the QW.

via intra-subband transitions since the exciton wave function have the same symmetry respect to z-axis. The exciton inter-subband transition is also possible through the symmetric phonon potential part, if the initial and final excitonic states have the same parity with respect to the center of the QW.

8.3 Scattering Probability

The probability per unit time of the excitonic transition from state $|\vec{K}, N, m; n_e, n_h\rangle$ to state $|\vec{K}', N', m'; n_e', n_h'\rangle$ state due to the interaction with optic phonon is given by

$$\begin{aligned} & W^{(n_p)}_{N,m;n_e,n_h\to N',m';n_e',n_h'}\left(\vec{K},\vec{K}'\right) \\ &= \frac{2\pi}{\hbar}\sum_{\vec{q}} |\langle \vec{K}, N, m; n_e, n_h|H_{E-P}|n_h', n_e'; m', N', \vec{K}'\rangle|^2 \\ &\times\delta\left(\frac{\hbar^2K'^2}{2M} - \frac{\hbar^2K^2}{2M} + \hbar\omega_{n_p,q} + E_{n_e'} - E_{n_e} + E_{n_h'} - E_{n_h} + \varepsilon_{N'} - \varepsilon_N\right). \end{aligned} \quad (8.20)$$

We consider the case of low temperature where $k_BT \ll \hbar\omega_{n_p,q}$ (k_B is the Boltzmann constant) and the phonon emission Stokes process is the main process. The form of wave function Eq. (8.5) and the exciton-phonon Hamiltonian (8.14) permit us to write the matrix element in Eq. (8.20) as

$$\begin{aligned} & \langle \vec{K}, N, m; n_e, n_h|\hat{H}_{E-P}|n_h', n_e'; m', N', \vec{K}'\rangle = \frac{C_F}{\sqrt{V}}\delta_{\vec{K}',\vec{K}-\vec{q}} \\ &\times\left[I^{N',m'}_{N,m}(Q_h)\langle n_e|\phi_{n_p,\vec{q}}|n_e'\rangle\delta_{n_h,n_h'} - I^{N',m'}_{N,m}(Q_e)^*\langle n_h|\phi_{n_p,\vec{q}}|n_h'\rangle\delta_{n_e,n_e'}\right], \end{aligned} \quad (8.21)$$

where $Q_{h(e)} = m_{h(e)}a_Bq/M$. The first (second) term in the r.h.s. of Eq. (8.21) is related to the electron (hole) contribution to the scattering rate after the phonon emission. The corresponding transitions in the plane perpendicular to or along the QW growth direction are given by the integrals $I^{N',m'}_{N,m}$ and $\langle n|\phi|n'\rangle$. Substituting Eq.

(8.21) into Eq. (8.20) and carrying out the sum over $\vec{K}$ one can find the scattering rate as a function of the absolute value of the exciton wave vector $\vec{K}'$

$$W^{(n_p)}_{N,m;n_e,n_h\to N',m';n'_e,n'_h} = \frac{C_F^2}{2\pi\hbar d}\int_0^\infty dqq\int_0^{2\pi} d\theta_1\delta(f(q,\theta_1))$$
$$\times|I^{N',m'}_{N,m}(Q_h)\langle n_e|\phi_{n_p,\vec{q}}|n'_e\rangle\delta_{n_h,n'_h} - I^{N',m'}_{N,m}(Q_e)^*\langle n_h|\phi_{n_p,\vec{q}}|n'_h\rangle\delta_{n_e,n'_e}|^2, \quad (8.22)$$

where

$$f(q,\theta_1) = \frac{\hbar^2q^2}{2M} - \frac{\hbar^2Kq}{M}\cos\theta_1 + \hbar\omega_{n_p,q} + E_{n'_e} - E_{n_e} + E_{n'_h} - E_{n_h} + \varepsilon_{N'} - \varepsilon_N, \quad (8.23)$$

and θ_1 is the angle between $\vec{K}$ and $\vec{q}$. The energy and momentum conservation laws restrict the absolute value of the phonon wave vector q within the range of q_{min} and q_{max}, which are solutions of

$$f_\pm(E_K) \equiv q_0^2 \pm 2\sqrt{\frac{M}{\mu}}\sqrt{\frac{E_K}{R_y}}q_0 + \frac{M}{\mu R_y}\left(\hbar\omega_{n_p,q} + E_{n'_e} - E_{n_e} + E_{n'_h} - E_{n_h} + \varepsilon_{N'} - \varepsilon_N\right) = 0, \quad (8.24)$$

with the condition $q_{min} \geq 0$ and $E_K = \hbar^2K^2/2M$ is the exciton kinetic energy. After the integration with respect to θ_1 and summation over m and m' in Eq.(8.22), we obtain

$$W^{(n_p)}_{N;n_e,n_h\to N';n'_e,n'_h}(E_K) = 2\omega_L\frac{M}{a_B\mu}\left(\frac{\epsilon_0}{\epsilon_\infty} - 1\right)\int_{q_{min}}^{q_{max}}\frac{dq_0q_0}{\sqrt{f_+(q_0)f_-(q_0)}}$$
$$\times\sum_{m,m'}|e^{i(m'-m)\theta_1}I^{N',m'}_{N,m}(Q_h)\langle n_e|\phi_{n_p,\vec{q}}|n'_e\rangle\delta_{n_h,n'_h}$$
$$- e^{-i(m'-m)\theta_1}I^{N',m'}_{N,m}(Q_e)^*\langle n_h|\phi_{n_p,\vec{q}}|n'_h\rangle\delta_{n_e,n'_e}|^2, \quad (8.25)$$

where θ_1 is given by

$$\tan\theta_1(q_0) = 2\frac{\sqrt{f_+(q_0)f_-(q_0)}}{f_+(q_0) + f_-(q_0)}. \quad (8.26)$$

From the energy and quasi-momentum conservation laws it follows that the scattering probability is different from zero if the exciton kinetic energy $E_K > (\hbar\omega_{n_p,\vec{q}} +$

$E_{n'_e} - E_{n_e} + E_{n'_h} - E_{n_h} + \varepsilon_{N'} - \varepsilon_N$). In Fig. 8.2, we illustrate the content of Eq. (8.25), showing the types of one phonon Stokes scattering processes included in the scattering rate. Each exciton band is characterized by single electron and hole quantum numbers (n_e, n_h) and the total quantum number N: two excitonic bands are shown including dispersion due to center-of-mass motion as in Eq. (8.13). For an exciton excited to the initial state labeled A in Fig. 8.2, and in the approximation used in this paper, only two processes will occur: (a) intra-subband scattering, with phonon potential state of even parity ($n_p = 2, 4$) and $n_e = n'_e, n_h = n'_h$; (b) inter-intra-subband scattering with $n_e = n'_e$ but $n_h \neq n'_h$ and vice versa. Here, if $|n_h - n'_h|$ is even the phonon potential is an even function, while for $|n_h - n'_h|$ equal to an odd number, the phonon potential states need to be odd giving a zero electron contribution to the scattering probability. This is illustrated in Fig. 8.2, where single phonon inter- intra-subband scattering are shown by arrows $A \longrightarrow B$, $A \longrightarrow C$ defining the corresponding q_{min} and q_{max} for theses processes. The exciton intra-subband transitions ($A \longrightarrow B'$, $A \longrightarrow C'$) in Fig. 8.2 are coupled to the symmetric part of the phonon potential, while the exciton inter-subbbond exciton energy and scattering (with mixed character or not) couples to the symmetric or antisymmetric part of the Fröhlich Hamiltonian interaction. Hence, the total inverse exciton lifetime characterized by the quantum numbers $N; n_e, n_h; E_K$ and due to the interaction with an optical phonon n_p can be written as

$$W^{-(n_p)}_{N;n_e,n_h}(E_K) = W^{(n_p)}_{N;n_e,n_h \to N;n_e,n_h}(E_K) + \sum_{N' \neq N} W^{(n_p)}_{N;n_e,n_h \to N';n_e,n_h}(E_K) + \sum_{n_e \neq n'_e, or, n_h \neq n'_h, N'} W^{(n_p)}_{N;n_e,n_h \to N';n'_e,n'_h}(E_K) \tag{8.27}$$

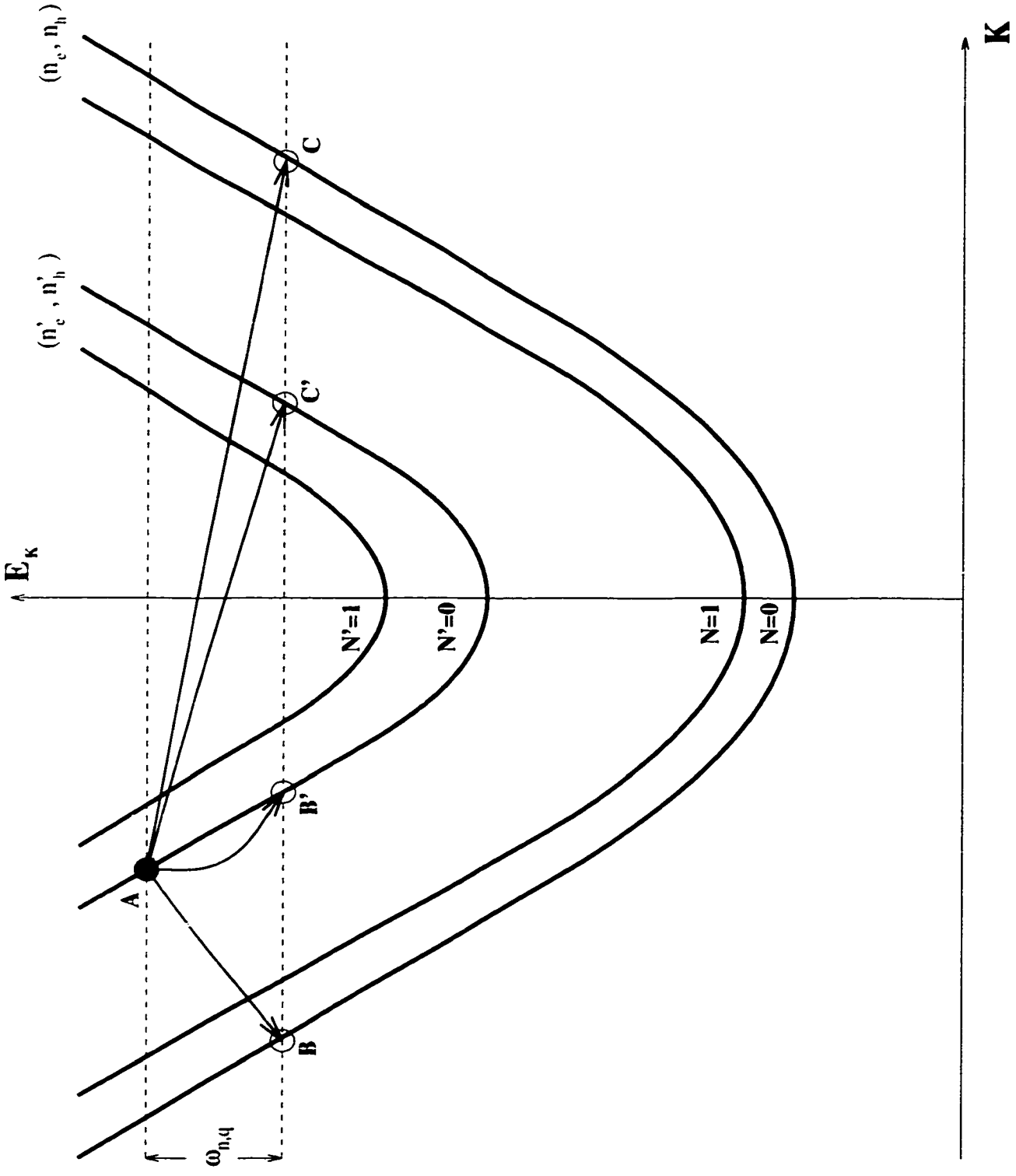

Figure 8.2: Schematic representation of allowed scattering processes. See text for discussion.

The first term in the r.h.s of Eq. (8.27) represents the intra-band scattering probability without changes in the internal state of the exciton branches. The second term is the probability of the intra-band scattering accompanied by transitions from N to other internal quantum states N', while the last term gives the inter-subband contribution to the exciton lifetime in the branch n_e, n_h with internal quantum number N and in-plane kinetic energy E_K. In the next section we study the dependence of the scattering rate on the in-plane exciton kinetic energy, on the phonon state n_p, and on the electron and hole effective masses.

8.4 Results and Discussion

For the numerical calculation of the scattering rate given by Eq. (8.25) and for an interpretation of the MPR reported in Ref. [53], we selected the GaAs/AlAs parameters given in [55]. In Table 8.1, we list the relevant values used in this calculation. The GaAs/AlAs QW is a type-II where the lowest electron conduction

	E_g (ev)	m_e/m_0	γ_1	γ_1	ϵ_0
GaAs	1.5192	0.0665	6.85	2.10	12.53
AlAs	3.1132	0.15	3.45	0.68	10.06

Table 8.1: Parameters used for GaAs/AlAs quantum well.

band belong to AlAs X-point of the Brillouin zone. Nevertheless, the reported data of Ref. [53] correspond to a resonant Raman process for the direct $\Gamma_{8v} - \Gamma_{6c}$ transition ($\hbar\omega > E_{\Gamma_{6c}} - E_{\Gamma_{8v}}$, where ω is the incoming frequency). Hence, for a backscattering configuration the electronic intermediate state taking place in the MPR of [53] correspond to the $\Gamma_{8v} - \Gamma_{6c}$ excitonic branch and the present calculation

is valid under the above experimental conditions. We used for the masses the in-plane mass $m_{h\perp} = m_0/(\gamma_1 \pm \gamma_2)$ and along z-direction $m_{hz} = m_0/(\gamma_1 \mp 2\gamma_2)$, where γ_1 and γ_2 are the Luttinger parameters [56]. The sign (+) or (-) corresponds to the light or heavy character of the mass, respectively. In Fig. 8.3 we show the dependence of the scattering rate on E_K in the $n_e = 1$, $n_h = 1$ excitonic branch and for the excitonic ground state $N = 0 \rightarrow N = 0$, $W^{(n)}_{0\rightarrow 0}$. Fig. 8.3(a) corresponds to a QW with a well width $d = 2$ nm while Fig. 8.3(b) is for $d = 1.7$ nm. The calculation represents the heavy hole contribution along the quantum well growth direction (light hole character in the x-y plane) due to the GaAs-like phonon modes L_2 and L_4 ($n_p = 2$ and $n_p = 4$). Since we are dealing with intra-band transitions ($n_e = n_h = 1$ for the final and initial states) the exciton-phonon interaction with odd modes is forbidden. It can be seen in Fig. 8.3(a) ($d = 2$ nm) that the main contribution corresponds to the L_4 mode and it is almost 3 times stronger than the L_2 mode. Fig. 8.3(b) shows opposite effect where the L_4 phonon mode is one order of magnitude weaker than the L_2 one.

To explain the above result we must to go back to the phonon dispersion relation of Fig. 8.1. For the $d = 2$ nm QW the L_2 confined mode is almost flat while the L_4 phonon has a stronger dispersion as a function of the phonon wave number $\vec{q}$ and it is in addition the symmetric QW phonon which has a predominantly interface character. The electrostatic potential associated with the L_4 mode in Fig. 8.3(a) gives strong coupling with excitons by the Fröhlich interaction in intra-subband transitions. The modes with largest $\phi_{n_p,\vec{q}}$ component in Eq. (8.25) are those which have the largest interface contribution, explaining why the scattering rate assisted by the L_4 phonon in Fig. 8.3(a) is stronger than that due to the L_2 confined mode.

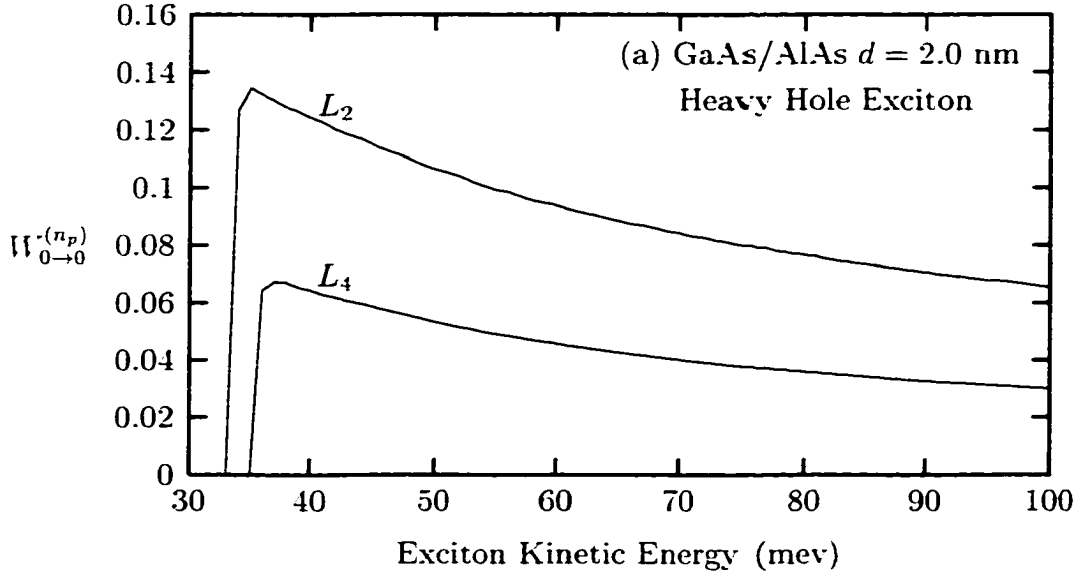

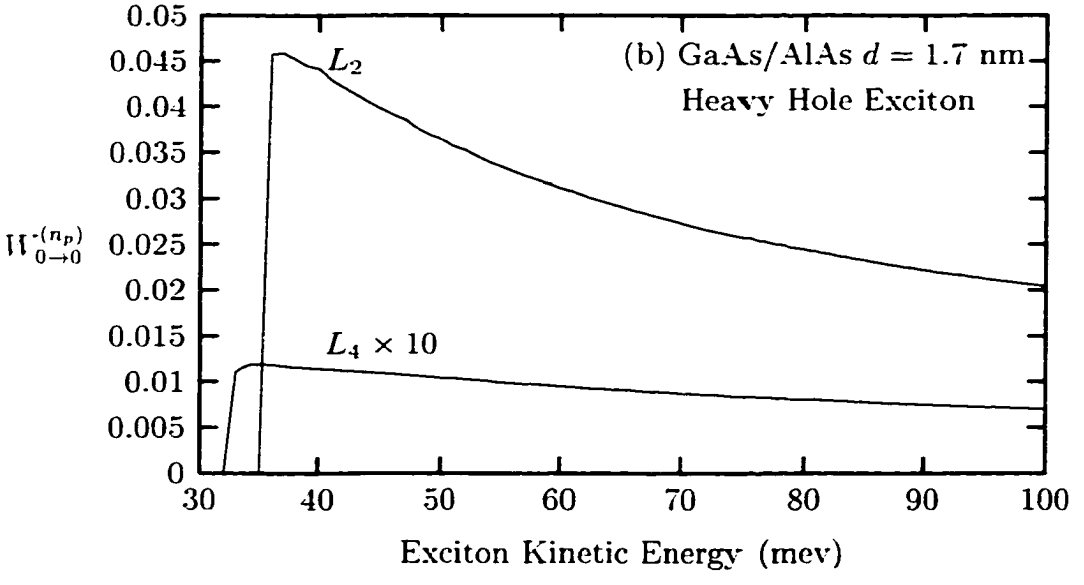

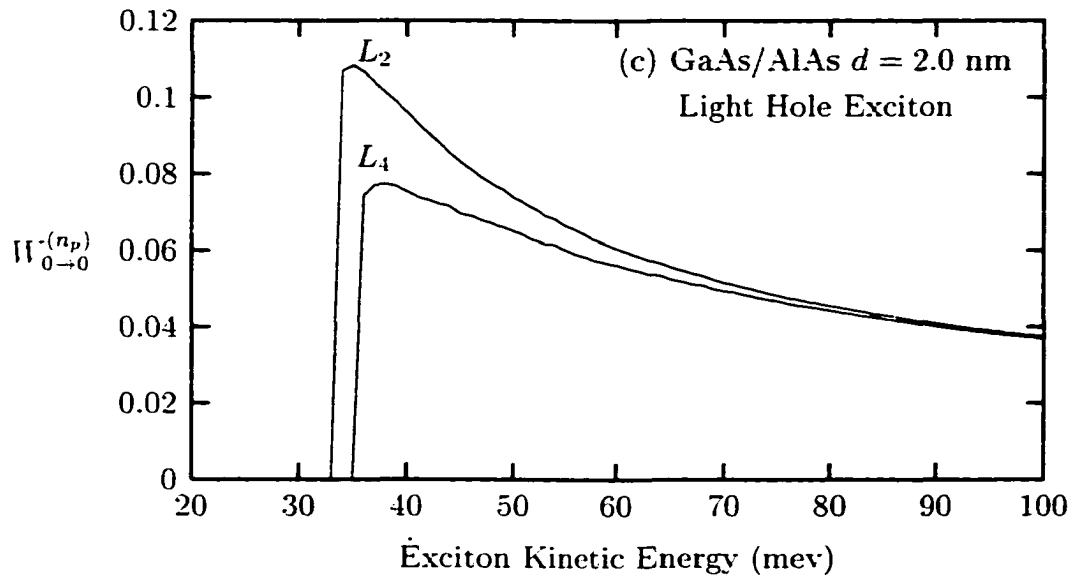

Figure 8.3: Exciton intra-subband scattering rate probability in units of $W_0 = 2\omega_L(\epsilon_0/\epsilon_\infty - 1)dM/(100a_B\mu)$ in a narrow QW as a function of the in-plane center-of-mass exciton kinetic energy. (a) and (b) correspond to the heavy-hole mass along the QW growth direction with $d = 2.0$ nm and $d = 1.7$ nm, respectively. (c) represents the light-hole mass along z-direction for $d = 2.0$ nm. The L_2 and L_4 phonon modes according to the notation followed in Fig. 8.1 have been considered for the one-phonon assisted exciton scattering rate.

In the case of $d = 1.7$ nm the L_4 GaAs-type phonon is more confined and it moves to lower frequency with an almost flat dispersion relation (see Fig. 8.3(b)). For the range of q values where the phonons are flat the Fröhlich interaction is proportional to $1/\sqrt{q^2 + q_z^2}$ with $q_z = n_p\pi/d$ ($n_p = 1, 2, ...$) [57]. Hence, the contribution to the intra-band scattering rate of the $n_p = 2$ mode is almost four times stronger than for the $n_p = 4$. Let us comment on the effect of the carrier effective masses on the scattering rate. First, the confinement is a function of the hole masses along the z-axis; Second, the hole-phonon matrix element depends on the hole masses through the $Q_h = m_h/Mqa_B$ factor and the range of values $q_{min} \leq q \leq q_{max}$ is a function of the electron-hole mass (in plane along the z-axis); Third, the scattering probability value strongly depends on the in-plane density of states. Fig. 8.3(c) shows the intraband exciton scattering rate for the case of the light-hole mass along the z-direction (heavy-hole character in x-y plane) and $d = 2$ nm. As in Fig. 8.3(a) the L_4 mode contribution is stronger than the L_2, showing that the relative intensity between several phonon branches is only a function of the phonon dispersion which itself depends on the QW width. The scattering rate values, in units of the constant W_0, for the light hole exciton contribution is smaller than the heavy-hole exciton one (see Figs. 8.3(a) and 8.3(c)). It is important to note that for the case we consider of isotropic effective masses and $m_e = m_h$ the intra-band transition $W_{0\to 0}^{(n_p)}$ is identically zero [46].

8.5 Conclusion

In conclusion we have performed an analysis of the exciton scattering rate in narrow QWs. The relaxation of hot excitons accounts for the emission of confined and

interface optical longitudinal phonons due to the Fröhlich-like exciton-phonon interaction. The results obtained above show a different behavior of the scattering probability as a function of the well width and in-plane exciton kinetic energy. The value of $W_{0\to 0}^{(n_p)}$ is not equal to zero for $E_K > \hbar\omega_{n_p,0}$ (for the case of intra-subband transition), increases with increasing E_K reaching a maximum and beginning to fall according to the law $E_K^{-1/2}$ [46]. The relative strength of the different phonon modes is proportional to the ratio of the square of their overlap integral of the function $\phi_{n_p,\vec{q}}$ with initial and final electron and hole subband states in the GaAs/AlAs QW. For a given phonon state, inter-subband transitions are less efficient processes on the exciton relaxation time in comparison with the intraband probability. The intra-subband scattering rate is accompanied only by symmetric phonon states ($n_p = 2, 4...$) in correspondence with the observed multiphonon Raman spectra in a series of short-period GaAs/AlAs superlattices [53]. The reported multiphonon peaks involving pure overtones of GaAs phonons are combinations of the even confined modes (see Fig. 6 in Ref. [53]). For samples with 10 GaAs monolayer width ($d \approx 2$ nm) combination of L_2 and L_4 (such as $2L_2$, $2L_4$, $3L_2$, $L_2 + 2L_4$, etc) are observed in the GaAs phonon spectra. In the case of samples with the 6 GaAs monolayer well width ($d \approx 1.7$ nm) only the combination of L_2 and interface GaAs modes ($2L_2$, $3L_2$, $L_2 + I$) are reported. Following the idea of the cascade model, where the iterated exciton-one-phonon interaction is the dominant mechanism, the MPR cross-section will be proportional to the $W_{0\to 0}^{(n_p)}(E_K)$ factor [58] (the inter-band exciton transitions give very small contribution and have been neglected). The obtained results shown on Fig. 8.3(b) predict that in a 6 monolayers sample, the MPR spectra needs to be composed mostly by combinations of L_2 confined modes while the combinations

with L_4 must be almost forbidden. The opposite conclusion is obtained from Fig. 8.3(a) ($d = 2$ nm) when combinations of L_2 and L_4 GaAs phonon modes in the multiphonon Raman spectra should present similar relative intensities. Thus, the experimental observation in GaAs/AlAs superlattices on the relative intensities of multiphonon scattering can be explained in the framework of a MPR cascade model taking into account the relative role of the confined and interface phonons on the hot exciton scattering rate.

8.6 Some Relevant Formulas

The norm of the vibrational amplitude is equal to

$$||u||^2 = \int_{-d/2}^{d/2} \left[Y^2(z) + Z^2(z) \right] dz, \tag{8.28}$$

where for odd potential states

$$\begin{aligned} Y(z) &= \eta_q \sin\left(\frac{2\eta_L z}{d}\right) - \eta_T \frac{S_L^- \exp(\eta_q) + S_L^+ \exp(-\eta_q)}{C_T^- \exp(\eta_q) - C_T^+ \exp(-\eta_q)} \sin\left(\frac{2\eta_T z}{d}\right) \\ &\quad + S_L^+ \frac{\omega_L^2 - \omega_T^2}{\omega_L^2 - \omega^2} \exp(-\eta_q) \sinh\left(\frac{2\eta_q z}{d}\right), \end{aligned} \tag{8.29}$$

$$\begin{aligned} Z(z) &= \eta_L \cos\left(\frac{2\eta_L z}{d}\right) + \eta_q \frac{S_L^- \exp(\eta_q) + S_L^+ \exp(-\eta_q)}{C_T^- \exp(\eta_q) - C_T^+ \exp(-\eta_q)} \cos\left(\frac{2\eta_T z}{d}\right) \\ &\quad + S_L^+ \frac{\omega_L^2 - \omega_T^2}{\omega_L^2 - \omega^2} \exp(-\eta_q) \cosh\left(\frac{2\eta_q z}{d}\right), \end{aligned} \tag{8.30}$$

and for even states

$$\begin{aligned} Y(z) &= \eta_q \cos\left(\frac{2\eta_L z}{d}\right) + \eta_T \frac{C_L^- \exp(\eta_q) - C_L^+ \exp(-\eta_q)}{S_T^- \exp(\eta_q) + S_T^+ \exp(-\eta_q)} \cos\left(\frac{2\eta_T z}{d}\right) \\ &\quad + C_L^+ \frac{\omega_L^2 - \omega_T^2}{\omega_T^2 - \omega^2} \exp(-\eta_q) \cosh\left(\frac{2\eta_q z}{d}\right), \end{aligned} \tag{8.31}$$

$$\begin{aligned} Z(z) &= \eta_L \sin\left(\frac{2\eta_L z}{d}\right) - \eta_q \frac{C_L^- \exp(\eta_q) - C_L^+ \exp(-\eta_q)}{S_T^- \exp(\eta_q) + S_T^+ \exp(-\eta_q)} \sin\left(\frac{2\eta_T z}{d}\right) \\ &\quad - C_L^+ \frac{\omega_L^2 - \omega_T^2}{\omega_T^2 - \omega^2} \exp(-\eta_q) \sinh\left(\frac{2\eta_q z}{d}\right), \end{aligned} \tag{8.32}$$

where

$$S^{\pm}_{L(T)} = \sqrt{\eta_q^2 + \eta^2_{L(T)}}\sin(\eta_{L(T)} \pm \theta_{L(T)}), \tag{8.33}$$

$$C^{\pm}_{L(T)} = \sqrt{\eta_q^2 + \eta^2_{L(T)}}\cos(\eta_{L(T)} \pm \theta_{L(T)}), \tag{8.34}$$

and

$$\begin{aligned}
\tan\theta_{L(T)} &= \frac{\eta_{L(T)}}{\eta_q}, \\
\eta_{L(T)} &= \frac{d}{2}\sqrt{\frac{\omega^2_{L(T)} - \omega^2}{\beta^2_{L(T)}} - q^2}, \\
\eta_q &= \frac{dq}{2},
\end{aligned} \tag{8.35}$$

and ω_T is the TO bulk phonon frequency. The functions S_0 and C_0 are defined in Refs. [55]

The matrix elements $I^{N',m'}_{N,m}$ represent the 2D excitonic transitions. From Eq.(8.9) and Eq.(8.14) it follows that

$$I^{N',m'}_{N,m} = \langle N|2(-1)^{|m'-m|}\int_0^{\pi}\cos(m'-m)\theta e^{im\rho q\cos\theta/M}d\theta|N'\rangle, \tag{8.36}$$

and θ being the angle between $\vec{\rho}$ and $\vec{q}$ vectors. The integration over θ gives

$$I^{N',m'}_{N,m} = (-i)^{|m'-m|}2\pi\langle N|J_{|m'-m|}\left(\frac{m}{M}\rho q\right)|N'\rangle, \tag{8.37}$$

where $J_\nu(z)$ is the Bessel function of order ν. Substituting Eq.(8.10) into Eq.(8.37), we have

$$\begin{aligned}
I^{N',m'}_{N,m} = {} & \nu_N^2 a_B^2 N_{N,m}N_{N',m'}\frac{\nu_N}{\nu_{N'}}^{|m'|}\int_0^{\infty} r^{|m|+|m'|+1}e^{-r(1+\nu_N/\nu_{N'})/2} \\
& F(-N+|m|,2|m|+1,r)F(-N'+|m'|,2|m'|+1,\frac{\nu_N}{\nu_{N'}}r)J_{|m'-m|}(Q\nu_N r)dr
\end{aligned} \tag{8.38}$$

with $\nu_N = (N+1/2)/2$. The hypergeometric function $F(-N+|m|, 2|m|+1, r)$ is a polynomial in r and the integral (8.38) can be obtained making use of the identity [59]

$$\int_0^\infty x^{p+1} e^{-\alpha x} J_\nu(\beta x) dx = (-1)^{p+1} \beta^{-\nu} \frac{d^{p+1}}{d\alpha^{p+1}} \left[\frac{(\sqrt{\alpha^2+\beta^2}-\alpha)^\nu}{\sqrt{\alpha^2+\beta^2}} \right], \tag{8.39}$$

with $\beta > 0$ and $\nu > 0$. We thus find

$$\begin{aligned}
I_{0,0}^{0,0}(Q) &= \frac{1}{2\pi} \frac{1}{(1+Q^2)^{\frac{3}{2}}}, \\
I_{0,0}^{1,0}(Q) &= \frac{1}{2\pi\sqrt{3^3}} \frac{Q^2}{(\frac{4}{9}+Q^2)^{\frac{5}{2}}}, \\
I_{0,0}^{1,\pm1}(Q) &= \frac{-i\sqrt{2}}{6\pi\sqrt{3^3}} \frac{Q}{(\frac{4}{9}+Q^2)^{\frac{5}{2}}}, \\
I_{0,0}^{2,0}(Q) &= \frac{1}{2\pi\sqrt{5^3}} \frac{2Q^2+\frac{9}{25}}{(Q^2+\frac{9}{25})^{\frac{7}{2}}}, \\
I_{0,0}^{2,\pm1}(Q) &= \frac{-i}{2\pi\sqrt{5^3}} \frac{\sqrt{6}}{10} \frac{Q(2Q^2+\frac{9}{25})}{(Q^2+\frac{9}{25})^{\frac{7}{2}}}, \\
I_{0,0}^{2,\pm2}(Q) &= \frac{-1}{2\pi\sqrt{5^3}} \frac{\sqrt{9}}{50\sqrt{6}} \frac{Q^2}{(Q^2+\frac{9}{25})^{\frac{7}{2}}}.
\end{aligned} \tag{8.40}$$

Chapter 9

Ground State Properties of Quantum Dots

9.1 Introduction

Quantum dots (quasi-zero-dimensional electron systems) are one of the most interesting systems in semiconductor nanostructures and have received increasing attention in recent years because of many novel physical properties observed in these systems as well as the potential for future technological applications [60]. Essentially, quantum dots are little islands of two-dimensional electrons which are laterally confined by an artificial potential and hence can be thought of as artificial atoms with a well controlled number of electrons. The purpose of this chapter is to obtain the eigenstates and eigenenergies of a quantum dot with several electrons inside. For such a few body problem, the exact numerical calculation based on the second quantization formalism is possible and gives very accurate results. We will first describe a theoretical model for quantum dot in strong magnetic field. We then present the numerical method used to diagonalize the second quantized Hamiltonian. The result is obtained for four-electron quantum dot. We also give the analytical expression for the Coulomb interaction matrix elements.

9.2 Theoretical Model and Exact Numerical Calculation

Because most current experiments have focused attention on quantum dots in a magnetic field, we consider the following Hamiltonian for N electrons in a quantum dot with confining potential $V_c(\vec{r})$ and an external magnetic field $\vec{B}$ along the z-axis

$$\hat{H} = \sum_i \left[\frac{1}{2m*} \left(\vec{p}_i + \frac{e\vec{A}_i}{c} \right)^2 + V_c(\vec{r}_i) \right] + \sum_{i<j} V_I(\vec{r}_i - \vec{r}_j) + g^* \mu_B \vec{B} \sum_i s_{i,z}, \qquad (9.1)$$

where m^* is the effective mass of electron and g^* is the effective g-factor. Due to the recent far-infrared optical measurements and generalized Kohn's theorem, the one-body confinement potential $V_c(\vec{r})$ is near parabolic, i.e. $V_c = \frac{1}{2} m^* \omega_0^2$ [61]. The Coulomb interaction can be used for $V_I(\vec{r}_i - \vec{r}_j)$ if we ignore the presence of image charges in the surrounding dielectric materials. In this work, we assume a sufficiently large magnetic field so that the spins are polarized. The single-electron wave functions are [61]

$$\phi_{nl} = C_{nl} r^{|l|} \exp(-il\theta) L_n^{|l|}(r^2/2a^2) \exp(-r^2/4a^2), \qquad (9.2)$$

where the normalization constant C_{nl} is given by

$$C_{nl} = \left[\frac{\sqrt{2}}{2a\pi} \frac{n!}{(n+|l|)!} \right]^{\frac{1}{2}} \left(\frac{\sqrt{2}}{2a} \right)^{|l|}, \qquad (9.3)$$

and the single-electron energies are

$$E_{nl} = (2n + |l| + 1)\hbar\Omega - \frac{1}{2} l \hbar \omega_c. \qquad (9.4)$$

where $n = 0, 1, 2, \ldots$ and $l = 0, \pm 1, \pm 2, \ldots$. Here $\omega_c = eB/m^*c$ is the cyclotron frequency, $\Omega = (\frac{1}{4}\omega_c^2 + \omega_0^2)^{1/2}$, $a = (\hbar/2m^*\Omega)^{1/2}$ is the magnetic length, and $L_n^{|l|}(x)$

are associated Laguerre polynomials. In the limit of $\omega_0 \to 0$ or $B \to \infty$, we have $E = (N + 1/2)\hbar\omega_c$ with $N = n + \frac{1}{2}(|l| - l)$ as Landau level index. The second quantized Hamiltonian is given by

$$H = \sum_{nl} E_{nl} c^\dagger_{nl} c_{nl} + \sum_{n_1 \ldots n4} \sum_{l_1 \ldots l4} A_{n_1 l_1, n_2 l_2, n_3 l_3, n_4 l_4} c^\dagger_{n_1 l_1} c^\dagger_{n_2 l_2} c_{n_3 l_3} c_{n_4 l_4}. \tag{9.5}$$

where A is the Coulomb matrix element defined as

$$A = \frac{1}{2} \int d\vec{r}_1 d\vec{r}_2 \phi^*_{n_1 l_1}(\vec{r}_1) \phi^*_{n_2 l_2}(\vec{r}_2) \frac{e^2}{|\vec{r}_1 - \vec{r}_2|} \phi_{n_3 l_3}(\vec{r}_2) \phi_{n_4 l_4}(\vec{r}_1). \tag{9.6}$$

We will give the exact analytical expression for these matrix elements in the next section. Noticing that the total angular momentum J is a good quantum number, we divide the Hilbert space into many sub-spaces corresponding to different J. On the other hand, in order to choose a finite basis set in each sub-space, we fixed the sum of Landau level indices: $N_{tot} = \sum N$. For example, $N_{tot} = 0$ means all electrons must stay in the lowest Landau level.

For parameters appropriate to GaAs, we have calculated the energy levels of the four-electron system by numerically diagonalizing the H matrix. The result is shown in Fig. 9.1, which agrees with Maksym and Chakraborty's calculation [61].

9.3 Coulomb Matrix Element

In this section, we give the analytical expression for the Coulomb interaction matrix elements defined in Eq. (9.6) as follows

$$\begin{aligned} A &= \frac{1}{2} \int d\vec{r}_1 d\vec{r}_2 \phi^*_{n_1 l_1}(\vec{r}_1) \phi^*_{n_2 l_2}(\vec{r}_2) \frac{e^2}{|\vec{r}_1 - \vec{r}_2|} \phi_{n_3 l_3}(\vec{r}_2) \phi_{n_4 l_4}(\vec{r}_1) \\ &= \frac{e^2}{2\epsilon} \frac{\sqrt{2}}{2a} \delta_{l_1 + l_2, l_3 + l_4} \left[\frac{n_1!}{(n_1 + |l_1|)!} \frac{n_2!}{(n_2 + |l_2|)!} \frac{n_3!}{(n_3 + |l_3|)!} \frac{n_4!}{(n_4 + |l_4|)!} \right]^{\frac{1}{2}} \end{aligned}$$

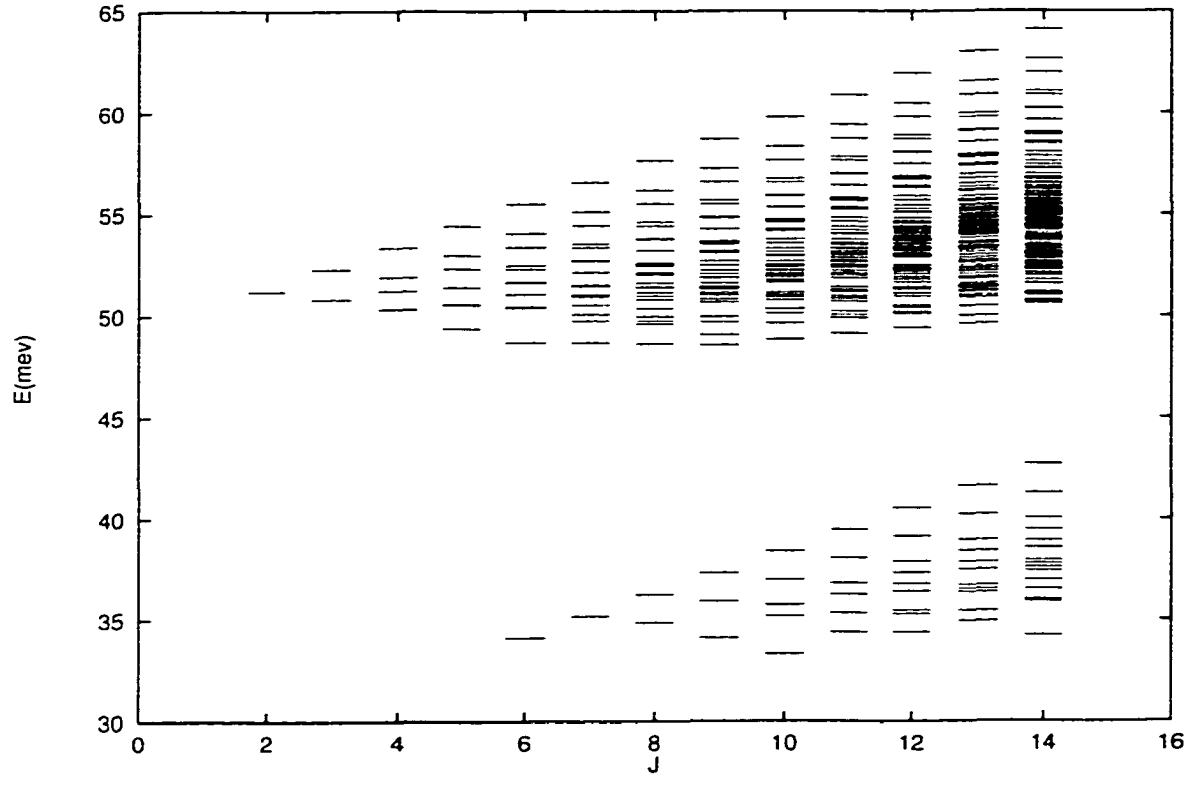

Figure 9.1: Energy levels as a function of J for four electrons in a GaAs quantum dot with $B = 8T$.

$$
\begin{aligned}
&\times \sum_{\alpha=0}^{n_1}\sum_{\beta=0}^{n_3}\sum_{\gamma=0}^{n_2}\sum_{\delta=0}^{n_4}\left[\alpha+\beta+\frac{1}{2}(|l_1|+|l_3|-|l_1-l_3|)\right]!\left[\gamma+\delta+\frac{1}{2}(|l_2|+|l_4|-|l_1-l_3|)\right]! \\
&\times \frac{(-1)^{\alpha+\beta}}{\alpha!\beta!}\frac{(n_1+|l_1|)!(n_3+|l_3|)!}{(|l_1|+\alpha)!(n_1-\alpha)!(|l_3|+\beta)!(n_3-\beta)!} \\
&\times \frac{(-1)^{\gamma+\delta}}{\gamma!\delta!}\frac{(n_2+|l_2|)!(n_4+|l_4|)!}{(|l_2|+\gamma)!(n_2-\gamma)!(|l_4|+\delta)!(n_4-\delta)!} \\
&\times \sum_{p=0}^{\alpha+\beta+\frac{1}{2}(|l_1|+|l_3|-|l_1-l_3|)}\frac{\left[\alpha+\beta+\frac{1}{2}(|l_1|+|l_3|+|l_1-l_3|)\right]!}{\left[\alpha+\beta+\frac{1}{2}(|l_1|+|l_3|-|l_1-l_3|)-p\right]!(|l_1-l_3|+p)!} \\
&\times \sum_{s=0}^{\gamma+\delta+\frac{1}{2}(|l_2|+|l_4|-|l_1-l_3|)}\frac{\left[\gamma+\delta+\frac{1}{2}(|l_2|+|l_4|+|l_1-l_3|)\right]!}{\left[\gamma+\delta+\frac{1}{2}(|l_2|+|l_4|-|l_1-l_3|)-s\right]!(|l_1-l_3|+s)!}.
\end{aligned}
\tag{9.7}
$$

Bibliography

[1] A. D. Griffin, W. Snoke, and S. Stringari, *Bose-Einstein Condensation* (Cambridge University Press, Cambridge, 1995).

[2] M. H. Anderson, J. R. Ensher, M. R. Matthews, C. E. Wieman, and E. A. Cornell, Science **269**, 198 (1995).

[3] K. B. Davis, M. O. Mewes, M. R. Andrews, N. J. van Druten, D. S. Durfee, D. M. Kurn, and W. Ketterle, Phys. Rev. Lett. **75**, 3969 (1995).

[4] C. C. Bradley, C. A. Sackett, J. J. Tollett, and R. G. Hulet, Phys. Rev. Lett **75**, 1687 (1995).

[5] E. A. Cornell, J. R. Ensher, and C. E. Wieman, Preprint cond-mat/9903109 (1999).

[6] F. Dalfovo, S. Giorgini, L. P. Pitaevskii, and S. Stringari, Rev. of Mod. Phys. **71**, 463 (1999).

[7] A. S. Parkins and D. F. Walls, Phys. Rep. **303**, 1 (1998).

[8] A. L. Fetter, Preprint cond-mat/9811366 (1998).

[9] A. L. Fetter, Ann. of Phys. **70**, 67 (1972).

[10] K. Huang, *Statistical Mechanics* (John Wiley and Sons, New York, 1987), 2nd ed.

[11] G. Baym and C. J. Pethick, Phys. Rev. Lett. **76**, 6 (1996).

[12] W. H. Press, S. A. Teukolsky, W. T. Vetterling, and B. P. Flannery, *Numerical Recipes in C* (Cambridge University Press, Cambridge, 1992), 2nd ed.

[13] F. Dalfovo and S. Stringari, Phys. Rev. A **53**, 2477 (1996).

[14] M. Edwards, R. J. Dodd, C. W. Clark, and K. Burnett, J. Res. Nat. Inst. Stand. Tech. **101**, 553 (1996).

[15] M. Edwards, P. A. Ruprecht, K. Burnett, R. J. Dodd, and C. W. Clark, Phys. Rev. Lett. **77**, 1671 (1996).

[16] B. D. Esry, Phys. Rev. A **55**, 1147 (1997).

[17] D. S. Jin, J. R. Ensher, M. R. Matthews, C. E. Wieman, and E. A. Cornell, Phys. Rev. Lett. **77**, 420 (1996).

[18] A. Smerzi and S. Fantoni, Phys. Rev. Lett. **78**, 3589 (1997).

[19] M. J. Holland, D. S. Jin, M. L. Chiofalo, and J. Copper, Phys. Rev. Lett. **78**, 3801 (1997).

[20] N. Balakrishnan, Phys. Rep. **280**, 79 (1997).

[21] C. Leforestier, R. H. Bisseling, C. Cerjan, M. D. Feit, R. Friesner, A. Guldberg, A. Hammerich, G. Jolicard, W. Karrlein, H. D. Meyer, N. Lipkin, O. Roncero, *et al.*, J. of Comput. Phys. **94**, 59 (1991).

[22] A. Griffin, Phys. Rev. B **53**, 9341 (1996).

[23] A. Griffin, Preprint Cond-mat/9901172 (1999).

[24] S. Giorgini, L. P. Pitaevskii, and S. Stringari, J. Low Temp. Phys. **109**, 309 (1997).

[25] E. A. Cornell, D. S. Hall, M. R. Matthews, and C. E. Wieman, Preprint cond-mat/9808105 (1998).

[26] T. L. Ho and V. B. Shenoy, Phys. Rev. Lett. **77**, 3276 (1996).

[27] H. Pu and N. P. Bigelow, Phys. Rev. Lett. **80**, 1130 (1998).

[28] D. S. Hall, M. R. Matthews, C. E. Wieman, and E. A. Cornell, Preprint cond-mat/9805327 (1998).

[29] D. S. Hall, M. R. Matthews, J. R. Ensher, C. E. Wieman, and E. A. Cornell, Preprint cond-mat/9804138 (1998).

[30] B. D. Esry, C. H. Greene, J. P. Burke, and J. L. Bohn, Phys. Rev. Lett. **78**, 3594 (1997).

[31] E. M. Lifshitz and L. P. Pitaevskii, *Statistical Physics, Part II* (Pergamon, Oxford, 1980).

[32] C. C. Bradley, C. A. Sackett, and R. G. Hulet, Phys. Rev. Lett. **78**, 985 (1997).

[33] D. A. W. Huntchinson, E. Zaremba, and A. Griffin, Phys. Rev. Lett. **78**, 1842 (1997).

[34] D. S. Jin, M. R. Matthews, J. R. Ensher, C. E. Wieman, and E. A. Cornell, Phys. Rev. Lett. **78**, 764 (1997).

[35] S. Choi, S. A. Morgan, and K. Burnett, Phys. Rev. A **57**, 4057 (1998).

[36] W. V. Liu, Phys. Rev. Lett. **79**, 4056 (1997).

[37] P. O. Fedichev, G. V. Shlyapnikov, and J. T. M. Walraven, Phys. Rev. Lett. **80**, 2269 (1998).

[38] S. Giorgini, Phys. Rev. A **57**, 2949 (1998).

[39] S. T. Chui and P. Ao, Phys. Rev. A **59**, 1473 (1999).

[40] B. D. Esry and C. H. Greene, Phys. Rev. A **59**, 1457 (1999).

[41] P. Öhberg, Phys. Rev. A **59**, 634 (1999).

[42] M. R. Matthews, B. P. Anderson, P. C. Haljan, D. S. Hall, C. E. Wieman, and E. A. Cornell, Phys. Rev. Lett. **83**, 2498 (1999).

[43] B. Jackson, J. F. McCann, and C. S. Adams, Phys. Rev. Lett. **80**, 3903 (1998).

[44] J. E. Williams and M. J. Holland, Preprint cond-mat/9909163 (1999).

[45] E. Gross, S. Permogorov, V. Morozenko, and B. Kharlamov, Phys. Status Solidi B **59**, 551 (1973).

[46] K. A. Aristora, C. Trallero-Giner, I. G. Lang, and S. T. Pavlov, Phys. Status Solidi B **85**, 351 (1978).

[47] C. Trallero-Giner, L. I. Korovin, and S. T. Pavlov, Fiz. Tverd. Tela **19**, 2456 (1977).

[48] C. Trallero-Giner, I. G. Lang, and S. T. Pavlov, Fiz. Tekh. Poluprovodnikor **14**, 235 (1980).

[49] V. F. Sapega, M. P. Chamberlain, T. Ruf, M. Cardona, D. N. Mirlin, K. Tötemeyer, A. Fisher, and K. Eberl, Phys. Rev. B **52**, 14144 (1995).

[50] M. C. Thatan, J. F. Ryan, and C. T. Foxon, Phys. Lett. **63**, 1637 (1989).

[51] K. T. Tsen, K. R. Wald, T. Ruf, P. Y. Yu, and H. Mordoc, Phys. Lett. **63**, 2557 (1991).

[52] S. C. Lee and I. Galbraith, Phys. Rev. B **59**, 15796 (1999).

[53] D. J. Mowbray, M. Cardona, and K. Ploog, Phys. Rev. B **43**, 11815 (1991).

[54] C. Trallero-Giner, F. Carcia-Moliner, and M. Cardona, Phys. Rev. B **45**, 11944 (1992).

[55] F. Comas, R. Pérez-Alvarez, C. Trallero-Giner, and M. Cardona, Superlatt. Microstr. **14**, 95 (1993).

[56] O. Madelung, J. Shultz, and H. Weiss, *Landolt-Börstein Tables* (Springer, Berlin, 1982), vol. III, p. 17a and 22a.

[57] C. Trallero-Giner and F. Comas, Phys. Rev. B **37**, 4583 (1988).

[58] C. Trallero-Giner, I. G. Lang, and S. T. Pavlov, Fiz. Tverd. Tela **23**, 1265 (1981).

[59] I. S. Gradshteyn and I. M. Ryzhik, *Tables of Integrals, Series and Products* (Academic, New York, 1980).

[60] T. Chakraborty, Comments Cond. Mat. Phys **16**, 35 (1992).

[61] P. A. Maksym and T. Chakraborty, Phys. Rev. Lett. **65**, 108 (1990).